Development of Methodologies in Solid-State Nuclear Magnetic Resonance and Their Applications in Material Chemistry

A Thesis

Submitted to the
Tata Institute of Fundamental Research, Mumbai
for the degree of Doctor of Philosophy
in Chemistry

by
Mithun Goswami

School of Natural Sciences
Tata Institute of Fundamental Research
Mumbai
August, 2010

DECLARATION

This thesis is a presentation of my original research work. Wherever contributions of others are involved, every effort is made to indicate this clearly, with due reference to the literature, and acknowledgement of collaborative research and discussions.

The work was done under the guidance of Prof. P. K. Madhu, at the Tata Institute of Fundamental Research, Mumbai.

[Mithun Goswami]

In my capacity as supervisor of the candidate's thesis, I certify that the above statements are true to the best of my knowledge.

[Prof. P. K. Madhu]
Date:

Acknowledgements

My Ph.D years at the Tata Institute of Fundamental Research and this thesis has had mentorship from numerous outstanding individuals both from within and outside the institute. It is to these individuals, that my heartfelt gratitude and thanks go out, for without their help, this thesis would not have seen the light of the day.

I am heartily thankful to my supervisor, Prof. P. K. Madhu, whose encouragement, guidance and support from the initial to the final level enabled me to develop an understanding of the subject. His thoughtful advise often served to give me a sense of direction during my Ph.D studies.

A special thanks to Prof. Subramanian Ganapathy from National Chemical Laboratory, Pune, with whom I worked in one of my projects. His deep understanding of the subject and valuable advise helped me to shape some of the interesting results.

I want to express my gratitude to Dr. Thomas Bräuniger with whom various discussions were made at different stages of my Ph.D. He made many valuable suggestions and gave constructive advice which improved the quality of this thesis.

I wish to thank Prof. Malcolm Levitt, Prof. Shimon Vega, and Prof. Angelika Sebald for the numerous discussions made with them during various meetings which were a great source of knowledge and inspiration.

Special Gratitude goes to Prof. P. K. Madhu and British Council, India for kindly arranging my visit to Southampton University, UK, to take part in the Cryo-NMR symposium. I would also like to extend my gratitude to the organising committee of the 6th Alpine Conference on Solid-State NMR for providing me with the scholarship to attend the conference.

I am deeply grateful to the members of the National Facility for High Field NMR for the trust and support that they gave me in order to carry out my studies. A special thanks to Manoj Naik who provided me with all the technical supports whenever I needed them.

I am tempted to individually thank all of my friends who, from my childhood until graduate school, have joined me in the discovery of what life is about and how to make the best of it. However, because the list might be too long and by fear of leaving someone out, I will simply say thank you very much to you all.

I cannot finish without saying how grateful I am to my family: my parents, my two sisters, and near relatives who have given me a loving environment to develop. Lastly, and most importantly, I wish to thank my wife Sanghamitra. She has always supported

and encouraged me to do my best in all matters of life. To them I dedicate this thesis.

Table of Contents

List of Figures

List of Tables

Statement Regarding New Facts

- Improved sensitivity enhancement scheme

  1. An improved sensitivity enhancement scheme for half-integer spin quadrupolar nuclei was developed under both magic angle spinning (MAS) and static condition.

  2. The new scheme shows very little dependence on experimental parameters such as spinning frequency and the nutation radio frequency of the pulses making it a highly robust method.

- Characterization of different polymorphs of Alq_3

  1. Solid-state NMR methods were used to distinguish between all the different polymorphs of Alq_3 and their quadrupolar parameters were also extracted.

  2. It was also shown that all the different polymorphs contain ^{27}Al in single unique crystallographic site.

  3. It was also demonstrated that by using Isodensity Polarisable Continuum Model (IPCM) for Density Functional Theory (DFT) based quantum chemical calculation one can more accurately predict the quadrupolar parameters for these kinds of systems.

  4. Solid-state NMR also revealed that the solvated form of Alq_3 has completely different quadrupolar parameters from all the other polymorphs of Alq_3.

  5. It was further revealed by temperature dependent study on the solvated Alq_3 that the presence of ethanol in the crystal matrix is the sole reason for the difference in the quadrupolar parameters.

- Application of symmetry based recoupling method and high-resolution solid-state NMR methods for quadrupolar nuclei for simultaneous extraction of dipolar and quadrupolar information.

1. Two dimensional quadrupolar-dipolar correlation spectra was obtained by combining symmetry based recoupling sequence $R18_2^5$ on ^1H and spin-echo on ^{17}O. From this correlation spectra one can obtain the information about the dipolar coupling constant at any point of the quadrupolar powder pattern.

2. High-resolution solid-state NMR methods such as Satellite Transition Magic Angle Spinning (STMAS) technique was combined with $R18_2^5$ symmetry sequence in three dimensional fashions to simultaneously extract dipolar and quadrupolar information.

3. Two dimensional numerical simulations were done to ascertain the relative orientation of dipolar tensor with respect to the quadrupolar tensor.

- Sensitivity enhancement of ^{29}Si double-quantum spectroscopy and its application

  1. An enhancement in the detection sensitivity of dipolar recoupled ^{29}Si double-quantum magic-angle spinning experiment was shown with a Carr-Purcell-Meiboom-Gill (CPMG) train of π pulses during the acquisition period of symmetry-adapted pulse schemes, such as POST-C7 and SR26.

  2. Application of POST-C7-CPMG method for framework characterization was demonstrated in the disordered and catalytically important ZSM-5 molecular sieve.

  3. Based on the observed double-quantum dipole-dipole correlation and the known T-site Si connectivity, the assignment of all the signals was made.

Synopsis

Statutory Declarations

Name of the Candidate	:	*Mithun Goswami*
Title of the Thesis	:	*Development of Methodologies in Solid-State Nuclear Magnetic Resonance and Their Applications in Material Chemistry*
Degree	:	*Doctor of Philosophy (Ph. D.)*
Subject	:	*Chemistry*
Name of the Guide	:	*Prof. P. K. Madhu*
Registration No.	:	*CHEM - 026*
Date of Registration	:	*5th January 2007*
Place of Research	:	*Department of Chemical Sciences Tata Institute of Fundamental Research, Homi Bhabha Road, Colaba, Mumbai - 400005*

Introduction

Spatial proximity and/or a chemical bond between two atoms can give rise to interactions between nuclei. In general, these interactions are orientation dependent. In media with no or little mobility (e.g. crystals, powders, large membrane vesicles, molecular aggregates), anisotropic interactions have a substantial influence on the behaviour of a system of nuclear spins. In contrast, in a classical liquid-state NMR experiment, Brownian motion leads to an averaging of anisotropic interactions. In such cases, these interactions can be neglected on the time-scale of the NMR experiment. Anisotropic interactions modify the nuclear spin energy levels (and hence the resonance frequency) of all sites in a molecule, and often contribute to a line-broadening effect in NMR spectra. However, there is a range of situations when their presence can either not be avoided, or is even particularly desired, as they encode structural parameters, such as orientation information, on the molecule of interest.

High-resolution conditions in solids (in a wider sense) can be established using magic angle spinning (MAS), and a variety of radio frequency (RF) irradiation patterns. While the latter allows decoupling of interactions in spin space, the former facilitates averaging of interactions in real space. In addition, line-broadening effects from microscopic inhomogeneities can be reduced by appropriate methods of sample preparation. Under decoupling conditions, isotropic interactions can report on the local structure, e.g. by the isotropic chemical shift. In addition, decoupled interactions can be selectively reintroduced ("recoupling"), and used, for example, in controlled de-phasing or transfer of polarization, which allows to derive a number of structural parameters. Hence the presence of line broadening in solid-state NMR, once thought to be a hindrance can actually provide much information about the chemistry, structure and dynamics in solid state.

Solid-state NMR has developed rapidly in the past few years and is finding ever increasing application in substances of chemical, material and biological importance. The standard nuclei, such as ^{11}B, ^{13}C, ^{23}Na, ^{27}Al, ^{29}Si and ^{31}P have been supplemented

with ever increasing range of other nuclei. The wider availability of higher magnetic fields has encouraged the greater coverage of periodic table. There are also now a range of techniques to enhance the signal intensity, especially by the manipulation of the population of the satellite transitions of quadrupolar nuclei. Compared to the past, the proliferation of solid-state NMR as a characterization tool for organic, inorganic and biological samples has meant that the technique is more often used and data reported in papers concerning such materials.

This thesis addresses the development of methods for sensitivity enhancements in solid-state NMR and also their applications in the structural characterizations of substances which are chemically important. This thesis demonstrates the design of an improved sensitivity enhancement scheme for half-integer spin quadrupolar nuclei which not only gives high sensitivity enhancement but also quite robust to the change of experimental parameters. Work has also been done to use high-resolution solid-state NMR techniques for quadrupolar nuclei to characterize Alq_3 which is one of the most important organic light emitting diodes. Further the present work demonstrates the use of IPC model [110] for more accurate prediction of quadrupolar parameters using quantum chemical calculations. Current work also deals with the technique to easily characterize zeolites using ^{29}Si NMR. Attempts were also made to combine recoupling technique to reintroduce heteronuclear dipolar coupling and high-resolution NMR schemes for quadrupolar nuclei in three dimensional form to simultaneously extract dipolar and quadrupolar informations.

Development of New Sensitivity Enhancement Scheme for Quadrupolar Nuclei

The potential application of NMR in the study of quadrupolar nuclei in the materials of inorganic, catalytic and biological importance is well documented. However, the

study of quadrupolar nuclei using NMR is often hindered due to one or many of the following factors such as, low natural abundance, small value of gyromagnetic ratio and large quadrupolar interaction constant. As a result the observable central-transition (CT) single-quantum (SQ) signal in one-dimensional (1D) experiments is often besieged with sensitivity problems even under magic-angle spinning (MAS). These become more acute when spectra need to be acquired under static conditions. Hence, sensitivity enhancement of the NMR spectra of half-integer spin quadrupolar nuclei is of utmost importance.

Since the seminal work by Vega and Naor [28] which showed that the application of amplitude modulated pulse lead to the population inversion of satellite transition thereby creating enhanced population difference across the observable central transition resulting in signal enhancement, several new sensitivity enhancement techniques have been developed. Some of the notable among them are "dual Q-probe" and frequency-swept adiabatic passage schemes [43, 44], double-frequency sweeps (DFS) [33], fast amplitude-modulated (FAM) pulses [31], Gaussian pulse trains [37], and hyperbolic secant pulses [38]. Variants of FAM which generate a frequency sweep by modulating the pulse duration in either a linear or non-linear way, notated as SW(τ)-FAM and SW($1/\tau$)-FAM, were found to give good signal enhancement in the case of static samples [77].

We developed a new scheme, *m*-FAM for signal enhancement where we applied multiple rotor assisted population transfers with FAM pulse pairs. The idea was to repeat FAM pulses along with the acquisition multiple times before the spin system returns to thermal equilibrium. This was found to be beneficial as always there is a considerable amount of spin polarisation left in the satellite transitions that are not transferred to the central transitions. By repeating the whole sequence several times within the relaxation time it is ensured that a substantial fraction of the population in the satellite transitions is converted to central transition.

We applied *m*-FAM under both MAS and static condition on spin-3/2 and spin-5/2 systems. We denote the *m*-FAM scheme as $\mathrm{F}^{I}_{n:m}(\tau)$, where *n* corresponds to the total

number of pulse pairs in the FAM scheme and τ is the duration of one FAM block in μs and m in the subscript indicates the number of times FAM and acquisition are repeated. The Roman numeral in the superscript suggests that FAM-I is used here. For ^{23}Na ($I=3/2$) we used m-FAM of the type $F^{I}_{18:10}$ (2.8) and for ^{27}Al ($I=5/2$) we used m-FAM of the form $F^{I}_{10:12}(6)F^{I}_{20:12}(7)$. For rotor synchronised m-FAM experiments on ^{27}Al we made use of m-FAM of the form $F^{I}_{10:12}(6)F^{I}_{20:12}(6)$ to obtain maximum enhancement. When m-FAM was applied to ^{23}Na ($I=3/2$) in Na_2SO_4 under MAS condition we obtained an enhancement of 3.3 times whereas normal FAM gave an enhancement of 1.66 compared to single 90^0 pulse. Further when m-FAM was applied under static condition we obtained an enhancement by a factor of 2 while normal FAM did not give any appreciable enhancement. We also applied m-FAM to ^{27}Al ($I=5/2$) in Gibbsite sample again under MAS and static condition. Under MAS we get an enhancement of 6.85 times while normal FAM gave enhancement of 2.05 times. We further observed that the m-FAM scheme is quite robust with respect to the experimental parameters such as MAS rate and nutation radio frequency of the FAM pulses (v^{FAM}_{nut}). Variation of both the parameters cause minor changes in the total enhancement factors for both spin-3/2 and spin-5/2 systems.

We also demonstarted that if SW($1/\tau$)-FAM which performs much better in static condition than normal FAM is repeated in a similar fashion to that of m-FAM one can get higher enhancements. When SW($1/\tau$)-FAM was applied multiple times (m-SW($1/\tau$)-FAM) in case of ^{27}Al ($I=5/2$) in Gibbsite under static condition we obtained an enhancement of 6.64 while normal SW($1/\tau$)-FAM gave an enhancement of 2.1. Here also we observed that m-SW($1/\tau$)-FAM is quite robust with respect to the experimental parameter v^{FAM}_{nut}.

Structural Characterization of Different Polymorphs of Alq$_3$

After the initial demonstration by Tang and Van Slyke [84] Tris(8-hydroxyquinolinato)-aluminium(III), known as Alq$_3$, has become a workhorse material for organic light emit-

ting devices (OLED) and/or electron transporting material in OLED. Alq_3 is an octahedral chelate complex with Al^{3+} ion in the center and three 8-hydroxyquinolinate ions octahedrally coordinated around it. Alq_3 has two geometric isomers, meridional and facial. X-ray diffraction studies showed that two polymorphs of Alq_3, α and β contain meridional isomers [85] which show green photoluminescence. Another polymorph δ-Alq_3 on the other hand contains facial form [87] which shows blue photoluminescence. These results suggest that there is a clear correspondence between the crystal structure of Alq_3 and the photoluminescence property. Also, it has been a practice to use different dopants in Alq_3 emitting layers to obtain desired colours [83]. Such Alq_3 systems are in general known as solvated Alq_3.

Considering the above stated facts, it becomes important to have insight about the structure of Alq_3 in both the solvated and the unsolvated form and about the intra molecular and intermolecular interactions. Since Alq_3 has an Al^{3+} ion in the centre, one can make use of it as a probe to monitor the electronic distribution in the molecule. ^{27}Al is well suited for solid-state NMR because of its high natural abundance (100%) and relatively large gyromagnetic ratio. The study of quadrupolar parameters with solid-state NMR can provide a wealth of information about the local environment around quadrupolar nuclei, as the quadrupolar parameters show strong dependence on the neighbouring electronic environment.

We investigated three types of Alq_3 samples: (a) α phase (containing the meridional isomer), (b) δ phase (containing the facial isomer), and (c) solvated phase (containing ethanol in the crystal lattice) using solid-state NMR combined with density functional theory (DFT) based quantum chemical calculation. We showed with the two-dimensional (2D) Multiple Quantum Magic Angle Spinning (MQMAS) [14] experiments that in all the polymorphs, ^{27}Al is present in a single crystallographic site which was clearly suggested by the presence of single ridges along the indirect dimensions of the spectra. We further demonstrated that although the fluorescence emission spectra of that

of the α phase and the solvated phase are almost identical the local environment around ^{27}Al in solvated phase is completely different from that in the α phase with the use of both 1D MAS and 2D MQMAS experiments. We also made use of DMFIT [135] program to model the 1D MAS spectra of all the polymorphs to extract the quadrupolar parameters. In addition, the anisotropic slices of the peaks in 2D MQMAS spectra were modelled using the DMFIT program to extract the quadrupolar parameters and isotropic chemical shifts. We further showed the result obtained from DFT based quantum-chemical calculation done on isolated molecule and show that the correspondence with the experimental results improve when the calculation is done under the solvation model (IPC model).

We also showed by the use of both 1D MAS and 2D MQMAS that if the ethanol is removed from the solvated Alq$_3$ crystal matrix its crystal structure becomes similar to that of the α phase of Alq$_3$ which is evident from their similar quadrupolar parameters. X-ray diffraction studies also showed similar results. It was also observed that the change of phase occurs exactly at the temperature at which ethanol is known to come out of the solvated Alq$_3$ crystal matrix.

Application of Symmetry-Sequence and High-Resolution NMR Techniques for Simultaneous Extraction of Dipolar and Quadrupolar Parameters

Interest in ^{17}O (I=5/2) NMR has increased markedly in the last few years, particularly for characterizing amorphous inorganic oxide gels and in the measurement of hydroxyl groups and water molecules in peptides and biological samples. The study of ^{1}H-^{17}O pairs is of particular interest for the investigation of hydrogen bonded systems since the ^{17}O quadrupolar interaction is sensitive to any perturbation in the local environment. Further one can obtain the magnitude of the ^{1}H-^{17}O dipole coupling and also the relative

orientation of dipolar coupling tensor with respect to the quadrupolar coupling tensor.

Although the magnitude of ^{1}H-^{17}O dipolar coupling of directly bonded hydroxyl groups is quite large (of the order of 15 kHz) it is difficult to observe them direcly because of the presence of ^{1}H- ^{1}H dipolar coupling. This difficulty can be removed by the use of symmetry based recoupling sequences. By choosing suitable symmetry numbers it is possible to selectively recouple only ^{1}H-^{17}O dipolar coupling while decoupling the ^{1}H- ^{1}H dipolar coupling.

We demonstrated quadrupolar-dipolar (QD) correlation spectra on ^{17}O enriched Brucite sample. We exploited symmetry based recoupling sequence of the type RN$_n^v$ [**?**] at proton Larmor frequency. One can choose suitable values for v, N, and n using the selection theorem for symmetry sequences to simultaneously recouple ^{1}H-^{17}O dipolar coupling and decoupling the homonuclear dipolar coupling between ^{1}H- ^{1}H. We used recoupling sequence of the type R18$_2^5$. The R18$_2^5$ sequence consists of a repetetion of two pulse element $180_{50}180_{-50}$ where the subscript denotes phase angle. The nutation rf of the pulses is 4.5 times of the MAS rate.

We showed that two-dimensional QD correlation spectra can be obtained by applying spin-echo sequence on ^{17}O while applying R18$_2^5$ symmetry sequence on ^{1}H. The QD correlation spectra show strikingly unique shape which clearly reflects the fact that dipolar coupling constant varies across the quadrupolar pattern. Hence from the correlation spectra one can obtain the magnitude of the dipolar coupling constant at any point of the quadrupolar powder pattern. We also obtained similar correlation spectra by combining Satellite Transition Magic Angle Spinning (STMAS) [**?**] pulse sequence on ^{17}O and symmetry sequence on ^{1}H. We further combined the symmetry sequence with the Triple Quantum Magic Angle Spinning (3QMAS) sequence, and as expected we obtained similar QD correlation spectra but the magnitude of the dipolar coupling constant at any point of the quadrupolar powder pattern is scaled by almost 3 times from that obtained using STMAS or spin-echo on ^{17}O.

We then combined STMAS and $R18_2^5$ sequence in three dimensional fashion to simultaneously obtain the information about the quadrupolar parameters and dipolar interaction. From the 3D experiment as expected we simultaneously obtained the QD correlation spectrum and the high-resolution two dimensional STMAS spectrum from which we extracted the quadrupolar parameters such as isotropic quadrupolar shifts, quadrupolar coupling constant and asymmetry parameter. We then did a series of 2D numerical simulations by varying the relative orientation of dipolar coupling tensor with respect to the quadrupolar coupling tensor using the quadrupolar parameters obtained from the 3D experiment to match the experimental QD correlation spectrum. From the simulation we concluded that the dipolar tensor and quadrupolar tensor in our system is coaxial.

Structural Characterization of Zeolite ZSM-5 Using Sensitivity Enhanced ^{29}Si Double-Quantum Spectroscopy

The study of ^{29}Si for structural elucidation of zeolites is often hindered by the poor sensitivity of ^{29}Si due to its low gyromagnetic ratio and low natural abundance. The detection sensitivity becomes even poor for systems which lack long range orders resulting in a distribution of isotropic chemical shifts which causes line broadening. Therefore, ^{29}Si observation is often beset with very poor detection sensitivity due to the disordered nature of the samples. Thus, in many cases of practical relevance, it is a prerequisite for the analysis to have double-quantum (2Q) recoupling experiments with enhanced ^{29}Si observation sensitivity.

Implementation of Carr-Purcell-Meiboom-Gill (CPMG) [51,52] sequence has proved to be highly successful method for sensitivity enhancement of second order broadened lines of quadrupolar nuclei. Similarly, in our present case also the sensitivity problem can be alleviated to a great extent by implementing a CPMG train of π pulses within

the acquisition period of the dipolar recoupling experiment. The multiple-pulse CPMG sequence refocuses the inhomogeneously broadened MAS spectral lines and entails repeated generation of spin echoes, which can be co-added to enhance the signal intensity.

In our study we used POST-C7 [152] double quantum dipolar recoupling sequence for 1Q-2Q correaltion experiment to establish the ^{29}Si-^{29}Si connectivity within the zeolite ZSM-5 framework. The effectiveness of the POST-C7 for double-quantum excitation can be attributed to the low chemical shift anisotropy (CSA) associated with the ^{29}Si in our system and also the fact that in our system ^{1}H-^{29}Si heteronuclear dipolar coupling is also relatively small. We further demonstrated that ^{29}Si dipolar coupled 1Q-2Q correlation spectra can be obtained under magic angle spinning with 3.5 fold enhanced sensitivity achieved by the acquisition of successive spin-echos created by CPMG train of π pulses applied at the ^{29}Si larmor frequency. We observed that maximum enhancement was obtained by the application of 14 CPMG train of π pulses with 16 ms of inter pulse delays. The sensitivity enhancement provided in the as-synthesized ZSM-5 high silica zeolite has enabled the identification of the dipolar correlations at each resolved silicon sites and has led to the resonance assignments in the MAS spectra.

List of Publications

1. Mithun Goswami, and P. K. Madhu, Sensitivity Enhancement of the Central Transition of Half-Integer Spin Quadrupolar Nuclei: Features of Multiple Fast Amplitude-Modulated Pulse Transfer. J. Magn. Reson. **192**, (2008) 230-234.

2. Mithun Goswami, Pabitra K. Nayak, N. Periasamy, and P. K. Madhu. Characterisation of Different Polymorphs of Tris(8-Hydroxyquinolinato)Aluminium(III) Using Solid-State NMR and DFT Calculations. Chemistry Central Journal **3:15**, 2009.

3. Mithun Goswami, P. K. Madhu, J. Dittmer, N. C. Nielsen, S. Ganapathy. Sensitivity Enhancement of ^{29}Si Double Quantum Dipolar Recoupling Spectroscopy by Carr-Purcell-Meiboom-Gill Acquisition Method. Chem. Phys. Lett. **478**, (2009) 287-291.

4. Mithun Goswami, and P. K. Madhu, Application of symmetry based recoupling method and high-resolution solid-state NMR methods for quadrupolar nuclei for simultaneous extraction of dipolar and quadrupolar information. Manuscript in preparation.

5. S. Paul, R. S. Thakur, M. Goswami, A. C. Sauerwein, S. Mamone, M. Concistrè, H. Förster, M. H. Levitt, and P. K. Madhu, Supercycled homonuclear dipolar decoupling sequences in solid-state NMR, J. Magn. Reson. **197**, (2009) 14-19.

Chapter 1

Introduction

1.1 General Introduction

Nuclear magnetic resonance, or NMR [1,2] as it is abbreviated, is a phenomenon which occurs when the nuclei of certain atoms are immersed in a static magnetic field and exposed to a second oscillating magnetic field causing transition between energy levels of a nucleus arising from its spin angular momentum.

Nuclear magnetic resonance was first described and measured in molecular beams by Isidor Rabi in 1938 [3] and in 1946, Felix Bloch and Edward Mills Purcell expanded the technique for use on liquids and solids, for which they shared the Nobel Prize in physics in 1952. Since then NMR has become an invaluable tool for investigation of matter. NMR which was initially only viewed as a physical phenomena has spread out to the fields of Chemistry, Biology, and Medicine. It has been applied in diverse areas such as brains, bones, ceramics, liquid crystal, protein folding, superconductors, zeolites, catalysis, organic light emitting diodes, polymers, and quantum computing. Application of NMR in such diversified fields proves its range and power. Perhaps no other field can boast of applications in such incredibly large range of areas. The field is still diversifying and new methodologies and techniques are being introduced to open up new areas of study.

Along with the various application of NMR, huge efforts are being put in, in the development of new techniques and methodologies of NMR for its successful applications. New techniques are being developed for the sensitivity enhancement of the NMR signal and the improvement of signal resolution to address the existing problems and also to pave the way for new avenues.

NMR generally consists of two realms: liquid state NMR and solid state NMR. In solution NMR, the molecules in the sample tumble randomly at rates fast enough ($\sim$ GHz in frequency) to average out anisotropic couplings. The advantage of this inherent isotropy (same in all directions) is that the NMR spectrum appears as a set of narrow, well defined lines with sharp transitions. The disadvantage of this is that orientation-dependent (anisotropic) information is lost. However in solution state NMR, some of this information can be regained by orienting the molecules partially, for example by adding phage particles that line up in the magnetic field [4].

In solids, on the other hand all of the anisotropic features are present in their full measure resulting in a broad lines. The presence of broad NMR lineshapes, once thought to be a hindrance for obtaining high resolution NMR spectroscopy, actually provides much information on chemistry, structure and dynamics in the solid state. Since the conception of it, the "Holy Grail" of solid state NMR is to get liquid like spectra while retaining the anisotropic informations. A host of techniques have been developed to this effect like Magic Angle Spinning (MAS) [5], Cross Polarization methods to transfer polarization from abundant nuclei to rare nuclei [6, 7], and multipulse techniques [8].

This thesis addresses the work done on sensitivity enhancement schemes for both spin-1/2 and spin>1/2 or quadrupolar nuclei. It also includes the application of high resolution NMR techniques for quadrupolar nuclei together with quantum chemical calculations as a tool for the characterization of a organic light emitting diode. It further includes attempts which were made to combine high resolution NMR techniques for quadrupolar nuclei with dipolar recoupling schemes in such way to simultaneously pre-

dict both dipolar information between a ^{1}H-^{17}O pair and also quadrupolar information of ^{17}O. Current work also introduces methods to easily characterize zeolites using ^{29}Si NMR.

In this chapter discussions will be made over the different NMR interactions with special emphasis on the quadrupolar interaction. A basic outline is given next about the high resolution NMR techniques for quadrupolar nuclei. A brief description about sensitivity enhancement schemes for both spin-1/2 and spin>1/2 is considered next following which dipolar recoupling techniques involving symmetry principles is highlighted.

1.2 Interactions in NMR

A theoretical description of a single spin system or a collection of spin systems begins with the spin Hamiltonians [9]. The total Hamiltonian, $\mathcal{H}$, for a spin system is a summation of all the individual Hamiltonians that describes particular interactions, $\mathcal{H}_\lambda$.

$$\mathcal{H} = \sum_\lambda \mathcal{H}_\lambda \tag{1.1}$$

Here the summation is over all interactions.

The spin interaction Hamiltonians can be divided into two classes,

- $\mathcal{H}_{ext}$: This Hamiltonian describes the interaction between the spin and the external fields such as the static magnetic field ($\mathcal{H}_Z$) or the time dependent radio frequency field ($\mathcal{H}_{RF}$).

- $\mathcal{H}_{int}$: This Hamiltonian describes all the direct and indirect interactions of the spins with internal fields. These include the dipolar ($\mathcal{H}_{DD}$), scaler ($\mathcal{H}_J$), chemical shift ($\mathcal{H}_{CS}$), and quadrupolar ($\mathcal{H}_Q$) Hamiltonians.

One of the most interesting feature of NMR is that the external interactions are usually much larger than the internal interactions which means that the spins are more

strongly coupled to the external apparatus than with their own molecular environment.

Total internal nuclear spin Hamiltonian, $\mathcal{H}_{int}$ can be described as the summation of the different nuclear spin interactions as,

$$\mathcal{H}_{int} = \mathcal{H}_J + \mathcal{H}_{CS} + \mathcal{H}_{IS} + \mathcal{H}_{II} + \mathcal{H}_Q \tag{1.2}$$

- $\mathcal{H}_J$: Indirect magnetic interactions of nuclear spins with each other, through the involvement of the electrons.

- $\mathcal{H}_{CS}$: Indirect magnetic interaction of the external magnetic field with the nuclear spin through the involvement of electrons.

- $\mathcal{H}_{IS}$: Heteronuclear direct dipolar coupling interactions between spin-**I** and spin-**S**.

- $\mathcal{H}_{II}$: Homonuclear direct dipolar coupling interactions between a pair of spin-**I**.

- $\mathcal{H}_Q$: Quadrupolar interactions for **I** and **S** spins.

In the solid state, all of these interactions can make contributions causing spin state energies to shift resulting in direct manifestation of these interactions in the NMR spectra. For most cases, we can assume the high-field approximation; that is, the Zeeman interaction and other external magnetic fields are much greater than internal NMR interactions. Correspondingly, these internal interactions can be treated as perturbations on the Zeeman Hamiltonian, $\mathcal{H}_Z$.

All NMR interactions are anisotropic and their three dimensional nature can be described by second-rank Cartesian tensors, which are 3×3 matrices.

$$\mathcal{H} = I.\bar{A}.S = \begin{pmatrix} I_x & I_y & I_z \end{pmatrix} \cdot \begin{pmatrix} A_{11} & A_{12} & A_{13} \\ A_{21} & A_{22} & A_{23} \\ A_{31} & A_{32} & A_{33} \end{pmatrix} \cdot \begin{pmatrix} S_x \\ S_y \\ S_z \end{pmatrix} \tag{1.3}$$

Here I_x, I_y, and I_z refers to the spin angular angular momentum components of spin **I** and S_x, S_y, and S_z represent the spin angular momentum components of coupled spin **S** for two spin interactions. $\bar{A}$ is a 3 × 3 matrix representing nuclear spin interactions.

The NMR interaction tensor describes the orientation of an NMR interaction with respect to the Cartesian axis system of the molecule. These tensors can be diagonalized to yield tensors that have three principal components which describe the interaction in its own principal axis system (PAS):

$$\mathcal{H}_{PAS} = \begin{pmatrix} I_x & I_y & I_z \end{pmatrix} \cdot \begin{pmatrix} A_{xx} & 0 & 0 \\ 0 & A_{yy} & 0 \\ 0 & 0 & A_{zz} \end{pmatrix} \cdot \begin{pmatrix} S_x \\ S_y \\ S_z \end{pmatrix} \tag{1.4}$$

Such interaction tensors are commonly pictured as ellipsoids or ovaloids, with the A_{zz} component assigned to the largest principal component.
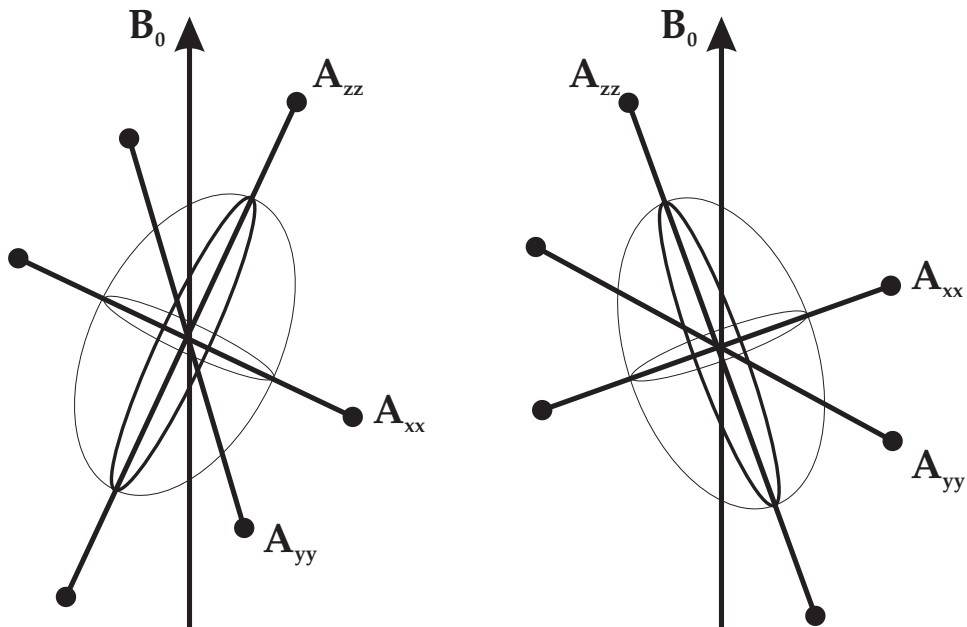
Figure 1.1: Ellipsoid representation of an interaction tensor. The principle axes of the ellipsoid coincides with the principle axes frame of the interaction tensor.

Using Cartesian tensors, the spin part of the Hamiltonian (which is the same as in solution NMR) is separated from the spatial anisotropic dependence, which is described by the second-rank Cartesian tensor.

All anisotropic NMR interaction Hamiltonians can be expressed by using Eq. 1.3, where the orientation dependence of the interactions are represented by the second-rank Cartesian tensors often referred to as *coupling tensors*.

The scaler coupling Hamiltonian, $\mathcal{H}_J$, that carries the information between spins by bonded electrons can be represented as,

$$\mathcal{H}_J = \sum_{i \neq j} I_i . \overline{J} . I_j \tag{1.5}$$

Although the magnitude of $\mathcal{H}_J$ is small compared to other nuclear spin interactions it causes the spin-spin splitting in high resolution NMR spectra. Here $\overline{J}$ represent the scaler coupling tensor.

Similarly the chemical shift Hamiltonian, $\mathcal{H}_{CS}$, can be described as

$$\mathcal{H}_{CS} = \gamma I . \overline{\sigma} . B_0 \tag{1.6}$$

in frequency units, where $\overline{\sigma}$ is the chemical shift tensor . This provides the frequency shift measured in high resolution spectra. γ is the gyromagnetic ratio of the spin **I** and **B**$_0$ represent the externally applied magnetic field.

The dipolar Hamiltonian, $\mathcal{H}_D$, again in frequency units can be written as

$$\mathcal{H}_D = \sum_{i<j} \frac{\mu_0}{4\pi} \frac{\hbar \gamma_i \gamma_j}{r_{ij}^3} \left\{ \vec{I_i} . \vec{I_j} - 3(\vec{I_i} . \hat{e}_{ij})(\vec{I_j} . \hat{e}_{ij}) \right\} = \sum_{i=j} I_i . \overline{D} . I_j \tag{1.7}$$

where r_{ij}^3 is the distance between the two spins i and j and $\hat{e}_{ij}$ is the unit vector along $\vec{r_{ij}}$. $\overline{D}$ represent the dipolar coupling tensor which describes the strength and orientation dependence of the dipolar interaction between two coupled spins.

The quadrupolar interaction is slightly different than other nuclear spin interactions

since it is an interaction between a nuclear electric quadrupole moment and an electric field gradient rather than an interaction between nuclear dipole moment and a magnetic field. Nevertheless, the quadrupolar Hamiltonian, $\mathscr{H}_Q$, can be expressed in a similar form to those for the chemical shift or dipolar coupling as

$$\mathscr{H}_Q = \frac{eQ}{2I(2I-1)\hbar} \sum_i I.\overline{V}.I \tag{1.8}$$

where $\overline{V}$ is the electric field gradient tensor and eQ is the nuclear electric quadrupole moment.

1.2.1 Quadrupolar Interaction

Quadrupolar nuclei have a spin $> 1/2$, and an asymmetric distribution of nucleons giving rise to a non-spherical positive electric charge distribution; this is in contrast to spin-1/2 nuclei, which have a spherical distribution of positive electric charge [10].
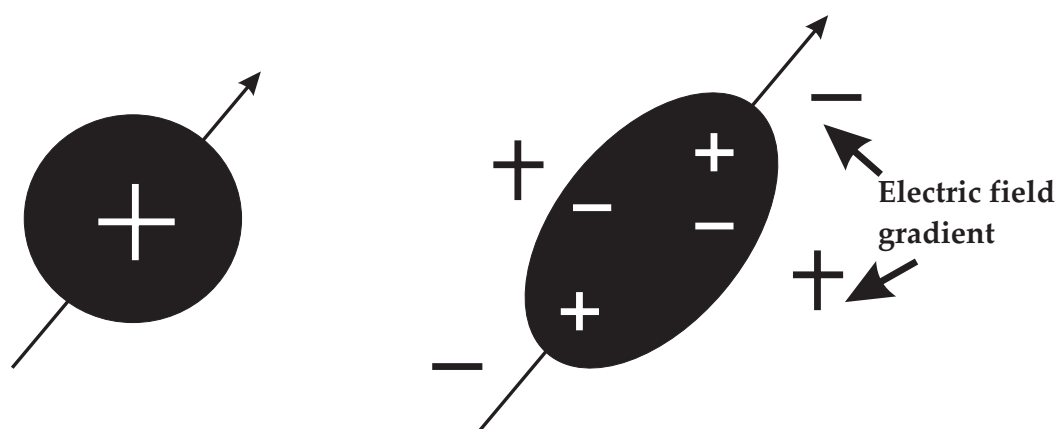
Figure 1.2: Comparison of charge distribution between spin-1/2 and spin $> 1/2$ systems.

The asymmetric charge distribution in the nucleus is described by the nuclear electric

quadrupole moment, *eQ*, which is measured in barn [11]. *eQ* is an instrinsic property of the nucleus, and is the same regardless of the environment.

Quadrupolar nuclei interact with electric field gradients (EFGs) in the molecule: EFGs are spatial changes in electric field in the molecule. Like the dipolar interaction, the quadrupolar interaction is a ground state interaction, but is dependent upon the distribution of electric point charges in the molecule and resulting EFGs.
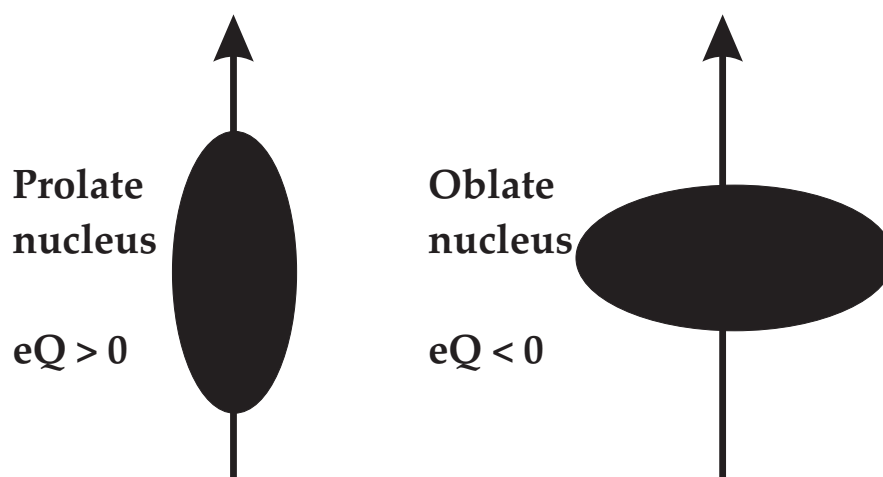
Figure 1.3: Dependence of nuclear electric quadrupolar moment, eQ on the shape of nucleus.

The electric field gradient (EFG) tensors at the quadrupolar nucleus can be described by a symmetric traceless tensor, V, which can also be diagonalized:

$$V = \begin{pmatrix} V_{11} & V_{12} & V_{13} \\ V_{21} & V_{22} & V_{23} \\ V_{31} & V_{32} & V_{33} \end{pmatrix}$$

$$V^{PAS} = \begin{pmatrix} V_{xx} & 0 & 0 \\ 0 & V_{yy} & 0 \\ 0 & 0 & V_{zz} \end{pmatrix} \tag{1.9}$$

where V^{PAS} represent the EFG tensor in its principle axis and V_{xx}, V_{yy} and V_{zz} are the principal components of the EFG tensors.

The principal components of the EFG tensor are defined such that $|V_{xx}| \leqslant |V_{yy}| \leqslant |V_{zz}|$. Since the EFG tensor is traceless, isotropic tumbling in solution averages it to zero (unlike J and σ), i.e. it has no isotropic component. Thus V_{zz} (= eq) is the anisotropy of the EFG tensor.

The magnitude of the quadrupolar interaction is given by the nuclear quadrupole coupling constant:

$$\chi_Q = eQ.V_{zz}/h \tag{1.10}$$

The asymmetry of the quadrupolar interaction is given by the asymmetry parameter, $\eta = (V_{xx} - V_{yy})/V_{zz}$, where $0 \leqslant \eta \leqslant 1$ and $V_{zz} =$ eq. If $\eta = 0$, the EFG tensor is axially symmetric.

For a quadrupolar nucleus in the centre of a spherically symmetric molecule, the EFGs cancel one another resulting in very small EFGs at the quadrupolar nucleus. As the spherical symmetry breaks down, the EFGs at the quadrupolar nucleus grow in magnitude.

The magnitude of quadrupolar Hamiltonian, $\mathcal{H}_Q$, besides being larger than all other anisotropic NMR Hamiltonians, is often stronger than the radio frequency (rf) fields used in NMR. Hence for an analysis of quadrupolar spectra, the first two terms in the expansion of $\mathcal{H}_Q$ are considered: the first-order, $\mathcal{H}_Q^{(1)}$, and second-order, $\mathcal{H}_Q^{(2)}$, following standard perturbation theory.

The first order quadrupolar interaction, $\mathcal{H}_Q^{(1)}$ affects only the satellite transitions (m $\longrightarrow$ m±1, where |m|= 1/2, 3/2, 5/2 etc) causing huge shifts (of the order of MHz) in
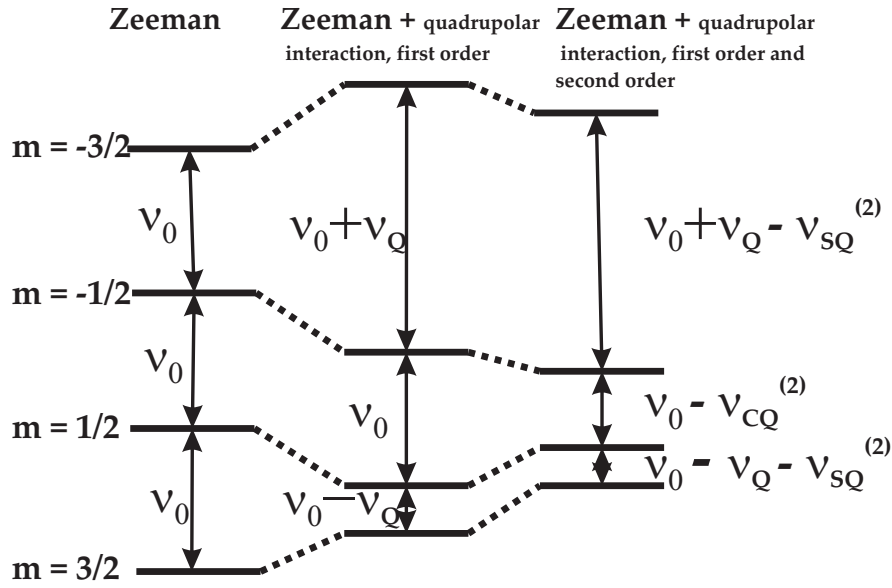
Figure 1.4: Energy level diagram of spin-3/2 system in presence of zeeman field, first order quadrupolar interaction and second order quadrupolar interaction.

the energy levels. As a result in the case of integer spins, the observable satellite transitions are broadened extensively making their observations very hard. However the symmetric transitions (m $\longrightarrow$ -m) are only affected by much smaller second order quadrupolar interactions, $\mathcal{H}_Q^{(2)}$, as a result the observable single quantum transition (+1/2 $\longrightarrow$ -1/2) for half integer spin quadrupolar nuclei provides with relatively narrower powder line shape. Fig 1.3 shows the energy level diagram of spin-3/2 system in presence of zeeman field, first order quadrupolar interaction and second order quadrupolar interaction with $\nu_{CQ}^{(2)}$ and $\nu_{SQ}^{(2)}$ denoting the second order quadrupolar frequency of the central and satellite transitions, respectively.

The quadrupolar frequency ν_Q in units of Hz or ω_Q in units of rad s^{-1}, is given by [9]

$$\nu_Q = \frac{\omega_Q}{2\pi} = \frac{3\chi}{2I(2I-1)} \tag{1.11}$$

Hence for I=3/2, ν_Q= 1/2χ and for I=5/2, ν_Q= 3/20χ. The first order quadrupolar interaction scale as ν_Q whereas the second order quadrupolar interaction scale as $\frac{\nu_Q^2}{\nu_0}$

where ν_0 represents the Larmor frequency. As a result higher the static magnetic field higher will be the resolution.

The quadrupolar Hamiltonian described in Eq. (1.5) can be rewritten in terms of irreducible spherical tensor operators [9, 12] is given in Eq. (1.9) as

$$\mathcal{H}_Q = \frac{\nu_Q}{3} \sum_{k=-2}^{2} (-1)^k T_q^{(2)} V_{-q}^{(2)} \tag{1.12}$$

where

$$T_0^{(2)} = \sqrt{\frac{1}{6}} [3I_z^2 - I(I-1)]$$

$$T_{(2)}^{(\pm 1)} = I_z I_\pm = I_\pm I_z$$

$$T_{(2)}^{(\pm 2)} = I_\pm^2 \tag{1.13}$$

The quadrupolar coupling tensor in the laboratory frame, $V_q^{(2)}$ and in the principle axis frame, $\rho_m^{(2)}$ is related via the Euler angles α, β, γ as

$$V_q^{(2)} = \sum_{q'=-k}^{k} \rho_{q'}^{(2)} D_{q'q}^{(2)}(\alpha, \beta, \gamma) \tag{1.14}$$

Where $D_{q'q}^{(k)}(\alpha, \beta, \gamma)$ represents the Wigner matrix elements [13].

In laboratory frame the quadrupolar interaction can be treated as perturbation to the external Zeeman field and can be treated as summation of first and second order quadrupolar terms,

$$\mathcal{H}_Q = \mathcal{H}_Q^{(1)} + \mathcal{H}_Q^{(2)}$$

$$\mathcal{H}_Q^{(1)} = \frac{\nu_Q}{3} T_0^{(2)} V_0^{(2)} = \frac{h\nu_Q'}{6} [3I_z^2 - I(I+1)]$$

$$\mathcal{H}_Q^{(2)} = \frac{h\nu_Q^2}{9\nu_0} \{ 2I_z [2I_z^2 - I(I+1) + \frac{1}{4}] V_{-1}^{(2)} V_1^{(2)} + I_z [I_z^2 - I(I+1) + \frac{1}{2}] V_{-2}^{(2)} V_2^{(2)} \} \tag{1.15}$$

Where $v_Q^{'}$ is represented as,

$$v_Q^{'} = v_Q \left(\frac{3\cos^2 \beta - 1}{2} + \frac{\eta}{2} \sin^2 \beta \cos 2\alpha \right) \tag{1.16}$$

When in MAS, to transform the PAS of a quadrupolar system to the lab frame, first one needs to transform the PAS to the rotor frame using proper Wigner matrix $D(\alpha, \beta, \gamma)$ where the angles α, β, γ represents the angles relating the PAS to the rotor frame. Then it is transformed to lab frame using Wigner matrix of the form $D(\omega_r t, \theta_{MA}, 0)$ where $\omega_r t$ represents the phase obtained by the rotor when spinning at a frequency of ω_r at an angle of θ_{MA} (magic angle) with the static magnetic field. Hence the quadrupolar coupling tensor in laboratory frame, $V_q^{(2)}$ may be described as the product of two Wigner matrices as follows,

$$V_q^{(2)} = \sum_{m=-2}^{2} D_{mq}^{(2)}(\omega_r t, \theta_{MA}, 0) \sum_{n=-2}^{2} D_{nm}^{(2)}(\alpha, \beta, \gamma) \rho_n^{(2)}. \tag{1.17}$$

Hence by putting the values of $V_q^{(2)}$ in Eq. (1.12) one may obtain the expression for the symmetric transitions as

$$v_{m,-m} = \sum_{l=0,2,4} v_Q^l(\alpha, \beta, \gamma) C_l(I, m) P_l(\cos \theta_{MA}) \tag{1.18}$$

Here $P_l(\cos \theta_{MA})$ is the Legendre polynomial of rank l, and C_l (I, m) are zero-, second- and fourth-rank (spin) coefficients depending on the spin quantum number I and order 2m of the transition. The expressions for C_l (I, m) can be found in [14] and v_Q^l represent the orientation dependent second rank and fourth rank frequencies responsible for line broadening. Eq. (1.18) forms the basis of high resolution Multiple Quantum Magic Angle Spinning (MQMAS) [14] experiment of which we shall discuss about in the next section.

1.3 High Resolution NMR Spectroscopy for Quadrupolar Nuclei

The MAS spectra of central transitions are only affected by second order quadrupolar interactions. However they still show a significant line broadening as it is evident from Fig. 1.5 and can hardly be considered as high resolution spectra. The reason for line broadening is clear from Eq. (1.18). The product of the orientation dependent terms containing both second and fourth rank Legendre polynomials is the source of line broadening.

$$P_2(\cos\theta) = (3\cos^2\theta - 1)$$

$$P_4(\cos\theta) = (35\cos^4\theta - 30\cos^2\theta + 3) \tag{1.19}$$

It is evident from above equations and also from Fig. 1.6 that there is no common root for both of them. Hence a rotor spinning at magic angle ($\theta_{MA}= 54.74^0$) will only make $P_2(\cos\theta)$ terms to vanish while the anisotropic contributions of terms containing $P_4(\cos\theta)$ will remain. This is the reason behind the line broadening of central transition under MAS.

To achieve high resolution spectra of quadrupolar nuclei one needs to come up with a method which will make all the anisotropic contributions to go to zero. The first high resolution spectra for quadrupolar nuclei were achieved by two methods, namely Double Rotation (DOR) [15] and Dynamic Angle spinning (DAS) [16, 17].

1.3.1 Double Rotation

DOR is a one dimensional experiment which involves two rotors, one outer rotor inclined at an angle of θ_1 with respect to the static magnetic field and an inner rotor containing the sample making an angle of θ_2 with the static magnetic field, this allows the simultaneous rotation of the sample about two different axes.. The high resolution condition in
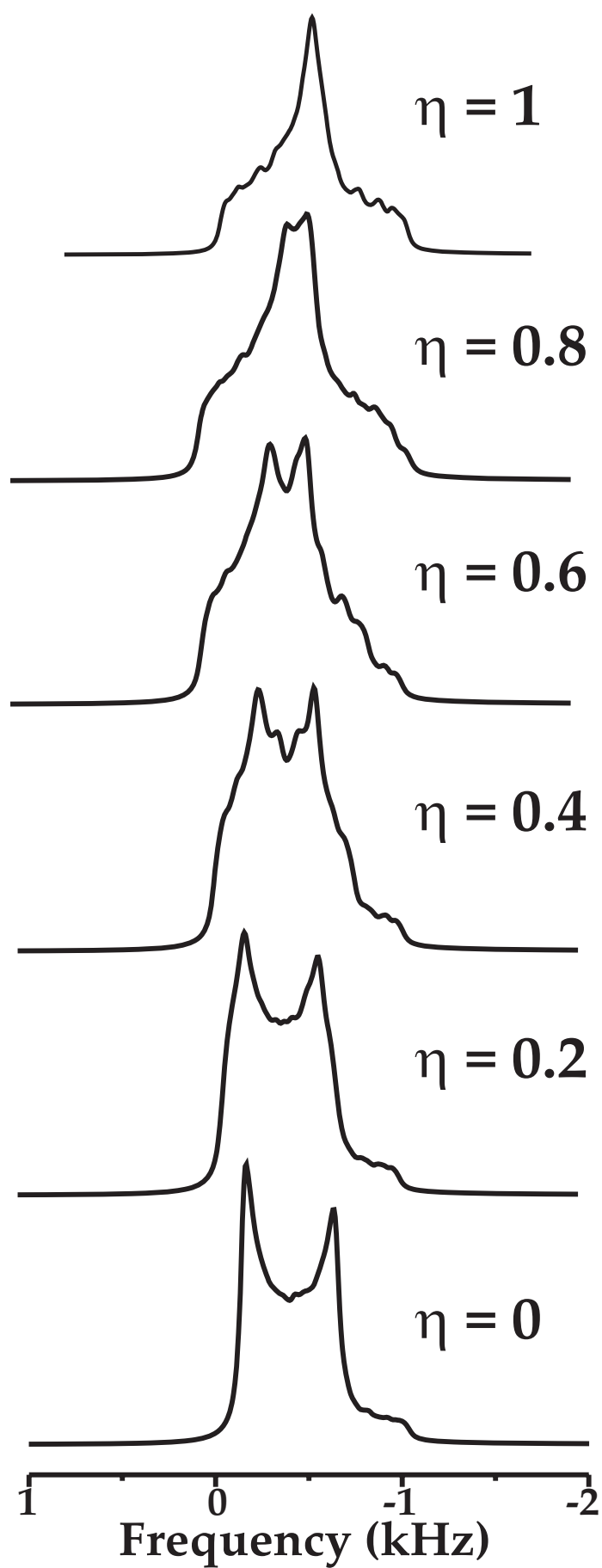
Figure 1.5: Powder simulation of central transitions under MAS of a spin-5/2 system with different asymmetry, η, parameter.
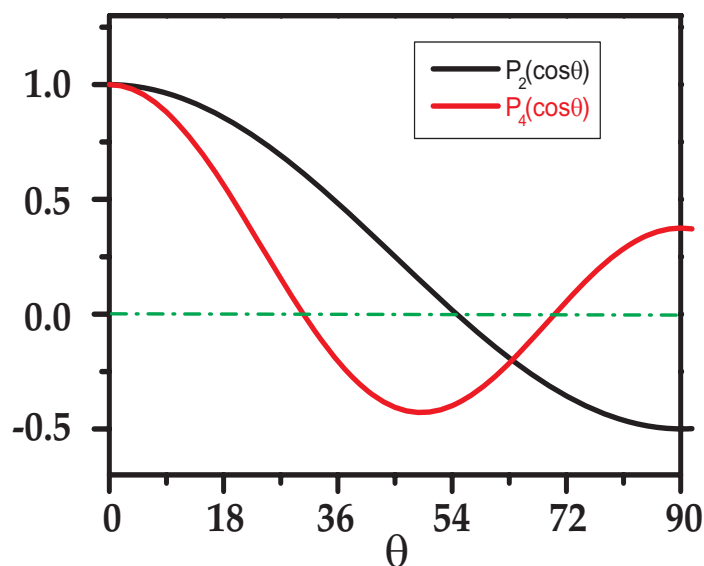
Figure 1.6: Plot of second and fourth rank Legendre polynomials.

the DOR experiment can be described as follows,

$$P_2(\cos\theta_1)P_2(\cos\theta_2) = 0$$

$$P_4(\cos\theta_1)P_4(\cos\theta_2) = 0, \tag{1.20}$$

and their solutions are either,

$$\{\theta_1, \theta_2\} = \{54.73^0, 30.56^0\} \, or$$

$$\{\theta_1, \theta_2\} = \{54.73^0, 70.12^0\}. \tag{1.21}$$

Eq. (1.21) shows the two set of angles at which two rotors must be inclined to remove the $P_2(\cos\theta)$ and $P_4(\cos\theta)$ spatial terms of second order quadrupolar interactions and achieve a high resolution spectra. Under DOR conditions, all the second-order quadrupolar coupling is removed, except for its isotropic component, thus leaving a sharp isotropic peak flanked by a series of sidebands spaced at integer multiples of the

outer rotor frequency. The isotropic quadrupolar shift (l = 0) is given explicitly as,

$$v_{iso}^{(2)} = \frac{1}{30} \frac{v_Q^2}{v_0} \left[I(I+1) - \frac{3}{4} \right] \left(1 + \frac{1}{3} \eta^2 \right) \tag{1.22}$$

1.3.2 Dynamic Angle Spinning

Dynamic-angle spinning (DAS) is an alternative technique for removing the second-order quadrupolar coupling. Like DOR, DAS seeks to remove the second-order quadrupolar coupling by spinning the sample at multiple angles. However, DAS spins sequentially at two different angles rather than simultaneously. DAS is a two-dimensional (2D) experiment in which the rotor is spun for a time t_1 at an angle θ_1, then the magnetisation is stored along the z-axis while the spinner angle is chenged ($\sim$ 30 ms), and finally coherence is transferred back to the central transition with rotor spinning at an angle θ_2. The two rotor axis angles are chosen in such a way that the conditions,

$$P_2(\cos \theta_1) + P_2(\cos \theta_2) = 0$$

$$P_4(\cos \theta_1) + P_4(\cos \theta_2) = 0, \tag{1.23}$$

are satisfied.

One of the simple solutions of the above equation is $\{\theta_1, \theta_2\} = \{ 37.38^0, 79.19^0 \}$. In fact, there are an infinite number of so-called DAS angle pairs. It is no coincidence that the angles 37.38^0, 79.19^0 correspond to the symmetry of an icosahedron (dodecahedron). Just as MAS corresponds to the dynamic implementation of cubic symmetry [18], DAS is the dynamic realization of icosahedral symmetry [20].

1.3.3 Multiple Quantum Magic Angle Spinning

Both DAS and DOR are very good techniques for removing the effects of the second-order quadrupolar coupling in half-integer-spin quadrupolar nuclei. However these methods

are technically very demanding and are limited by several factors, such as in DOR experiments relatively low spinning rate of the outer rotor produces large number of sidebands. Similarly DAS experiments are limited by the fact that T_1 of the quadrupolar nuclei needs to be longer than the time taken by the rotor to change its angle. A technically simpler approach, known as multiple-quantum MAS (MQMAS) [14] capitalizes ingeniously on multiple-quantum coherence and coherence transfer with a standard MAS probe to remove $\mathscr{H}_Q^{(2)}$.

MQMAS is a 2D experiment where a high-resolution spectrum along the indirect dimension is correlated with its corresponding MAS spectrum in the detection dimension. This is achieved by simultaneously manipulating spin and spatial parts of the quadrupolar Hamiltonian. MAS takes the role of spatial averaging and removes the chemical shift anisotropy, CSA, the heteronuclear dipolar interactions, and the second rank elements of the second-order quadrupolar interaction, $\mathscr{H}_Q^{(2)}$. Radiofrequency pulses are used to manipulate the spin part of the $\mathscr{H}_Q^{(2)}$ and remove the anisotropic contributions of the fourth rank terms. An echo is formed by correlating the symmetric multiple quantum transitions with central transitions of all the crystallites in a powder simultaneously.

Using Eq. (1.18) the evolution undergone by a -m $\longrightarrow$ +m spin coherence after excitation can be described by a multirank expansion of its phase ϕ,

$$\phi(m, \theta, \alpha, \beta, t) = v^{CS} 2mt + v_Q^{(0)} C_0(I, m)t + v_Q^{(2)}(\alpha, \beta) C_2(I, m) P_2(\cos\theta)t + v_Q^{(4)}(\alpha, \beta) C_2(I, m) P_4(\cos\theta)t.$$

$$(1.24)$$

where θ is the angle of rotation axis with respect to the static magnetic field, B_0.

Now in a 2D experiment spin coherences evolve during time t_1 and then t_2. To remove all the anisotropic contributions from the phase ϕ and to obtain high resolution isotropic peaks following relations need to be satisfied,

$$v_Q^{(2)}(\alpha, \beta) C_2(I, m_1) P_2(\cos\theta_1)t_1 + v_Q^{(2)}(\alpha, \beta) C_2(I, m_2) P_2(\cos\theta_2)t_2 = 0$$

$$\nu_Q^{(2)}(\alpha,\beta)C_4(I,m_1)P_4(\cos\theta_1)t_1 + \nu_Q^{(2)}(\alpha,\beta)C_4(I,m_2)P_4(\cos\theta_2)t_2 = 0. \qquad (1.25)$$

Setting $\theta_1 = \theta_1 = \theta_{MA}$ and leaving $m_{1,2}$ as parameters, the above constraints reduce to

$$C_4(I,m_1)t_1 + C_4(I,m_2)t_2 = 0 \qquad (1.26)$$

Hence at a time $t_2 = -\frac{C_4(I,m_1)}{C_4(I,m_2)} t_1$ all the anisotropy are removed and quadrupolar echo is achieved for all the crystallites. Fig. 1.7 shows the typical two pulse MQMAS sequence with coherence pathways.
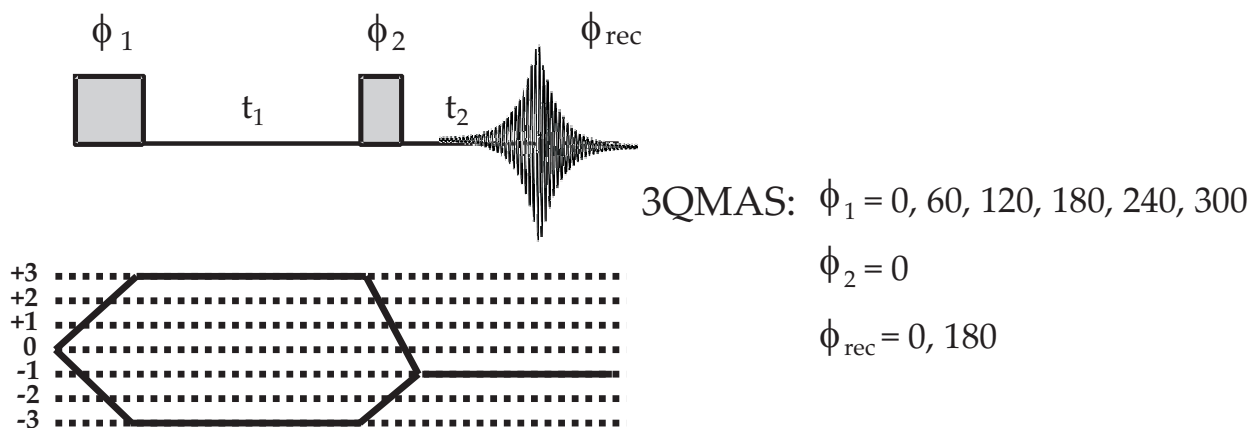
Figure 1.7: Pulse sequence diagram of 2D 3QMAS experiment with the phase cycling. ϕ_1 and ϕ_2 represent the phases of the excitation and conversion pulses.

Fig. 1.8 is a typical 2D spectrum of ^{23}Na in tri sodium citrate sample using split-t_1 variant of MQMAS [21]. The spectrum contains three ridges along the indirect or F_1 or isotropic dimensions indicating three crystallographically non equivalent sites.

1.3.4 Satellite Transition Magic Angle Spinning

In 2000, Gan proposed a new MAS-based method for obtaining high-resolution quadrupolar NMR spectra of solids [19]. This satellite-transition (ST) MAS experiment is similar
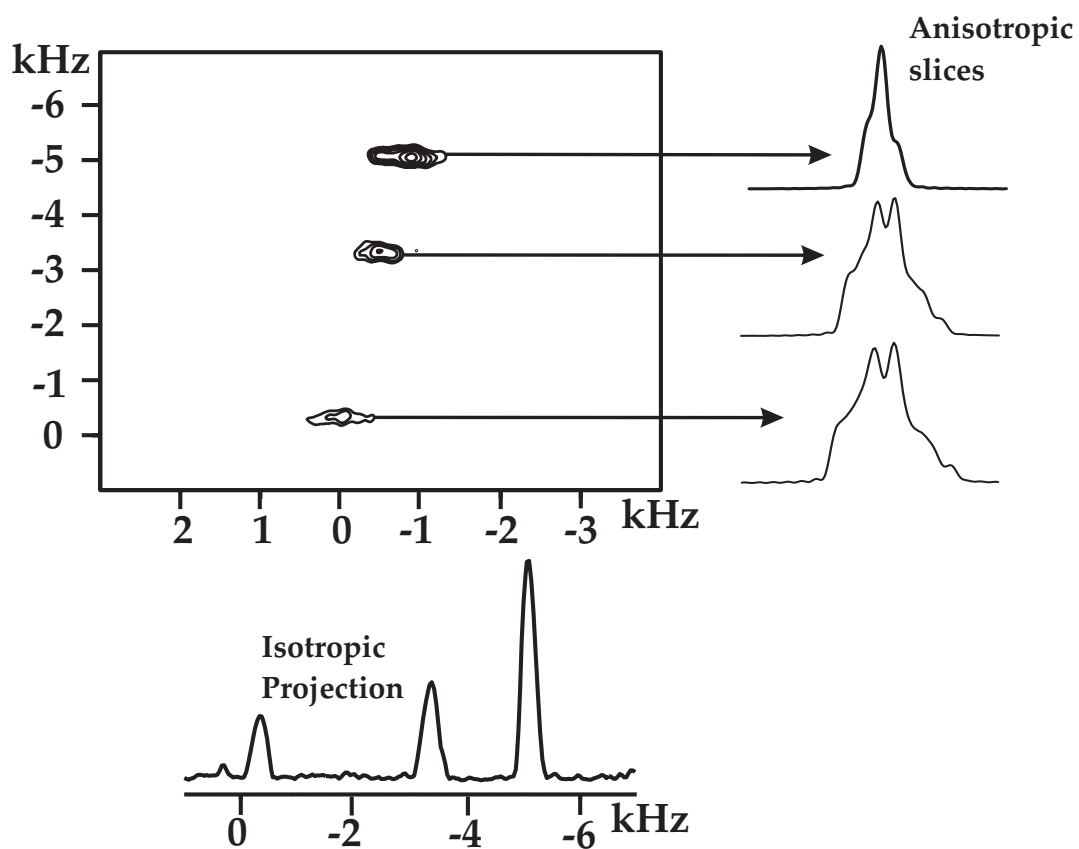
Figure 1.8: 2D 3QMAS spectrum of tri sodium citrate with isotropic projection and corresponding anisotropic slices.

to MQMAS in many ways, yet often yields significantly enhanced sensitivity. Yet so far it has not attracted the same level of interest as that of MQMAS. The reason behind that may be its reputation of being a more difficult experiment to perform than MQMAS since it requires precise setting of magic angle and rotor synchronized data acquisition. However MQMAS has a very poor sensitivity and the problem often accentuates in real systems. In such scenarios a method such as STMAS offers significantly improved sensitivity.

The satellite transitions in the spin manifold of quadrupolar nuclei can be efficiently excited using short radio frequency pulses and directly observed under MAS. At high magnetic field the effect of first and second order quadrupolar interaction can be expressed as,

$$E_{I,m}^{Q(1)} = -\omega_Q \left[I(I+1) - 3m^2 \right] \sum_{m=-2}^{m} a_{2,m}^{(1)} Y_{2,m}(\theta, \phi)$$

$$E_{I,m}^{Q(2)} = \frac{\omega_Q^2}{\omega_L} \sum_{l=0,2,4} C_l(I,m) \sum_{m=-l}^{l} a_{l,m}^{(2)} Y_{l,m}(\theta, \phi) \tag{1.27}$$

where ω_Q is quadrupolar frequency as given in Eq. 1.8 and ω_L is the Larmor frequency. The terms $a_{2,m}^{(1)}$ and $a_{l,m}^{(2)}$ have dependence on the asymmetry factor of the EFG tensor where as (θ, ϕ) denotes the polar angle between the magnetic field and the principle axis of the EFG tensor. As we have seen the central transition in any half integer quadrupolar nuclei is independent of the first order quadrupolar interaction where as the satellite transitions are affected by both $E_{I,m}^{Q(1)}$ and $E_{I,m}^{Q(2)}$. Spinning the sample at exactly magic angle will get rid of the anisotropic effects of the first order quadrupolar interaction as its anisotropic part has only second rank dependence, $Y_{2,m}(\theta, \phi)$. The second order effect $E_{I,m}^{Q(2)}$ contains the isotropic $l = 0$ and the anisotropic $l = 2, 4$ terms with the expansion coefficients

$$C_l(I,m) = C(22l, 1-1)\left[4I(I+1) - 8m^2 - 1\right]m + C(22l, 2-2)\left[2I(I+1) - 2m^2 - 1\right]m$$

$$(1.28)$$

where C(22l, 1 - 1) and C(22l, 2 - 2) are the Clebsh-Gordon coefficients.

The ratios between the $\pm 3/2 \longrightarrow \pm 1/2$ and the central transition frequencies for l = 0, 2, 4 are given in Ref. [19]. As we have seen in the case of MQMAS that under MAS the second rank l = 2 terms get averaged out but the fourth rank terms are scaled by $P_4(\cos\theta_{MA})$ which result in causing line broadening to the central transition lines and the spinning sidebands from satellite transitions. Again similar to the MQMAS technique the line broadening can be completely removed by doing the experiment in 2D fashion. The l = 4 terms between the satellite and central transitions are different only by a scaling factor, R [19]. Thus the dephasing of time-domain signals is refocused at $t_2 = Rt_1$ and the refocusing leads to an averaging of the remaining l = 4 terms for isotropic spectra.

1.4 Sensitivity Enhancement of NMR Signal

The most pressing problem faced by any solid state NMR spectroscopist is the low sensititvity of the NMR signal. Hence it is of paramount importance to design methods to manipulate spins within a system in such a way to obtain higher sensitivity. This is more important in case of quadrupolar systems which more often then not have very poor intrinsic sensitivity owing to their large quadrupolar moments. Low natural abundance and low gyromagnetic ratio often add to the problem.

For dilute-spin nuclei, S, in solids, cross-polarization (CP) [6,7] with abundant spins, I, has become a standard technique for improving the quality of NMR spectra for the S spins. In this case, the CP experiment involves a transfer of magnetization from the abundant spins to the dilute spins. To be successful, this experiment requires that the I and S spins are spin-spin coupled to one another. As well, conventional Hartmann-Hahn

CP is technically demanding, particularly when the dilute spins have gyromagnetic ratios that are an order of magnitude or more smaller than the abundant spins. If the dilute spin is a half-integer quadrupolar nucleus, the lineshape of the central transition also depends on the contact time used in the CP experiment [22, 23].

A different class of experiments that are designed to improve the signal-to-noise (S/N) of NMR spectra is based on modifying the Boltzmann thermal equilibrium populations, by so-called population transfer experiments [24, 25]. Probably, the most important of these is the insensitive nuclear enhancement by polarization transfer (INEPT) experiment [24, 26] and related experiments that enhance the intensity of the S spins in isotropic liquids and solids by a factor of up to γ_I/γ_S.

In this section we primarily focus on population transfer techniques that have been used recently to enhance the central NMR transition, 1/2 to -1/2, of half integer spin quadrupolar nuclei in solids. Enhancement of the signal can be achieved by manipulating the equilibrium population of different energy levels. According to Boltzmann law the equilibrium population, at high temperature limit, of a spin state m_I of a nucleus I can be expressed as:

$$p_{m_I} \approx 1 + 2m_I \left(\frac{h\nu_0}{2kT} \right), \qquad (1.29)$$

where h is Planck's constant, k is the Boltzmann constant, T is the absolute temperature, and m_I = -I, -I + 1,...., I. This may be rewritten as

$$p_{m_I} \approx 1 + 2m_I\delta. \qquad (1.30)$$

The manipulation of nuclear spin population by selective excitation was first introduced by Pound in 1950 [27]. He described the effect of partially saturating one of the ^{23}Na signal in $NaNO_3$ on other transitions. Later Vega and Naor [28] selectively inverted the populations of the ^{23}Na satellite NMR energy levels in a single crystal of $NaNO_3$ using amplitude-modulated pulses.

	(a)	**(b)**	**(c)**	**(d)**
m=-5/2	1-5δ	1-3δ	1-5δ	1-δ
m=-3/2	1-3δ	1-3δ	1-δ	1-5δ
m=-1/2	1-δ	1-3δ	1-5δ	1-3δ
m=1/2	1+δ ⌉1	1+3δ ⌉3	1+5δ ⌉5	1+3δ ⌉3
m=3/2	1+3δ	1+3δ	1+δ	1+5δ
m=5/2	1+5δ	1+3δ	1+3δ	1+δ

Figure 1.9: Population distribution of different energy levels of a spin-5/2 system (a)at equilibrium and (b), (c), (d) under different population altering methods.

There are two methods for altering the population of energy levels. One is to saturate or to invert the population of two or more energy levels. A schematic representation of energy levels of a spin-5/2 system with thermal equilibrium population is shown in Fig. 1.9(a). Simultaneous saturation of the satellite transitions equalizes the populations of all the lower and upper energy levels and, as represented in Fig. 1.9(b), enhances the signal intensity of the central transition by a factor of $(I + 1/2)$; i.e., 3.0. Differential signal enhancements of the central transition may result depending on which populations are inverted and the order in which they are inverted. To achieve the maximum signal enhancement, 2I, for the central transition of a spin-5/2 nucleus, the populations associated with the ±5/2 and ±3/2 transitions must be inverted first, followed by those associated with the ±3/2 and the ±1/2 transitions, as shown in Fig. 1.9(c). Inversion of the ±3/2 populations with the ±1/2 populations first, followed by an inversion of the ±5/2 and ±3/2 populations will only result in an enhancement of 3.0, as indicated in Fig. 1.9(d).

There are many methods for achieving either saturation or inversion of energy levels thereby increasing the sensitivity of the NMR signal. These include Fast Amplitude Modulated pulses (FAM) [30–32], Double Frequency Sweep (DFS) [33–36], Gaussian pulses [37], Hyperbolic Secant pulses (HS) [38–41].

1.4.1 Fast Amplitude Modulation

In 1999, Madhu *et al.* [29] developed a method of using a phase alternating pulse trains to enhance the transfer of multiple quantum coherence to single quantum coherence in a MQMAS experiment. They denoted this method as Fast Amplitude Modulation. Later in 2000, Yao *et al.* [30] used the same method to enhance the signal of central transition of ^{23}Na and ^{87}Rb in MAS condition and they obtained an enhancement of 1.7 and 1.9, respectively. This method is also known as Rotor Assisted Population Transfer (RAPT) since spinning powder samples at magic angle has the effect of sweeping the satellite transition frequencies to the resonant condition. As shown in Fig. 1.10(b) FAM pulses can roughly be considered as cosine modulation with ω_m as the modulation frequency. Modulation of this kind is well known to results in side bands at $\pm\omega_m$ again symmetrically around the carrier frequency. In 2003, Madhu *et al.* [31] explored the idea of using two different FAM blocks with two different modulation frequencies for spin-5/2 systems. A first block with higher modulation frequency and later a second block with lower modulation frequency. The idea was to first saturate the outer satellites with FAM of higher modulation frequency then saturate the inner satellites with FAM block of lower modulation frequency. With this method they reported enhancements of 2.5 and 2.3 for the ^{27}Al and ^{17}O central transition, respectively. We will discuss about another variant of FAM known as *multiple* FAM or m - FAM in next chapter.

(a) **(b)**
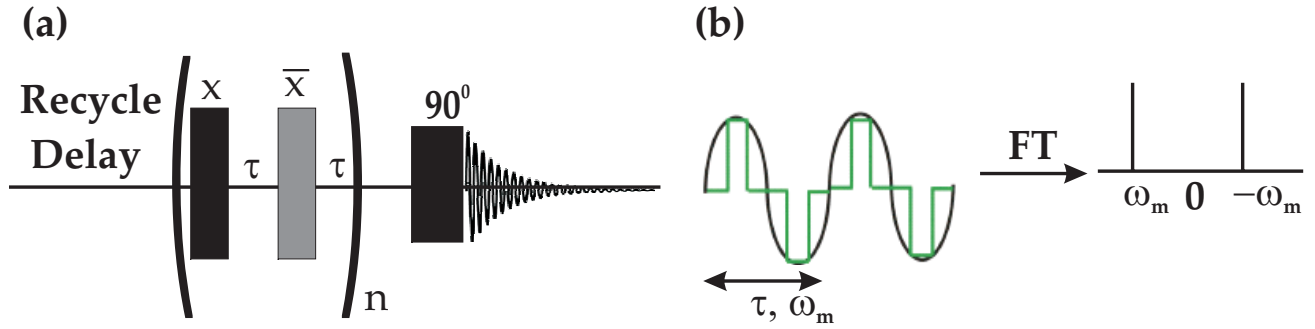
Figure 1.10: (a) Schematic representation of FAM pulse sequence with a single FAM block for spin-3/2 system, (b) Cosine modulation of the FAM sequence.

1.4.2 Double Frequency Sweep

It was Kentgens [42] who first applied frequency sweep in modern FT-NMR spectrometers to observe spectra of half-integer quadrupolar nuclei in the solid state. Later Haase *et al.* [43–45] used an adiabatic frequency sweep to alter the thermal equilibrium populations and enhance the central transition of ^{27}Al (I = 5/2) in a single crystal of sapphire. In 1999 Kentgens applied a time dependent amplitude modulated pulse scheme of the type depicted in Fig. 1.11 to invert the population of the satellites simultaneously and named the method as Double Frequency Sweep (DFS). If the rf field strength be ω_1 of the DFS pulses then ω_1 will be amplitude modulated within DFS as

$$\omega_1 = \omega_{1,max} \cos \int \left(\omega_s + \frac{\omega_f - \omega_s}{\tau} t \right) dt \qquad (1.31)$$

where $0 \leqslant t \leqslant \tau$ and $\omega_{1,max}$ is the amplitude of the modulation. This kind of modulation results in rf irradiation not at carrier frequency ω but simultaneously at ω - ω_m and ω + ω_m symmetrically around the carrier frequency, where $\omega_m = \left(\omega_s + \frac{\omega_f - \omega_s}{\tau} t \right)$. Depending on whether ω_s is smaller or bigger than ω_f a divergent or convergent DFS

is resulted, respectively. Applying DFS on ^{23}Na of NaNO$_3$ single crystal they obtained an enhancement of 3 while for powdered NaNO$_2$ they observed an enhancement of 2.3 and 1.7 in static and MAS condition. Under MAS condition DFS causes enhancement similar to that expected for saturation of outer satellites i.e., between 1.7 and 2.0 for spin-3/2 nuclei, indicating a mixture of inversion and saturation of the populations.
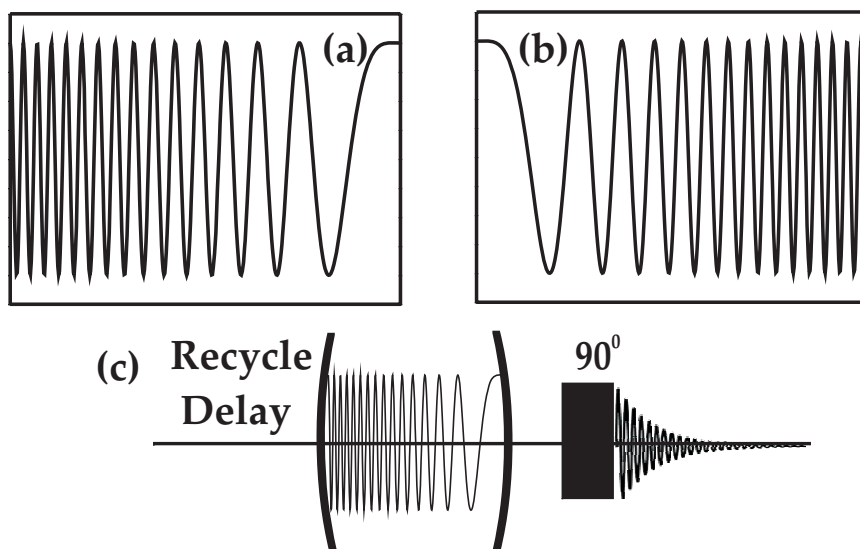
Figure 1.11: (a) Amplitude profile of converging, (b) diverging DFS scheme, (c) Schematic diagram of the DFS pulse scheme.

1.4.3 Gaussian Pulse

Grandinetti *et al.* in 2000 introduced another new variant of RAPT pulse scheme by using a train of Gaussian pulses with alternating off-resonance frequencies of $\pm \nu_{off}$ instead of the rectangular pulses. This modification helps to do away with the need for rapid change of phases within the RAPT sequence and also permits larger frequency offsets. However, this modification performs only slightly better than FAM sequence in terms of signal enhancement.
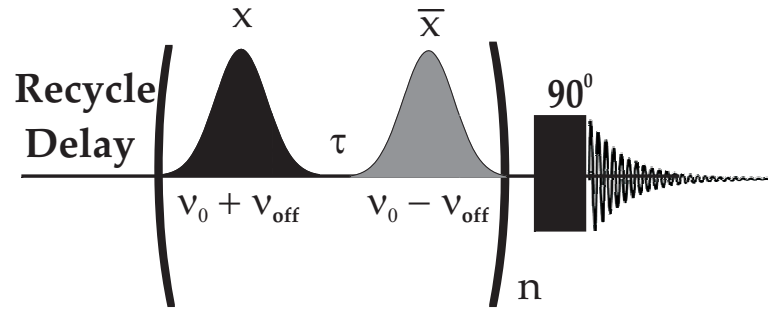
Figure 1.12: Schematic representation of Gaussian pulse sequence.

1.4.4 Hyperbolic Secant Pulse

Another method for altering the population distributions of energy levels is to use broad band inversion pulses such as hyperbolic secant pulses. Although the use of hyperbolic secant pulses is one of the latest additions in the realm of signal enhancements of quadrupolar nuclei in solid state NMR, this method has its origin in laser spectroscopy where it was first used by McCall and Hahn [46] in 1969. Later it was used in MRI by Silver *et al.* [47] to provide highly selective, low-power π-pulses. The interesting thing about hyperbolic secant pulses is that its inversion profile is independent of applied rf field once it is above a certain level [35]. Unlike DFS where phase is kept constant here the HS pulses are generated by applying modulation on both amplitude, ω_1 and phase, ϕ_1,

$$\omega_1 = \omega_{1,max} sech\left(\beta\left(\frac{2t}{T_p} - 1\right)\right) \tag{1.32}$$

$$\phi_1 = \frac{\lambda}{\beta}\frac{T_p}{2}\ln\left[\cosh\left(\beta\left(\frac{2t}{T_p} - 1\right)\right)\right] + \Delta\omega_0 t \tag{1.33}$$

where $\omega_{1,max}$ is the maximum amplitude of the pulse, T_p is the pulse width, β (=5.3) is a truncation factor which limits the sech function to 1% of its amplitude, λ is one half of the band width and $\Delta\omega_0$ is the offset of the HS pulse from the carrier frequency. The phase variation results in a frequency sweep, $\Delta\omega$ (t), over the band width centred at carrier frequency $\Delta\omega_0$,

$$\Delta\omega(t) = \lambda \tanh\left(\beta\left(\frac{2t}{T_p} - 1\right)\right) + \Delta\omega_0. \tag{1.34}$$

In contrast to DFS, HS pulses have a nonlinear frequency sweep over the pulse duration. The inversion profile for an HS pulse using a 29 kHz effective rf field, and a pulse width of 500 μs shows an inversion bandwidth, BW, of 100 kHz which is much larger than a rectangular π pulse [48]. Using this sequence Wasylishen *et al.* have reported an enhancement of upto 4.1 in the central transition of powder ^{27}Al under MAS in Al(acac)$_3$ sample [40].
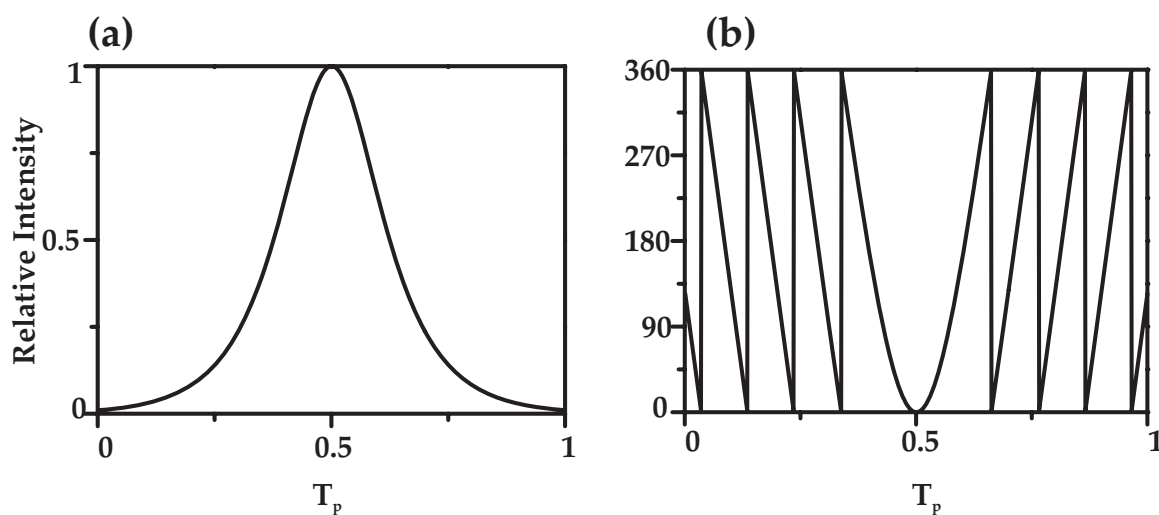
Figure 1.13: (a) Amplitude modulation and (b) Phase modulation of hyperbolic secant pulse with respect to pulse width T_p in ms.

1.4.5 Carr-Purcell-Meiboom-Gill Sequence

For quadrupolar systems with large nuclear quadrupolar coupling constant, χ_Q, static quadrupolar-echo (QE) [49, 50] experiment has been the method of choice for detecting the rapidly decaying free induction decay (FID) without disturbance from finite receiver dead time and probe ringing. But for half integer spin quadrupolar nuclei having large χ_Q even QE or QE-MAS experiments suffer from low sensitivity and resolution, since the second-order quadrupolar powder pattern of the central transition can be several kHz wide. To remedy these problems, while maintaining structural or dynamic information from the anisotropic interactions, and achieving gain in the signal to noise (S/N) ratio can be done by implementing Carr-Purcell-Meiboom-Gill [51, 52] series of selective π pulses.

The CPMG technique is an extension of the Carr-Purcell method [51], which, in turn, had been introduced to circumvent the effect of molecular diffusion and pulse imperfections on the measurements of transverse relaxation time T_2 via Hahn's spin echo. Although initially used for refocusing the inhomogeneous line broadening, the CPMG sequence can also lessen the homonuclear dipolar broadening in solids. The CPMG scheme has been adapted to various solid-state NMR experiments involving the quadrupolar nuclei.

The quadrupolar CPMG [53] method (also known as QCPMG) pulse sequence for the sensitivity enhancement of quadrupolar echo NMR (QE NMR) is shown in Fig. 1.14. The pulse sequence has basically three parts, part A is a standard QE sequence with τ_2 optimized such that the acquisition starts at the echo maximum. The repeating unit in part B accomplishes sampling of the spin-echoes generated by the interrupting train of π_y refocusing pulses. The receiver-off periods τ_3 and τ_4 bracketing the refocusing pulses serve to protect the receiver from the effects of the π_y pulses. Finally, part C extends the decaying part of the final spin-echo to the free induction decay (FID) to avoid undesired baseline problems and sinc wiggles upon Fourier transformation. It is noted that the
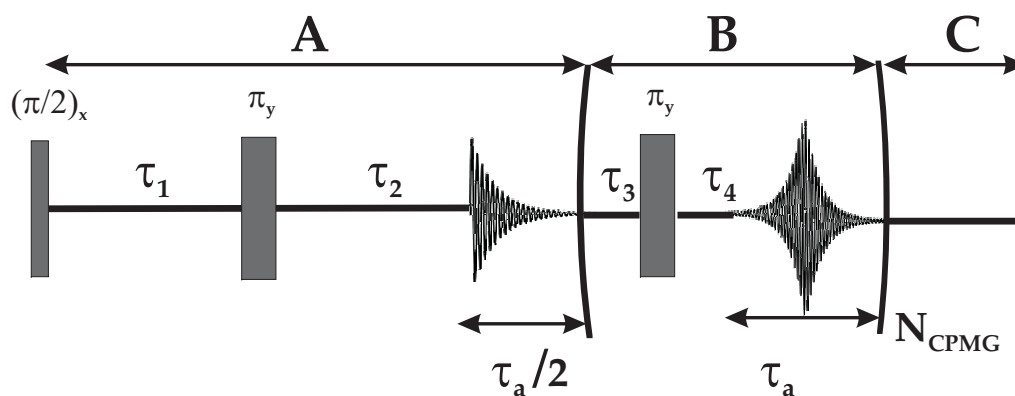
Figure 1.14: Schematic representation of CPMG pulse sequence.

flip angles of all pulses correspond to the angles effective for selective operation on the (-1/2, 1/2) central transition.

Unlike other enhancement schemes discussed thus far QCPMG does not alter the population of energy levels. This sequence achieves signal gain by refocusing the inhomogeneous interactions and splitting the QE spectrum, which would result from sampling of the decaying part of the first echo alone (i.e., part A of the pulse sequence), into a manifold of sidebands separated by $1/\tau_a$. This partition of the powder spectrum into distinct sidebands leads to a considerable increase in the overall sensitivity of the experiment. In this and other respects the spin-echoes observed in QCPMG experiments resemble the rotational echoes observed in magic-angle spinning (MAS) experiments.

CPMG sequence proved to be highly successful as a means to enhance the sensitivity of second-order broadened quadrupolar nuclei in static [53–55], MAS [56–58], and MQ-MAS [59–61] experiments.

CPMG method has also been applied extensively in spin-1/2 systems, specially in

case of ^{29}Si NMR for signal enhancement because its high efficiency in refocusing the inhomogeneous interactions. We shall discuss more about this aspects of CPMG in the fifth chapter of the thesis.

1.5   Recoupling Techniques in NMR

It is known that MAS averages out all the interactions of 2nd rank tensor in nature. This means that interactions such as heteronuclear dipolar coupling, homonuclear dipolar coupling, and chemical shift anisotropy gets averaged out resulting in a narrow NMR lines. Though sharp NMR lines is a desirable feature, however in doing so one loses all the interesting spatial (anisotropic) informations. Hence it is of utmost importance to design techniques which will bring back one of the interactions averaged out by MAS while filtering out the others. People have come up with several clever ideas by which one can successfully bring out one of the interactions while not jeopardising the high resolution nature of the spectrum.

One of the first successful attempt in this direction was carried out by Waugh and co-workers when they applied a series repetitive pulses synchronous with the rotor period and showed that chemical shift anisotropy (CSA) can be brought back [62]. It was later that people found out that by applying continuous rf field to one spin species may restore the effect of the heteronuclear dipolar interaction to a second spin species [63], which is now known as heteronuclear dipolar recoupling. To achieve this one needs to maintain rf amplitude such that it is an integer multiple of the rotor period. This condition is known as "rotary resonance". Later Schaefer *et al.* pointed out that by applying two strong 180^0 pulses at every rotor period one can achieve the same result [64]. This idea later materialized to the designing of highly successful heteronuclear recoupling sequence, rotational echo double resonance (REDOR) method [65]. Tycko in 1990 came up with a sequence known as dipolar recoupling at the magic angle (DRAMA) scheme [66] which recouples the homonuclear dipolar coupling. After this various al-

ternate methods came up for efficient homonuclear dipolar recoupling such as, radio-frequency driven recoupling (RFDR) scheme [67], double-quantum homonuclear rotary resonance (2Q-HORROR) method [68] etc. The HORROR method showed for the first time that it is possible to achieve highly efficient 2Q excitation in a powder sample. However HORROR is only possible with coupled spins which have chemical shift difference. The effort of making this scheme more general ultimately led to the designing of C7 sequence [69] and this in turn led to the introduction of "symmetry principles" in designing recoupling sequences by Levitt [70].

The sequences designed based on the symmetry principle take the advantage of the rotational properties of the spin interactions. In general each spin interaction can be expressed as the product of its "spatial" part which expresses the transformation of the spin interaction with respect to the physical rotation of the molecular frame and the "spin" part which expresses the way spin interaction changes with the rotations of the nuclear spin polarization. These rotational properties can be summarized in terms of the rotational ranks listed in table 1.1.

Table 1.1: Components of nuclear spin interactions in the interaction frame of an applied rf field, in the case of exact magic-angle spinning.

Spin interactions	Space rank	Space components	Spin rank	Spin components
Isotropic chemical shift	0	0	1	-1, 0, 1
Chemical shift anisotropy	2	-2, -1, 1, 2	1	-1, 0, 1
J coupling	0	0	0	0
Homonuclear dipolar coupling	2	-2, -1, 1, 2	2	-2, -1, 1, 2
Heteronuclear dipolar coupling	2	-2, -1, 1, 2	1	-1, 0, 1

The interactions which are invariant to particular type of rotations are assigned as rank 0. Interactions which have the rotational symmetry of a p-orbital in atomic theory are assigned rank 1. Interactions which have the rotational symmetry of a d-orbital in

atomic theory are assigned rank 2. If a spin interaction has spatial rank l and spin rank λ then the physical rotation of the molecular frame induces a mixing of $(2l + 1)$ space components with m = -l, -l+1, ..., l. Similarly the rotation of nuclear spin polarization induced by rf pulses causes a mixing of $(2\lambda + 1)$ spin components with μ = - λ, -λ + 1, ..., λ. Hence in presence of both sample rotation and resonant rf fields any spin interaction can be regarded as a superposition of $(2l + 1) \times (2\lambda + 1)$ terms.

$$\mathscr{H}^\Lambda = \sum_{m=-l}^{+l} \sum_{\mu=-\lambda}^{+\lambda} \mathscr{H}_{lm\lambda\mu}^\Lambda \tag{1.35}$$

Explicit expressions for the components $\mathscr{H}_{lm\lambda\mu}$ may be found in Ref. [71].

Selective recoupling of a specific interaction is possible by designing pulse sequences based on the transformation property of that interaction.

1.5.1 Definition of Symmetry Based Sequences

There are two classes of symmetry based recoupling sequences, namely, CN_n^ν and RN_n^ν [70]. Both CN_n^ν and RN_n^ν sequences are characterized by three symmetry numbers, N, n, and ν. N is known as the "step number" while n and ν is known as "space winding" number. By suitably choosing the three symmetry numbers N, n and ν it is possible to make the pulse sequence to be selective to a specific interaction.

1.5.2 CN_n^ν

A CN_n^ν sequence may be constructed by dividing n rotational period into N equal interval during which a cyclic rf sequence is applied which implies that the rf sequence induces a rotation of nuclear spin polarization through an integer multiple of 360°. The winding number ν defines the phase difference between the successive cyclic rf elements and is given by $2\pi\nu/N$. The sample then undergoes physical rotation (MAS) through n full rotations at the same time experiences a set of cyclic rf elements, the phases of which

advances through v full rotations. A schematic diagram of the sequence with timings is shown in Fig. 1.15.

To determine whether a spin interaction is symmetry allowed or not to first order is determined by the following selection rule,

$$\mathscr{H}^{(1)}_{lm\lambda\mu}(t_q) = 0$$

when

$$mn - \mu v \neq NZ \tag{1.36}$$

where Z is any integer [69]. The superscript (1) denotes that the selection rule is valid only to the first order average Hamiltonian theory [70].

One can take the symmetry sequence $C7^1_2$ as an illustrative example where $N = 7$, $n = 2$, and $v = 1$. Now let us consider the double quantum dipole-dipole term with { l, m, λ, μ} = { 2, 1, 2, 2 }. The expression $mn - \mu v$ yields a value 0, which is an integer multiple of $N = 7$. Hence this term is symmetry allowed in the sequence $C7^1_2$. Next if we consider the CSA term { l, m, λ, μ} = { 2, 2, 1, 1 }, the expression $mn - \mu v$ yields a value 5, which is not an integer multiple of $N = 7$. Hence the CSA interaction is symmetry forbidden under $C7^1_2$.

It is possible to depict the selection rules by space spin selection diagram, as shown in Fig. 1.16. It is evident from the diagram that all the CSA terms are suppressed in case of $C7^1_2$ sequence where as two homonuclear dipolar terms are symmetry allowed. This sequence therefore recouples the DD coupling terms while it suppresses the CSA terms. Since only dipole-dipole terms with spin quantum number $\mu = \pm 2$ are allowed this sequence results in the generation of CSA compensated double quantum recoupling sequence [70].

We have successfully made use of Permutationally Offset Stabilized C7 (POST-C7) variant of $C7^1_2$ sequence together with CPMG method to characterize the zeolite ZSM-5.
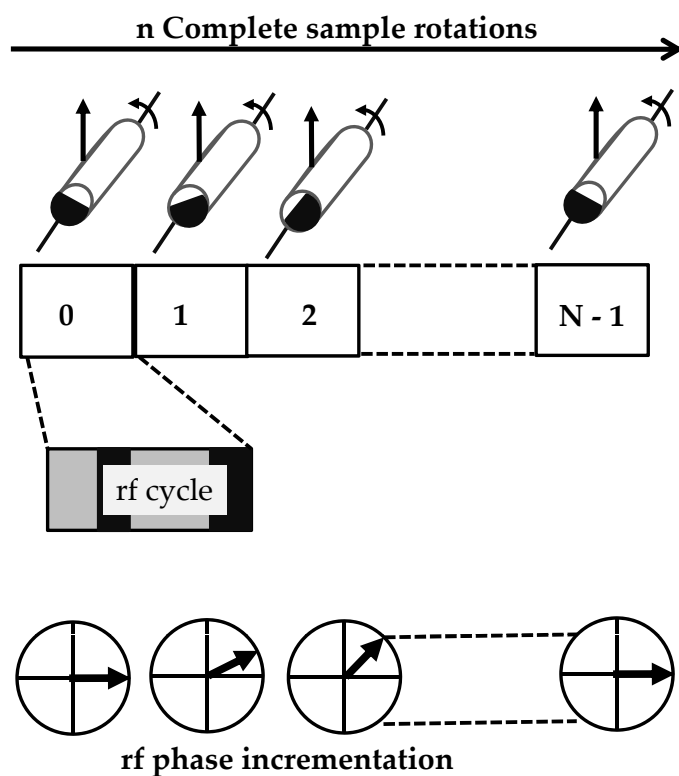
Figure 1.15: Construction of a CN_n^v sequence. The pulse sequence is set up in such a way that n sample rotations is synchronized with N rf elements. The pulses of consecutive elements increment in steps of $2\pi v/N$.
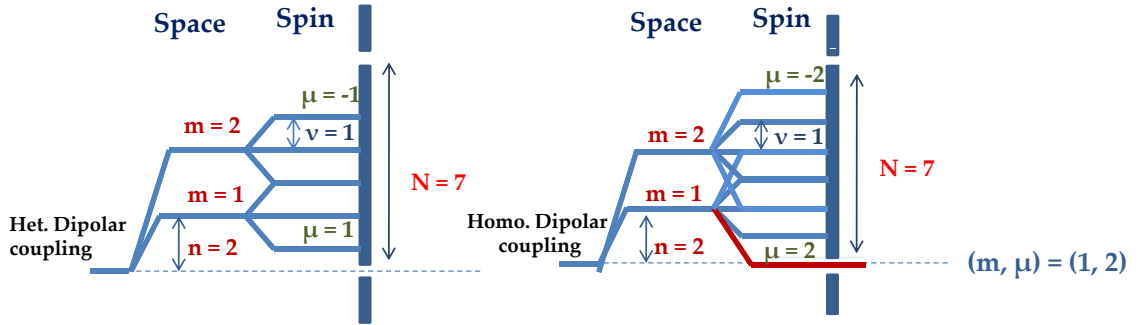
Figure 1.16: Space spin selection diagram for C7$_2^1$ symmetry sequence.

More about this will be discussed in the fifth chapter of this thesis.

1.5.3 RN$_n^\nu$

Unlike CN$_n^\nu$ sequences which has a cyclic basic element, the basic rf element of RN$_n^\nu$ sequence denoted as R consist of a pulse or pulses (composite pulses) that rotates the nuclear spin polarization through an angle of 180° around the x-axis [70]. The element R is repeated again but changing the signs of the phases of all the pulses within it. This element is denoted as $R^{'}$. Now the amplitude of the rf field is chosen such that the duration of R and $R^{'}$ denoted as τ_R is equal to $\tau_R = n\tau_r/N$ where $\tau_r = 2\pi/\omega_r$ is the rotor period and ω_r is the angular spinning frequency. Here N is an even integer and n is any integer. The RN$_n^\nu$ sequence can now by developed using $N/2$ concatenating phase shifted $\{RR^{'}\}$ pairs as follows,

$$RN_n^\nu = (R)_\phi (R^{'})_{-\phi} (R)_\phi (R^{'})_{-\phi} .....(R^{'})_{-\phi} \equiv \{R_\phi R^{'}_{-\phi}\}^{N/2}$$

where the phase shifts are specified by, $\phi = \pi v/N$, and v is an integer.

A schematic construction of the sequence is shown in Fig. 1.17.
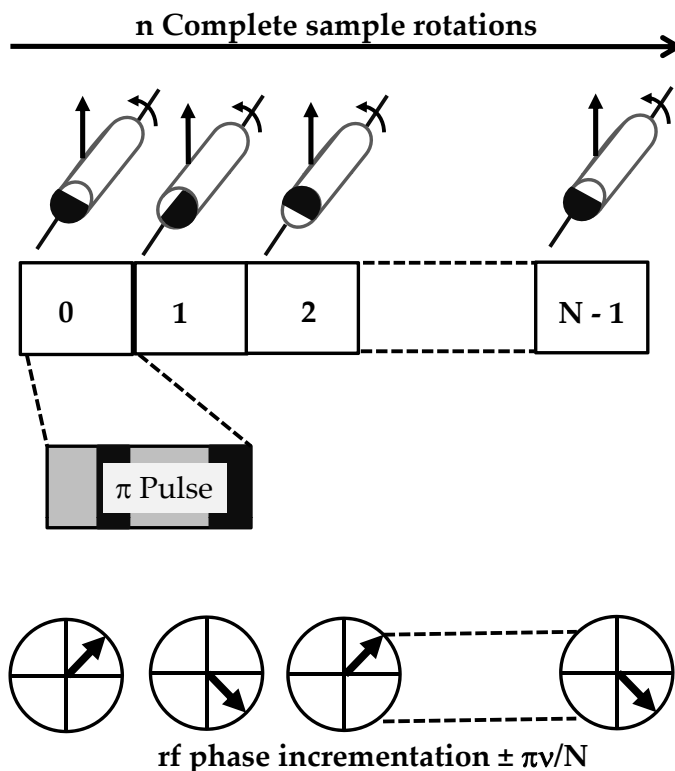
Figure 1.17: Construction of a RN_n^v sequence. The pulse sequence is set up in such a way that n sample rotations is synchronized with N rf elements. The phases of consecutive elements increment in steps of $\pm \pi v/N$.

The entire RN_n^v sequence is consists of $N/2$ contiguous pairs of RR' elements spanning n rotational periods.

The selection rule for RN_n^v sequence can be described as,

$$\mathcal{H}_{lm\lambda\mu}^{(1)}(t_q) = 0$$

when

$$mn - \mu v \neq \frac{N}{2} Z_\lambda \tag{1.37}$$

where Z_λ denotes any integer with the same parity as that of λ. This implies that if λ is odd then Z_λ is any odd integer and if λ is even then Z_λ is any even integer [71]. It is quite evident from above that RN_n^ν sequences are more restrictive than CN_n^ν sequences [70].

As an illustrative example let us consider $R18_2^5$ sequence. Now consider the heteronuclear dipolar coupling interaction with $\{l, \lambda\} = \{2, 1\}$. Since for this interaction $l = 2$ there are four m components with $m = \{-2, -1, 1, 2\}$ and since $\lambda = 1$ there are three components of $\mu = \{-1, 0, 1\}$. For the combinations of $\{l, m, \lambda, \mu\} = \{2, 2, 1, -1\}$ and $\{2, -2, 1, 1\}$ the selection rule $mn - \mu\nu$ yields 9 and -9, both of which are odd integers of $\frac{N}{2} = 9$ and spin rank λ is also odd. Hence these terms are symmetry allowed. If we now consider homonuclear dipolar coupling interaction with $\{l, \lambda\} = \{2, 2\}$ it can be easily found out that no combinations of $\{l, m, \lambda, \mu\}$ yields an even integer multiple of $\frac{N}{2} = 9$. This means that homonuclear dipolar coupling interaction is symmetry forbiddeen under the application of $R18_2^5$ sequence. The results are also diagrammatically shown in Fig. 1.18.
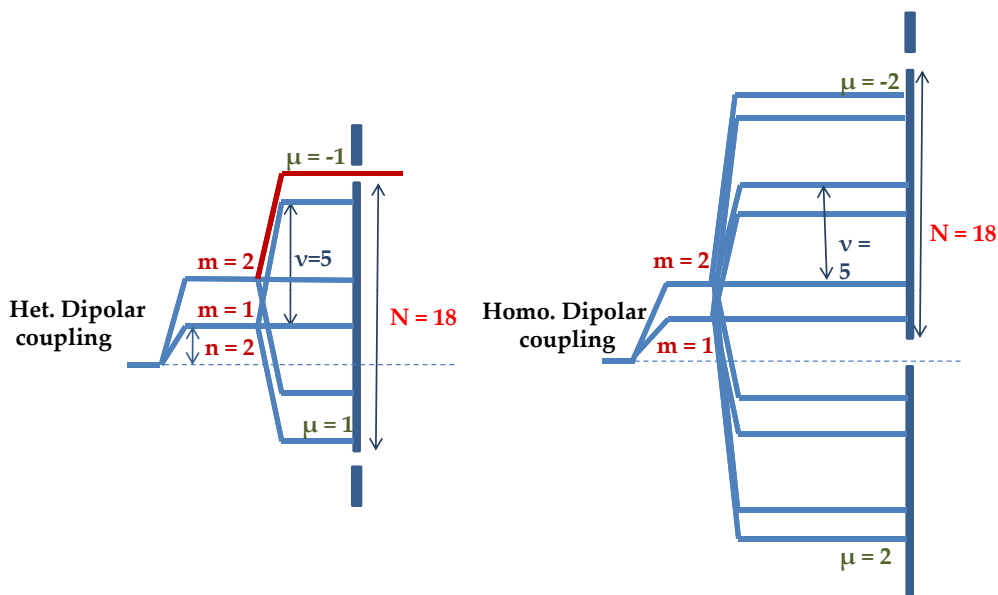
Figure 1.18: Space spin selection diagram for $R18_2^5$ symmetry sequence.

We have made use of R18$_2^5$ symmetry sequence to recouple heteronuclear dipolar coupling between a spin-1/2 system (^{1}H) and a quadrupolar system with spin-5/2 (^{17}O). We shall discuss more about this on the fourth chapter of this thesis.

1.6 Conclusions

A brief introduction of NMR was presented with an emphasis on the spectroscopy of the rigid solids. Various spin interactions were revisited with special emphasis on the quadrupolar interaction. Various high resolution NMR techniques for quadrupolar nuclei was discussed next. Then various sensitivity enhancement schemes for quadrupolar nuclei was outlined.

In the later half of this Chapter, recoupling techniques to selectively bring back specific nuclear spin interactions were discussed. The particular emphasis was on the irradiation schemes based on the symmetry properties of the internal spin interactions (CN$_n^v$ and RN$_n^v$).

1.7 Description of This Thesis

As the title of the thesis suggests, the work presented here represents the successful combination of two realms of solid-state NMR spectroscopy, which are the development of methodologies and application of them in the substances of material importance. This thesis also presents the use of these two realms of solid-state NMR in both spin-1/2 and half integer spin quadrupolar nuclei (I = 3/2, 5/2).

The second chapter deals with the designing of an improved sensitivity enhancement scheme (*m*-FAM, *multiple*-FAM)for quadrupolar nuclei where FAM pulse pairs and signal acquisition repeated multiple times before the spin system returns to thermal equilibrium. It will be shown to perform much better than original FAM sequence both under MAS and static condition on both spin-$\frac{3}{2}$ and spin-$\frac{5}{2}$ systems. It will be further shown

that the *m*-FAM scheme is much more robust with respect to experimental parameters facilitating an easy implementation. Additionally, the multiple version of SW($1/\tau$)-FAM will be shown to give better enhancement than SW($1/\tau$)-FAM. This chapter also consists of investigations carried out about the reason behind the better performance of multiple versions of enhancement schemes by doing numerical simulations on the differentially oriented single crystals under different enhancement schemes.

The third chapter contains experimental demonstration of the application of high resolution NMR techniques for the characterization and distinguish between all the different polymorphs of Alq_3 which is one of the most well known organic light emitting devices (OLED). This chapter also demonstrates that by using Isodensity Polarisable Continuum Model (IPCM) for Density Functional Theory (DFT) based quantum chemical calculation one can more accurately predict the quadrupolar parameters for these kinds of systems.

The fourth chapter discusses the results obtained when the symmetry sequence was combined with high-resolution sequences for the quadrupolar nuclei in 2D fashion to obtain the quadrupolar-dipolar (QD) correlation spectra. Further the possibility of performing three dimensional experiment by combining the high resolution techniques for quarupolar nuclei and symmetry sequence to simultaneously obtain the dipolar and quadrupolar informations will be explored. It also contains the results of 2D numerical simulations done to ascertain the relative orientations of dipolar and quadrupolar tensors.

The fifth chapter highlights the experimental method developed to enhance the sensitivity of dipolar recoupled ^{29}Si double-quantum magic-angle spinning experiment. Further, the applicability of the method will be demonstrated by using it to characterize catalytically important zeolite ZSM-5.

Chapter 2

Sensitivity Enhancement of the Central-Transition Signal of Half-Integer Spin Quadrupolar Nuclei

2.1   Introduction

The potential application of solid-state NMR in the study of quadrupolar nuclei in materials of inorganic, catalytic, and biological importance is well documented [23, 72]. However, due to one or many of the following factors such as, low natural abundance, small values of gyromagnetic ratios, and large values of quadrupolar interaction constants, the observable central-transition (CT) single-quantum (SQ) signal in one-dimensional (1D) experiments is often beset with sensitivity problems even under magic-angle spinning (MAS). These become more acute when spectra need to be acquired under static conditions. Hence, sensitivity enhancement of solid-state NMR spectra of half-integer spin quadrupolar nuclei is of utmost importance.

The seminal work of Vega and Naor in 1981 showed that amplitude-modulated radio-frequency (RF) pulses lead to inversion of populations across the satellite tran-

sitions giving rise to an enhanced population difference across the central transition and thereby an enhanced signal intensity in the case of single crystals under static conditions [28]. It may be noted that a similar attempt was made much earlier by Pound where a saturation of populations across the satellite transitions was shown to effect an enhanced central-transition signal again for static single crystals [27]. Many different schemes have been introduced since 1990 for the CT signal enhancement in 1D experiments, notable among them being "dual Q-probe" and frequency-swept adiabatic passage schemes [43–45], double-frequency sweeps (DFS) [33–36], fast amplitude-modulated (FAM) pulses [30–32], Gaussian pulse trains [37], and hyperbolic secant pulses [38–41]. All these modulated RF pulse schemes rearrange the populations across the satellite transitions, through a combination of both inversion and saturation, leading to an enhancement of the single-quantum central-transition signal. It may be noted that the FAM pulses were originally introduced in the context of signal enhancement of multiple-quantum MAS (MQMAS) experiments [14, 29, 73, 74]. The same pulse scheme was later termed as rotor assisted population transfer (RAPT) pulses by the group of Grandinetti [30]. Although it is true that the FAM pulses are most effective under MAS, certain enhancement could be obtained in static cases as well [75]. Variants of FAM which generate a frequency sweep by modulating the pulse duration in either a linear or non-linear way, notated as SW(τ)-FAM and SW($1/\tau$)-FAM, were found to give good signal enhancement in the case of static samples [76, 77].

A significant addition to these enhancement schemes was made by Kwak *et al.* where in they introduced multiple rotor assisted population transfers with Gaussian pulse pairs [78]. The idea was not just to repeat the Gaussian pulse pairs several times before the signal acquisition and wait for thermal equilibrium to happen, as also implemented with other schemes, but to repeat the Gaussian pulse pairs and signal acquisition multiple times before the spin system returns to thermal equilibrium. This was found to be beneficial as always there is a considerable amount of spin polarisation left in the satellite

transitions that are not transferred to the central transitions. By repeating the whole sequence several times within the relaxation time it is ensured that a substantial fraction of the population in the satellite transitions is converted to central transition. This multiply repeated scheme was shown to give a signal enhancement by a factor of 2.0 or more compared to implementing it once. This was later shown in the case of DFS scheme as well [79].

In this chapter we report on similar enhancement obtained with the FAM pulse scheme and its variants performed multiply, notated as multiple FAM (m-FAM), under both MAS and static conditions. We further examine the robustness of these schemes with respect to the MAS frequency ν_r and the nutation frequency of both the "CT selective 90° pulse $\nu_{nut}^{90°}$" used to create the transverse magnetisation and the FAM and the m-FAM pulses ν_{nut}^{FAM}. m-FAM performs much better under both spinning and static conditions. We report also on the signal enhancement obtained by repeating the SW($1/\tau$)-FAM scheme for the static case which in turn surpasses the performance of m-FAM. Investigation behind the probable reason for the higher enhancements for multiple FAM schemes were also carried out by doing numerical simulations.

Higher signal enhancement and much smaller dependence to the MAS frequency under spinning and nutation frequency of the FAM pulses for both spinning and static conditions are some of the desirable features of m-FAM and m-SW($1/\tau$)-FAM.

2.2 Experimental

All experiments were carried out on a Bruker Avance-500 spectrometer operating at a field strength of 11.7 T with a Bruker 4 mm triple-resonance probe. Experiments were performed observing the spin-3/2 ^{23}Na resonance of Na_2SO_4 at a Larmor frequency of 132.25 MHz and the spin-5/2 ^{27}Al resonance of the gibbsite sample at a Larmor frequency of 130.28 MHz. The quadrupolar coupling constant χ of ^{23}Na in Na_2SO_4 is 2.6 MHz and asymmetry parameter η is 0.6 [80]. Gibbsite has Al in two different

environments with χ = 2.0 MHz and η= 0.8 and χ = 4.3 MHz and η= 0.4 [81].

We denote the FAM pulse train consisting of a pulse pair and windows of delays of equal duration separating them by a concise notation of the form $F_n^I(\tau)$, where n corresponds to the total number of pulse pairs in the FAM scheme and τ is the duration of one FAM block in μs [82]. The Roman numeral in the superscript suggests that FAM-I is used here. For ^{23}Na (spin I=3/2) the FAM train was of the form $F_{18}^I(2.8)$ and for ^{27}Al (I=5/2) we used FAM train of the form $F_{10}^I(6)F_{12}^I(7)$ to obtain maximum enhancement. Two FAM blocks were used for spin-5/2 nuclei with the first one affecting the outer satellite transition and the second one affecting the inner satellite transition. Figure 1a shows the pulse scheme employing FAM for signal enhancement in spin-3/2 systems.

The *m*-FAM scheme has FAM as the basic building block where the optimised FAM cycle along with the central-transition selective 90° pulse and the acquisition were repeated multiple times until maximum enhancement of the signal was obtained. The pulse scheme is given in Fig. 1b again for spin-3/2 systems. We denote the *m*-FAM scheme as $F_{n:m}^I(\tau)$ where m in the subscript indicates the number of times FAM and acquisition are repeated. For ^{23}Na (I=3/2) we used *m*-FAM of the type $F_{18:10}^I(2.8)$ and for ^{27}Al (I=5/2) we used *m*-FAM of the form $F_{10:12}^I(6)F_{20:12}^I(7)$. For rotor synchronised *m*-FAM experiments on ^{27}Al we made use of *m*-FAM of the form $F_{10:12}^I(6)F_{20:12}^I(6)$.

For the spin 3/2 system the nutation frequency of the FAM pulses was 53 kHz and that for the central-transition selective 90° pulse was 25 kHz. For the spin 5/2 system the nutation frequency of the FAM pulses was 62 kHz and that for the 90° pulse was 25 kHz. For both the nuclei recycle delay was 2 s.

2.3   Simulation

All the numerical simulations were carried out using SIMPSON simulation package. All the experimental parameters such as the number of pulses, timings, and field strength were included in the simulation. The shape for the Hyperbolic Secant pulse, Double

Frequency Sweep (DFS) pulse and Gaussian Pulse were created within the SIMPSON input file. Typically the powder averaged spectra were calculated using 4186 crystal orientations and 5 γ angles. The maximum time step over which the Hamiltonian was considered time independent was kept at 0.5 μs. The SIMPSON simulations for a powder of spin-5/2 system using HS pulses of 700 μs took approximately 2 h in a HP XW 4400 workstation. Similarly for the same system the simulation took 1.5 h to finish when DFS pulses of 400 μs and for Gaussian pulses it took around 1.25 h.

2.4   Results and Discussion

In this section we report the results obtained from numerical simulations using different enhancement schemes for spin-5/2 system both in powder and single crystal. We also discuss about the experimental results obtained from the spin-3/2 and spin-5/2 samples using FAM and m-FAM pulses under both MAS and static conditions. The signal enhancement factor η reported with the use of FAM schemes is with respect to the signal obtained with only a single 90$^\text{o}$ pulse.

2.4.1   Numerical Simulation

All the numerical simulations were carried out on a spin-5/2 system with the quadrupolar coupling constant χ of 3.0 MHz and asymmetry parameter $\eta = 0.2$. Simulations were done for both powder and single crystals. Initially different enhancement schemes (HS, DFS, Gaussian, FAM) were optimized on powder and the resulting enhancements are given in the Table 2.1. The simulated powder spectra are given in Fig 2.1.

After this the optimized enhancement schemes were applied on single crystals of the same spin-5/2 system with same quadrupolar parameters. The orientations which were considered for the simulations are given in Fig 2.2.
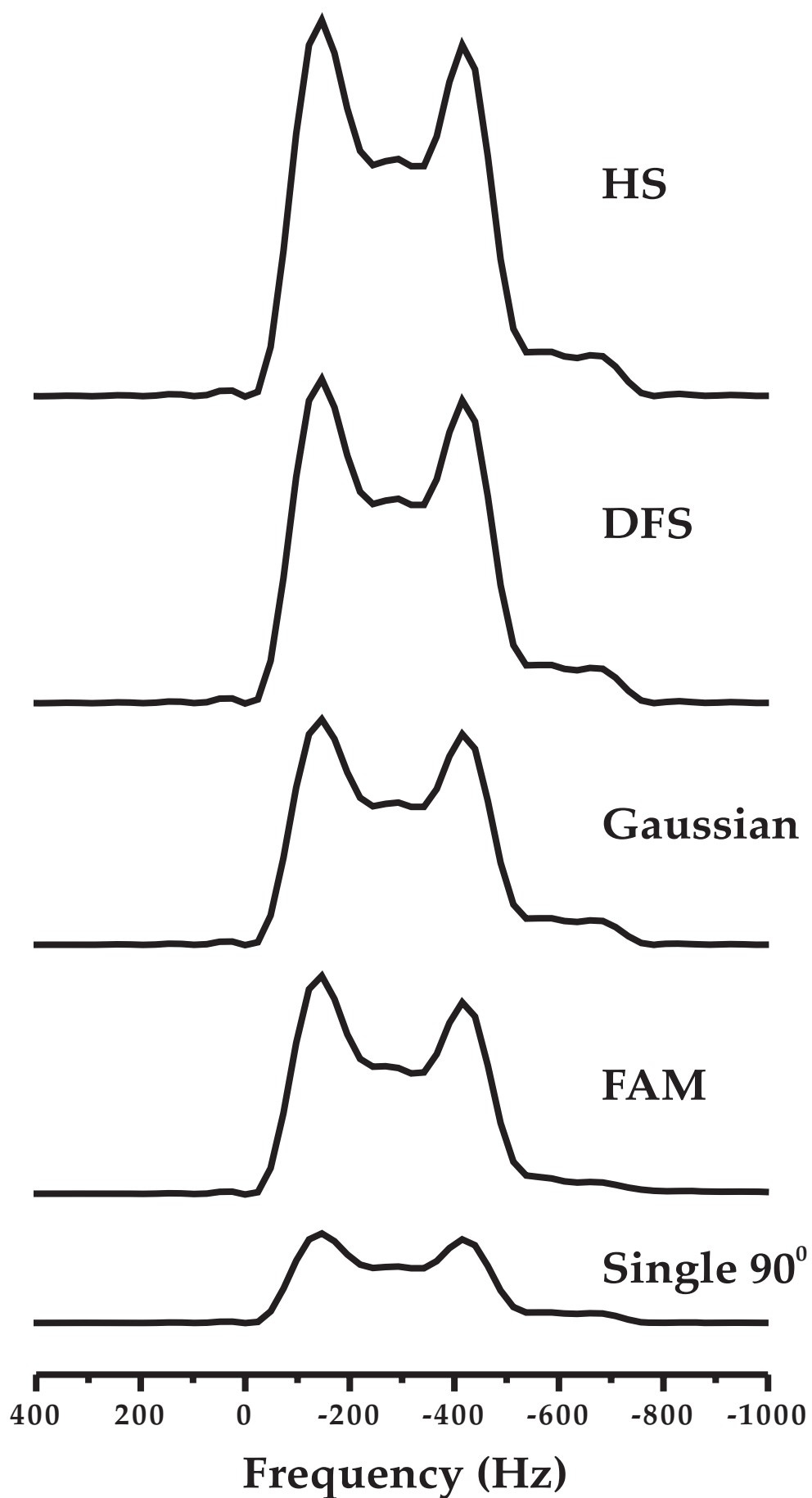
Figure 2.1: Powder simulation of a spin-5/2 system under different pulse schemes.
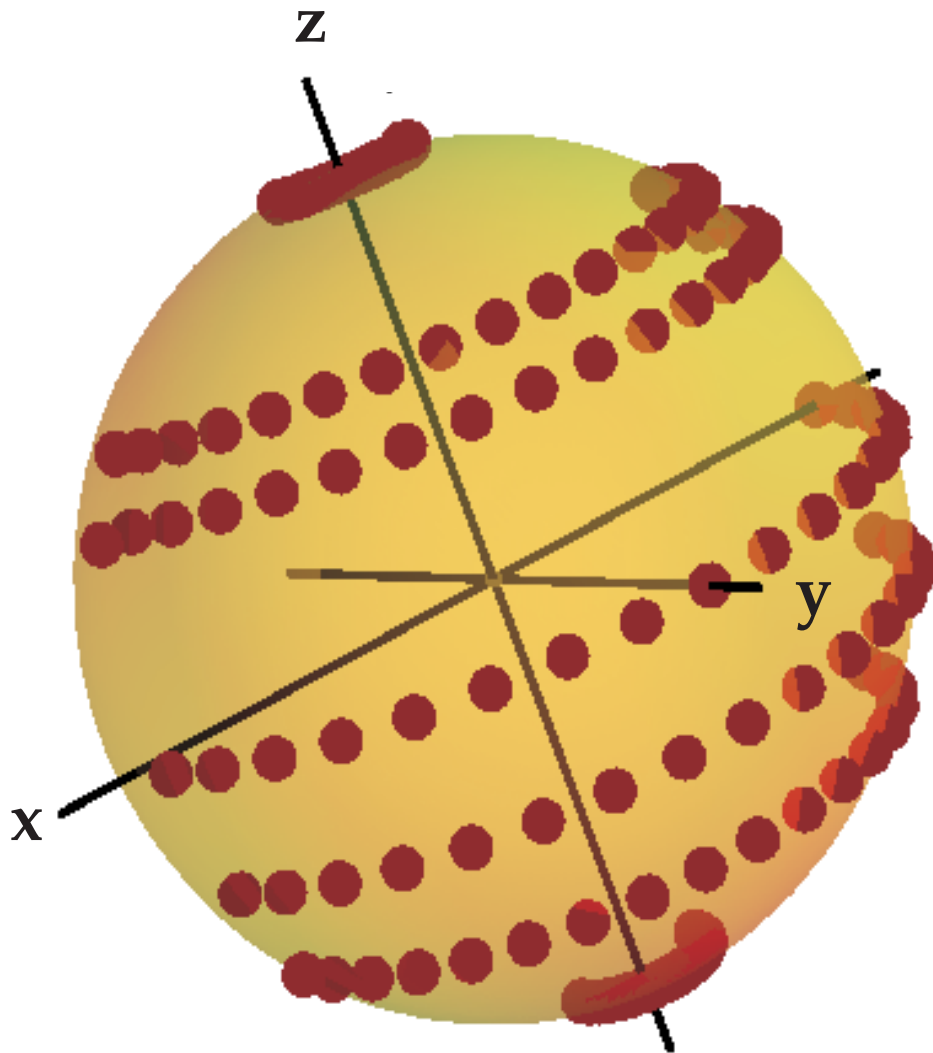
Figure 2.2: Powder orientations considered for the single crystal simulations.

Table 2.1: Enhancements achieved by numerically simulating different enhancement schemes.

Enhancement Schemes	Enhancements
Hyperbolic Secant	4.1
Double Frequency Sweep	3.7
Gaussian	2.7
Fast Amplitude Modulated	2.5

Fig 2.3 shows that for all the enhancement schemes the enhancements are not uniform for all the crystallites rather the enhancements are differential and the enhancements as a matter of fact vary from 1 to the maximum theoretically possible enhancements. Further it was seen (Fig 2.4) that when the spinning speed was varied for a particular enhancement scheme (FAM) the variation in the enhancements also changes from one spinning speed to another. In these plots different coloured regions denote different set of orientations. The black region denotes orientations where the euler angle β_{MR} is fixed at 10° and the euler angle α_{MR} is varied from 0° to 180°. Similarly for the red region β_{MR} is fixed at 50°, again for blue, wine, olive, purple and grey regions β_{MR} are fixed at 60°, 90°, 110°, 125° and 170° respectively. For each of these β_{MR} the α_{MR} is varied from 0° to 180°. The subscripts associated with the euler angles denote that these euler angles relate molecular frame to rotor frame.

It is well known that under MAS any enhancement scheme can only affect a certain region of the whole crystallite orientations of the powder. The observation that all the enhancement schemes affect different crystallite orientations differently under MAS led us to believe if a enhancement scheme can be designed which can affect large distribution of crystallite orientations within a powder then that scheme has better chance of achieving more enhancement. Hence we came up with a modification of the FAM scheme where the optimised FAM cycle along with the central-transition selective 90° pulse and the acquisition were repeated multiple times (*m*-FAM). This modification along with the
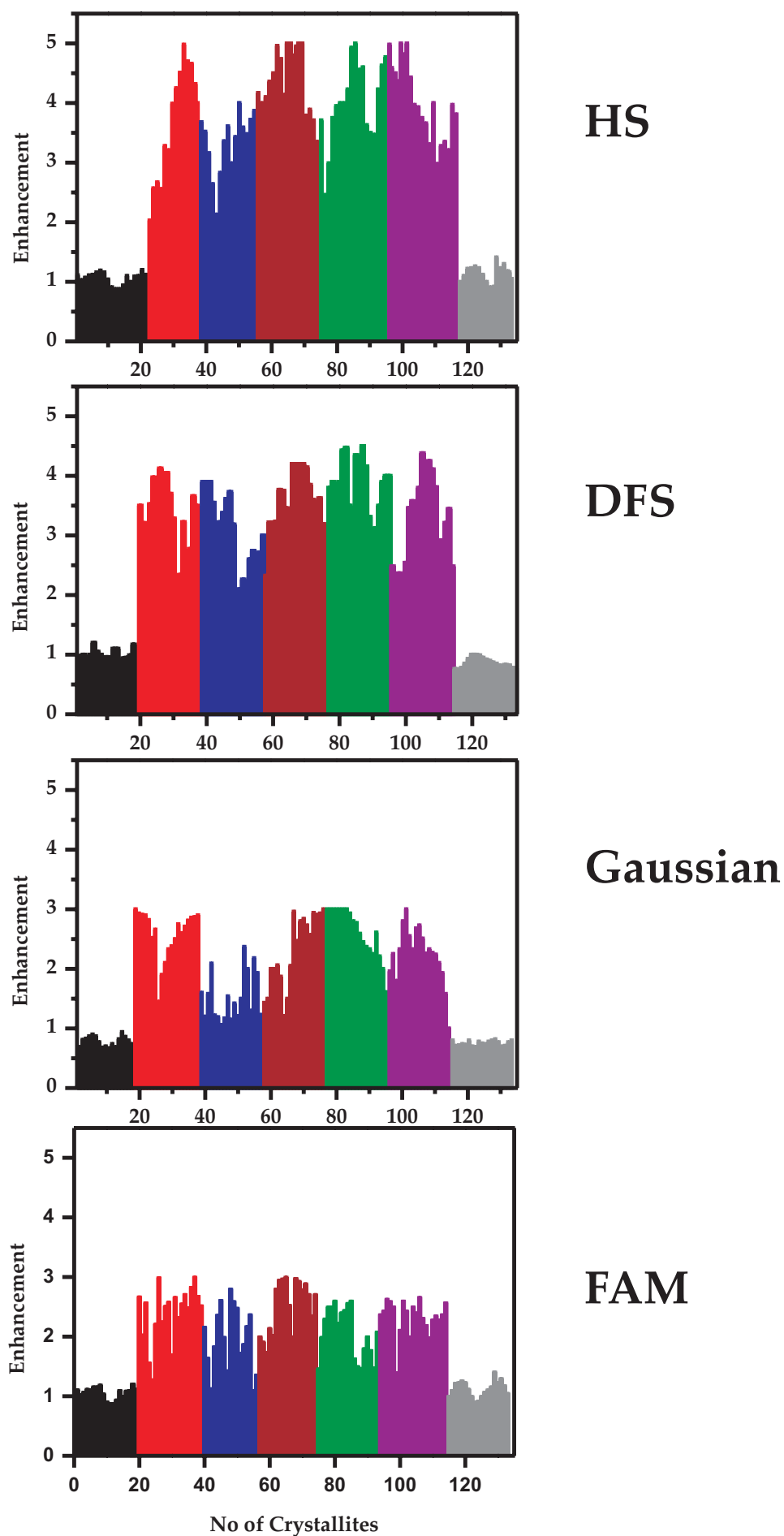
Figure 2.3: Enhancements of individual crystallites under different enhancement schemes.
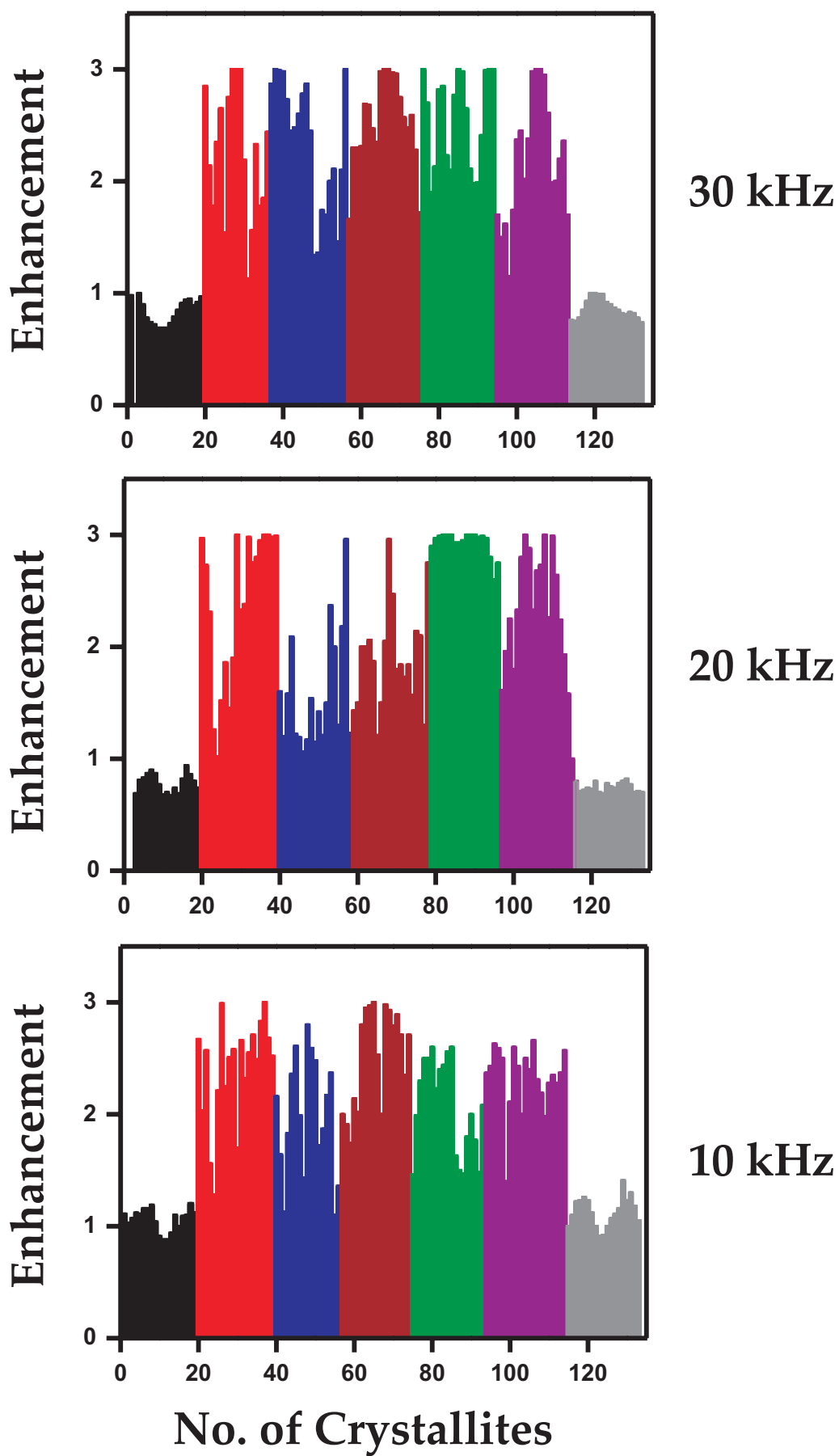
Figure 2.4: Enhancements of individual crystallites under FAM scheme.

normal scheme for spin-3/2 system is shown in Fig 2.5. This modification on the FAM sequence enables one to affect different domains of the powder orientations in a spinning sample more effectively thereby achieving more enhancement.
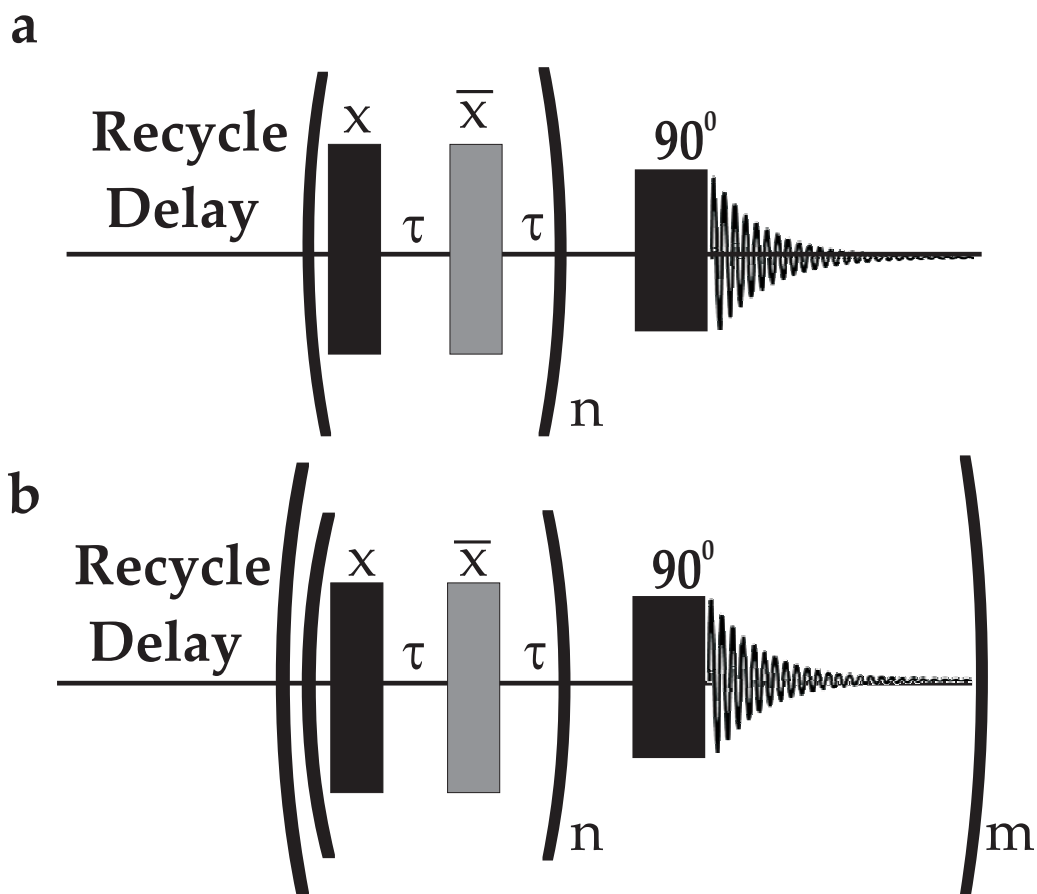
Figure 2.5: (a) FAM pulse sequence for spin-3/2 nuclei where n is the loop counter of the FAM pulse train. (b) m-FAM pulse sequence for spin-3/2 nuclei where m is the total loop counter of FAM-90^0-acquisition before the recycle delay. τ is the interpulse delay of the FAM train.

2.4.2 NMR of ^{23}Na (I=3/2) in Na$_2$SO$_4$

Table 2.2 shows the results obtained with the application of FAM and *m*-FAM pulses observing the ^{23}Na resonance of Na$_2$SO$_4$. It is quite evident that *m*-FAM outperforms FAM as seen from Table 2.2.

Table 2.2: Experimental signal enhancement obtained with FAM and *m*-FAM for ^{23}Na and ^{27}Al spin systems (quoted with an accuracy of ±5%)

Nucleus	Spin	FAM Enhancement	*m*-FAM Enhancement
^{23}Na	3/2	1.7	3.3
^{27}Al	5/2	2.1	6.9

To investigate the robustness of the FAM sequences with respect to the nutation frequency of the pulses and the MAS frequency, the signal enhancement factors were noted for FAM and *m*-FAM as a function of these variables. Figure 2.6a shows the signal enhancement factor for FAM and *m*-FAM plotted as a function of the nutation frequency of the FAM pulses, ν_{nut}^{FAM}. The FAM blocks were optimised for a nutation frequency of 53 kHz. Figure 2.6b shows the signal enhancement factor for FAM and *m*-FAM plotted as a function of the nutation frequency of the central-transition selective 90° pulses, $\nu_{nut}^{90°}$. In both Figs. 2.6a and 2.6b the respective nutation frequencies were varied from 25 kHz to 95 kHz. Figure 2.6c shows the signal enhancement factor for FAM and *m*-FAM plotted as a function of the MAS frequency ν_r where ν_r was varied from 6 kHz to 12 kHz in steps of 1 kHz. The maximum drop in the efficiency of the schemes for the three experimental variables considered is given in Table 2.3.

It is clearly seen that *m*-FAM is much superior to and robust than normal FAM for signal enhancement under MAS conditions.

m-FAM applied on Na$_2$SO$_4$ under static conditions gave a signal enhancement of a factor of 2.0 compared with a single 90° pulse, whilst regular FAM did not yield any
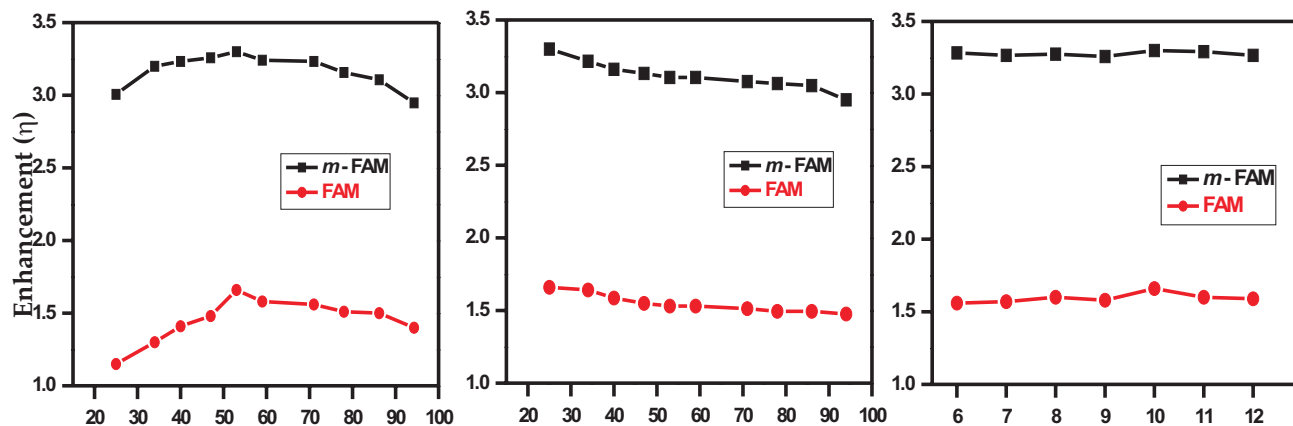
Figure 2.6: Signal-enhancement factor for spinning ^{23}Na sample as a function of (a) the nutation frequency of the FAM pulses v_{nut}^{FAM}, (b) the nutation frequency of the 90^0 pulse $v_{nut}^{90^o}$, and (c) the spinning speed v_r. Squares represent the result with m-FAM and circles represent the result with FAM.

appreciable signal enhancement (data not shown). This aspect will be discussed in detail in the next Section with reference to the spin-5/2 system.

Table 2.3: Maximum drop in the optimised signal (expressed in terms of %) with FAM and m-FAM as a function of v_{nut}^{FAM}, $v_{nut}^{90^o}$, and v_r for ^{23}Na (I=3/2).

Variables	FAM	m-FAM
v_{nut}^{FAM}	30.8	10.7
$v_{nut}^{90^o}$	11.2	10.6
v_r	4.9	1.1

2.4.3   NMR of ^{27}Al (I=5/2) in Gibbsite under MAS

For the spin-5/2 case the performance efficiency of FAM, m-FAM, and rotor-synchronised m-FAM schemes were investigated observing the ^{27}Al resonance of a sample of gibbsite.

Figure 2.7 shows the one-dimensional (1D) MAS [27]Al spectra of gibbsite acquired at $v_r = 10$ kHz with a single 90º pulse, multiple 90º pulse (90º pulses were implemented as in the case of *m*-FAM scheme), FAM, *m*-FAM, and rotor-synchronised *m*-FAM schemes. Clearly *m*-FAM performs better than regular FAM with enhancement factors reported in Table 2.1. It may be noted that the rotor-synchronised *m*-FAM scheme performs as well as *m*-FAM (factor of 6.7 against 6.85 with respect to a single 90º pulse scheme). Interestingly, the *m*-90º scheme outperforms regular FAM, whilst *m*-FAM is still better by a factor of nearly 2.5 in comparison with *m*-90º. There are no appreciable line shape distortions here which were also evident in the case of spin-3/2 system (data not shown).

To investigate the robustness of the FAM sequences with respect to the nutation frequency of the pulses and the MAS rate, the signal enhancement factors were noted for FAM, *m*-FAM, and rotor-synchronised *m*-FAM schemes as a function of these variables. Figure 2.8a shows the signal enhancement factor for all the schemes plotted as a function of the nutation RF of the FAM pulses, v_{nut}^{FAM}. The FAM blocks were optimised for a nutation frequency of 53 kHz. Figure 2.8b shows signal enhancement factor for all the schemes plotted as a function of the nutation frequency of the central-transition selective 90º pulses, $v_{nut}^{90º}$. In both Figs. 2.8a and 2.8b the respective nutation frequencies were varied from 30 kHz to 95 kHz. Figure 2.8c shows the signal enhancement factor for all the schemes plotted as a function of the MAS frequency v_r where v_r was varied from 6 kHz to 12 kHz in steps of 1 kHz. The maximum drop in the efficiency of the schemes for the three experimental variables considered is given in Table 2.4.

It is clearly seen that *m*-FAM is much superior to normal FAM and rotor-synchronised *m*-FAM in terms of robustness with respect to experimental parameters and could be easily implemented experimentally.

The signal-enhancement feature of *m*-FAM can be attributed to the multiple transfer of population from satellite transitions to central transition before the spin system attains thermal equilibrium. For every such transfer made possible, the central-transition
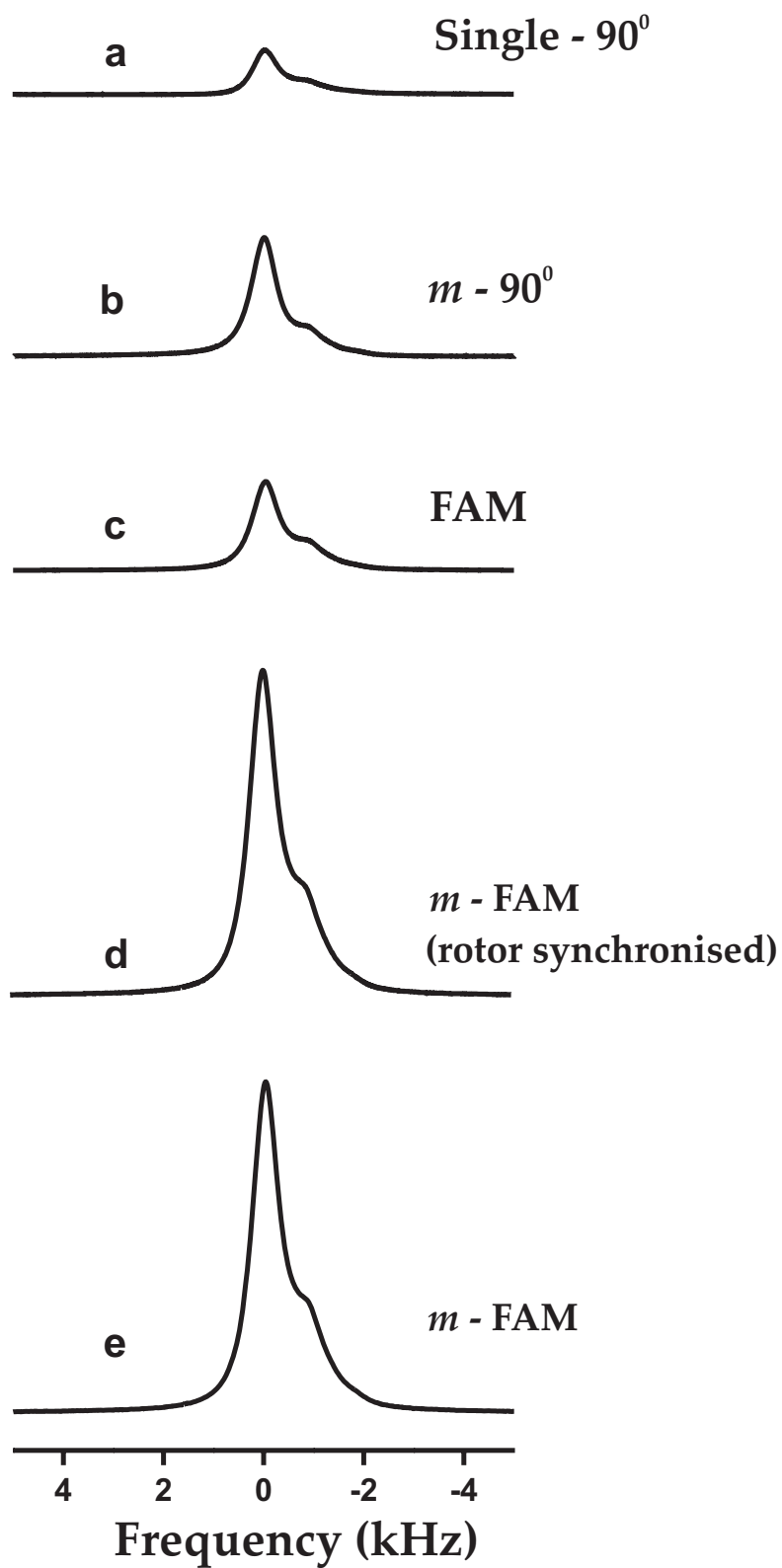
Figure 2.7: ^{27}Al NMR spectra of gibbsite with different pulse schemes under MAS. (a) Single 90^0 pulse, (b) repetitive 90^0 pulse *m*-90°, (c) FAM, (d) rotor synchronised *m*-FAM, and (e) *m*-FAM.
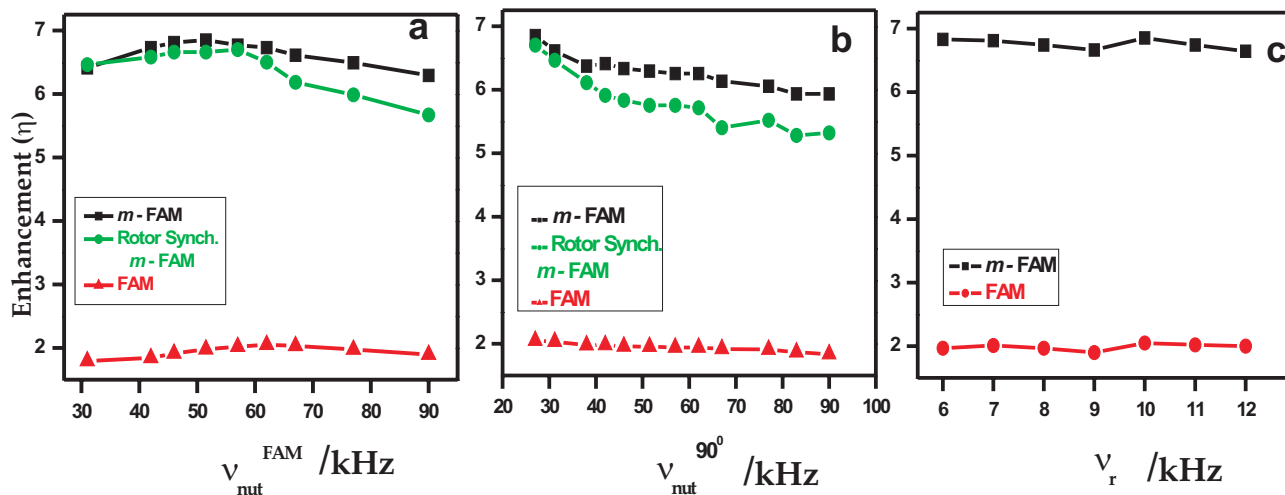
Figure 2.8: Signal-enhancement factor for spinning ^{27}Al sample as a function of (a) the nutation frequency of the FAM pulses v_{nut}^{FAM}, (b) the nutation frequency of the 90^0 pulse $v_{nut}^{90^o}$, and (c) the spinning speed v_r. In a and b squares, circles, and triangles correspond to *m*-FAM, rotor-synchronised *m*-FAM, and FAM respectively. In c squares and circles correspond to *m*-FAM and FAM respectively.

Table 2.4: Maximum drop in the optimised signal (expressed in terms of %) with FAM, *m*-FAM, and rotor synchronised *m*-FAM as a function of v_{nut}^{FAM}, $v_{nut}^{90^o}$, and v_r for ^{27}Al (I=5/2)

Variables	FAM	*m*-FAM	Rotor Synchronised *m*-FAM
v_{nut}^{FAM}	12.5	8.1	15.4
$v_{nut}^{90^o}$	10.5	13.4	20.6
v_r	7.5	3	-

selective 90° pulse acts nearly on a similar range of crystallites accounting for the almost similar dependence on $v_{nut}^{90°}$ of all the schemes. Additional robustness of the m-FAM with respect to both v_{nut}^{FAM} and v_r may be attributed to different parts of the powder being influenced by the FAM pulses as either of these change where then a multiple transfer of population takes place. In other words, any change in the experimental variable, either v_{nut}^{FAM} or v_r, simply changes the domain of action of the FAM pulses in a powder, but wherever they act an optimum multiple transfer of population from satellite transition to central transition is obtained thereby keeping the signal-enhancement factor nearly the same. If this were true, a rotor-synchronised m-FAM scheme would not be as effective as the m-FAM scheme as by virtue of rotor synchronisation the FAM pulses can only affect the same range of crystallites in a powder for all values of v_{nut}^{FAM} or $v_{nut}^{90°}$. This would then lead to a dependence of the rotor-synchronised m-FAM scheme on these variables, and this is clearly borne out from the experiments as shown in Table 2.4. All the above arguments are also valid in the earlier discussed case of spin-3/2 system.

2.4.4   NMR of ^{27}Al (I=5/2) in Gibbsite in Static Condition

It has been shown earlier that SW($1/\tau$)-FAM performs best in static cases with respect to the simple FAM [77]. Experiments were performed observing ^{27}Al resonance of gibbsite under static conditions with SW($1/\tau$)-FAM, m-FAM, and multiple SW($1/\tau$)-FAM. The SW($1/\tau$)-FAM scheme was composed of 12 pulse pairs with the pulse length and the window duration being the same. The initial pulse duration was 0.4 μs and the final pulse duration was 7.2 μs. The sweep width was 486 kHz. The nutation frequency of the FAM pulses was 62 kHz. Both m-FAM and m-SW($1/\tau$)-FAM schemes were repeated 10 times before the spin system attained thermal equilibrium. Regular FAM pulses were nearly ineffective in the static case. Compared to a single 90° pulse, SW($1/\tau$)-FAM gave a signal enhancement of 2.1. The m-FAM scheme gave a signal enhancement of 5.46 whilst the m-SW($1/\tau$)-FAM gave a factor of 6.64. Such enhancements could be very

useful in the NMR of quadrupolar nuclei under static cases.

Figures 2.9a and 2.9b show the signal-enhancement factor obtained with m-FAM, SW$(1/\tau)$-FAM, and m-SW$(1/\tau)$-FAM as a function of v_{nut}^{FAM} and $v_{nut}^{90^o}$ respectively, with the former being varied from 30 kHz to 85 kHz and the latter being varied from 25 kHz to 85 kHz. As evident from Figs. 2.9a and b m-FAM and m-SW$(1/\tau)$-FAM show lesser dependence on v_{nut}^{FAM} whilst all the three schemes show a similar dependence on $v_{nut}^{90^o}$. This observation again proves the superior performance of multiple FAM schemes. The maximum drop in the efficiency of the schemes for the two experimental variables considered is given in Table 2.5.
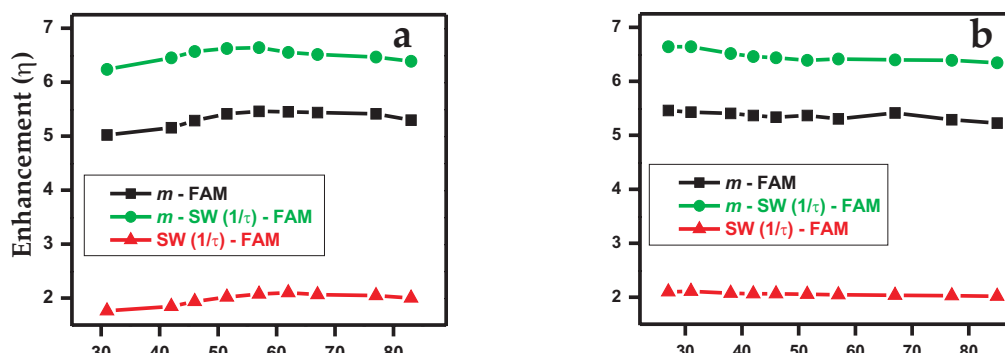
Figure 2.9: Signal-enhancement factor as a function of (a) the nutation frequency of the FAM pulses v_{nut}^{FAM} and (b) the nutation frequency of the 90^0 pulse $v_{nut}^{90^o}$ for static ^{27}Al sample. Squares, circles, and triangles represent m-FAM, m-SW$(1/\tau)$-FAM, and SW$(1/\tau)$-FAM respectively.

From the experiments considered here, m-FAM schemes gave much higher signal enhancement than FAM both in the spinning and the static case, which was also true between SW$(1/\tau)$-FAM and m-SW$(1/\tau)$-FAM in the static case where the latter gave much higher enhancement than the former. This happens as performing FAM and SW$(1/\tau)$-FAM in a multiple way without allowing the spin system to reach thermal equilibrium

Table 2.5: Maximum drop in the optimised signal (expressed in terms of %) with SW($1/\tau$)-FAM, m-FAM, and m-SW($1/\tau$)-FAM as a function of ν_{nut}^{FAM} and $\nu_{nut}^{90^\circ}$ for ^{27}Al (I=5/2) in static condition.

Variables	SW($1/\tau$)-FAM	m-FAM	m-SW($1/\tau$)-FAM
ν_{nut}^{FAM}	16.1	8.1	6.2
$\nu_{nut}^{90^\circ}$	3.9	4.3	4.5

transfers a larger part of polarisation from the satellite to the central transition. It is also observed that m-FAM is quite robust with respect to change in the nutation RF of the modulation pulses, ν_{nut}^{FAM}, and the MAS rate, ν_r, but when the nutation RF of the 90° pulses, $\nu_{nut}^{90^\circ}$, was changed m-FAM scheme behaves almost comparably in different nuclei (^{23}Na and ^{27}Al) and also under different conditions (spinning and static). One can argue that since the 90° pulse is not a part of the modulation changing the nutation RF of the 90° pulse manifests relatively similarly with FAM and m-FAM under different conditions and with different nuclei.

2.5 Simulation Programs

In this section the numerical simulation programs are given which were used to simulate the powder spectrum of a spin-5/2 system under different enhancement schemes.

2.5.1 Hyperbolic Secant

$\neq$ powderhs.in

$\qquad$ $\neq$ Spin-5/2 central-line intensity calculation with Hyperbolic Secant pulses for

$\qquad$ $\neq$ population inversion of satellites

$\qquad$ $\neq$ for a powder rotating at the magic angle,

$\qquad$ $\neq$ submitted to the first- and the second-order

$\neq$ quadrupole interactions.

```
spinsys {
channels 27Al
nuclei 27Al
quadrupole 1 2 3.0e6 0.2 0 0 0
}
par {
proton_frequency 500e6
spin_rate 10000
sw 1.0e5
np 1600
crystal_file rep2000
gamma_angles 20
start_operator I1z
detect_operator I1c
verbose 1101
variable rf 2000
}
proc hspulse { tau wrfmax phase } {
set fmax 10e3
set dt 2.0
set w [expr 2*3.1416*190000]
set steps [expr int(round($tau/$dt/2))]
set phi0 [expr 180.0*$fmax*$tau/10.6e6]
for {set i −$steps} {$i <$steps} {incr i} {
set x [expr cosh(10.6*$dt*$i/$tau)]
set phi [expr $phase + $phi0*log($x)]
```

```
set rf [expr $wrfmax/$x]

set newrf [expr 2.0*$rf*cos($phi+$w*$dt*$i)]

if { $newrf < 0} {

set newrf [expr -$newrf]

set phi [expr $phi + 180]

}

pulse $dt $newrf $phi

}

}

proc pulseq {}{

global par

maxdt 0.2

hspulse 700 9000 0

offset 0

set tsw [expr .083e6/$par(rf)]

pulse $tsw $par(rf) x

acq -y

for {set i 1}{$i <$par(np)}{incr i}{

delay 10

acq -y

}

}

proc main {}{

global par

set f [fsimpson]

fsave [fsimpson] $par(name).fid

fzerofill $f 4096
```

```
≠ f addlb$f 100

fft $f

fsave $f $par(name).txt -xreim

fsave $f $par(name).spe

funload $f

puts "Larmor frequency (Hz) of 27Al: "

puts [resfreq 27Al $par(proton_frequency)]

}
```

2.5.2   Double Frequency Sweep

```
≠ powderdfs.in

    ≠ Spin-5/2 central-line intensity calculation with DFS pulses for

    ≠ population inversion of satellites

    ≠ for a powder rotating at the magic angle,

    ≠ submitted to the first- and the second-order

    ≠ quadrupole interactions.

    spinsys {

    channels 27Al

    nuclei 27Al

    quadrupole 1 2 3.0e6 0.2 0 0 0

    }

    par {

    proton_frequency 500e6

    spin_rate 10000

    sw 1.0e5

    np 1600

    crystal_file rep2000
```

```
gamma_angles 20

start_operator I1z

detect_operator I1c

verbose 1101

variable rf 2000

}

proc dfspulse { tau wrfmax phase} {

set dt 2.0

set steps [expr int(round($tau/$dt))]

for {set i -$steps} {$i <$steps}{incri}{

set x [expr cos(2*3.14*1200e3*$dt*$i-2*3.14*1050e3*$dt*$dt*$i/2*$tau)]

set phi 0

set rf [expr $wrfmax*$x]

if {$rf < 0}{

set rf [expr -$rf]

set phi [expr $phi + 180]

}

pulse $dt $rf $phi

}

}

proc pulseq {}{

global par

maxdt 0.2

dfspulse 200 30000 0

offset 0

set tsw [expr .083e6/$par(rf)]

pulse $tsw $par(rf) x
```

```
acq -y

for { set i 1} {$i <$par(np)}{incri}{

delay 10

acq -y

}

}

proc main {}{

global par

set f [fsimpson]

fsave [fsimpson] $par(name).fid

fzerofill $f 4096

faddlb $f 10 0

fft $f

fsave $f $par(name).txt -xreim

fsave $f $par(name).spe

funload $f

puts "Larmor frequency (Hz) of 27Al: "

puts [ puts [resfreq 27Al $par(proton_frequency)]]

}
```

2.5.3   Gaussian Pulse

```
≠ powdergs.in

    ≠ Spin-5/2 central-line intensity calculation with Gaussian pulses for

    ≠ population saturation of satellites

    ≠ for a powder rotating at the magic angle,

    ≠ submitted to the first- and the second-order

    ≠ quadrupole interactions.
```

```
spinsys {

channels 27Al

nuclei 27Al

quadrupole 1 2 3.0e6 0.2 0 0 0

}

par {

proton_frequency 500e6

spin_rate 10000

sw 1.0e5

np 1600

crystal_file rep2000

gamma_angles 20

start_operator I1z

detect_operator I1c

verbose 1101

variable rf 2000

}

proc gauss { tau wrfmax phase} {

set dt .2

set w 4.94

set a [expr 619/$w*sqrt(3.1416/2)]

set steps [expr int(round($tau/$dt))]

for { set i -$steps} {$i <$steps}{incri}{

set x [expr {exp(-2*(($dt*$i-$tau)/$w)*(($dt*$i-$tau)/$w))}]

set phi 0

set rf [expr $wrfmax*$a*$x]

pulse $dt $rf $phi
```

```
}
}
proc gauss1 {tau wrfmax phase} {
set dt .2
set w 4.94
set a [expr 619/$w*sqrt(3.1416/2)]
set steps [expr int(round($tau/$dt))]
for { set i -$steps} {$i <$steps}{incr i}{
set y [expr {exp(-2*(($dt*$i+$tau)/$w)*(($dt*$i+$tau)/$w))}]
set phi1 0
set newrf [expr $wrfmax*$a*$y]
pulse $dt $newrf $phi1
}
}
proc gauss2 { tau wrfmax phase} {
set dt .2
set w 4.94
set a [expr 619/$w*sqrt(3.1416/2)]
set steps [expr int(round($tau/$dt))]
for { set i -$steps} {$i <$steps}{incr i}{
set x [expr {exp(-2*(($dt*$i-$tau)/$w)*(($dt*$i-$tau)/$w))}]
set phi 180
set rf [expr $wrfmax*$a*$x]
pulse $dt $rf $phi
}
}
proc gauss3 {tau wrfmax phase} {
```

```
set dt .2

set w 4.94

set a [expr 619/$w*sqrt(3.1416/2)]

set steps [expr int(round($tau/$dt))]

for { set i -$steps} {$i <$steps}{incri}{

set y [expr {exp(-2*(($dt*$i+$tau)/$w)*(($dt*$i+$tau)/$w))}]

set phi1 180

set newrf [expr $wrfmax*$a*$y]

pulse $dt $newrf $phi1

}

}

proc pulseq {}{

global par

maxdt 1 for { set j 1} {$j < 2}{incrj}{offset 220000

gauss 7.49 5000 0

gauss1 7.49 5000 0

offset -220000

gauss2 7.49 5000 0

gauss3 7.49 5000 0

}

offset 0

set tsw [expr .083e6/$par(rf)]

pulse $tsw $par(rf) x

acq -y

for { set i 1} {$i <$par(np)}{incri}{

delay 10

acq -y
```

```
}
}
proc main {}{
global par
set f [fsimpson]
fsave [fsimpson] $par(name).fid
fzerofill $f 4096
faddlb $f 10 0
fft $f
fsave $f $par(name).txt -xreim
fsave $f $par(name).spe
funload $f
puts "Larmor frequency (Hz) of 27Al: "
puts [resfreq 27Al $par(proton_frequency)]
}
```

2.5.4 Fast Amplitude Modulated (FAM) Pulse

```
≠ powderfam.in
    ≠ Spin-5/2 central-line intensity calculation with FAM pulses for
    ≠ population saturation of satellites
    ≠ for a powder rotating at the magic angle,
    ≠ submitted to the first- and the second-order
    ≠ quadrupole interactions.
    spinsys {
    channels 27Al
    nuclei 27Al
    quadrupole 1 2 3.0e6 0.2 0 0 0
```

```
}
par {
proton_frequency 500e6
spin_rate 10000
sw 1.0e5
np 1600
crystal_file rep2000
gamma_angles 20
start_operator I1z
detect_operator I1c
verbose 1101
Variable rf_fam 24000
variable rf 4000
}
proc pulseq {}{
global par
maxdt 1
for { set i 1} {$i < 25}{incri}{
pulse 1 $par(rf_fam) x
delay 1
pulse 1 $par(rf_fam) -x
delay 1
}
for { set j 1} {$j < 25}{incri}{
pulse 1.4 $par(rf_fam) x
delay 1
pulse 1.4 $par(rf_fam) -x
```

```
delay 1
}
≠ matrix set detect elements 3 4
set tsw [expr .083e6/$par(rf)]
pulse $tsw $par(rf) x
acq -y
for { set k 1 } {$k <$par(np)}{incrk}{
delay 10
acq -y
}
}
proc main {}{
global par
set f [fsimpson]
fsave [fsimpson] $par(name).fid
fzerofill $f 4096
faddlb $f 10 0
fft $f
fsave $f $par(name).txt -xreim
fsave $f $par(name).spe
funload $f
puts "Larmor frequency (Hz) of 27Al: "
puts [resfreq 27Al $par(proton_frequency)]
}
```

2.6 Conclusions

In this chapter we have described the salient features of m-FAM. It was shown in this chapter that m-FAM gives better signal enhancement than FAM and is much more robust to the nutation RF of the FAM pulses and the MAS frequency than FAM. m-FAM also performs better than SW$(1/\tau)$-FAM in static condition, however, m-SW$(1/\tau)$-FAM outperforms m-FAM. Both m-SW$(1/\tau)$-FAM and m-FAM show very little dependence on the change of the nutation frequency of the FAM pulses from the optimised value where as SW$(1/\tau)$-FAM showed an appreciable amount of dependence. From the results obtained with the simulations on single crystal we expect that the Gaussian pulse pairs, DFS scheme, and hyperbolic secant pulses also will show the same robustness features as was shown for FAM when applied in a multiple fashion. It is expected that the robustness features of these schemes will make the application of these towards sensitivity enhancement of the spectra of half-integer spin quadrupolar nuclei more routine.

Chapter 3

Characterisation of Different Polymorphs of Alq$_3$ Using Solid-State NMR and DFT Calculations

3.1 Introduction

In organic based semiconductor devices, molecular solids of organic molecules are used in active layers [83]. The properties of amorphous solid thin films can be different from the properties of isolated molecule, due to interaction among the molecules in solid state. The properties of amorphous solid thin films are mainly decided at the molecular level and modulated by intermolecular interactions and other bulk properties. Hence, it is important to have information about the structure of the organic molecule, charge distribution on the molecular framework, and intermolecular interactions as they collectively govern the performance of the device.

Following the experimental demonstration by Tang *et al.* [84] Tris(8-hydroxyquinolinato)-aluminium(III), known as Alq$_3$, has become a workhorse material for organic light emitting devices (OLED) and/or electron transporting material in OLED. Alq$_3$ is an oc-
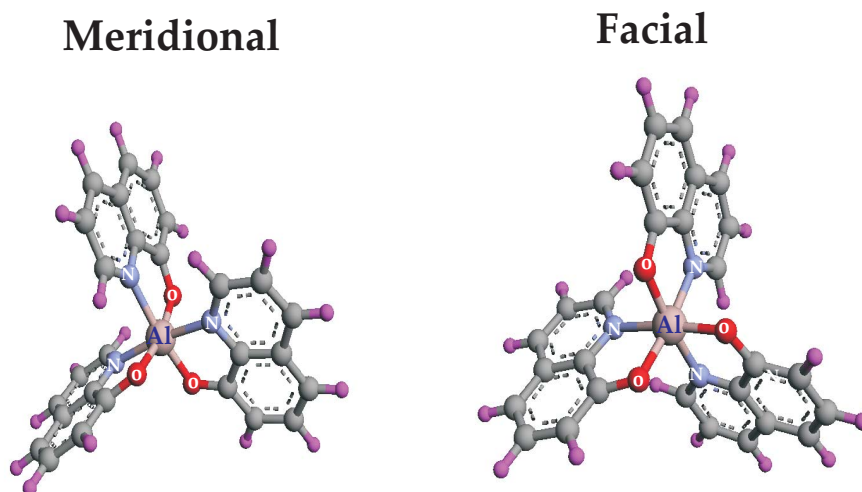
Meridional   **Facial**

Figure 3.1: Meridional and Facial geometrical isomers of Alq$_3$

tahedrally coordinated chelate complex, with an Al^{3+} ion in the center and three 8-hydroxyquinolinate ions octahedrally coordinated around it. It has mainly two types of geometrical isomeric forms, meridional and facial. Brinkmann *et al.* investigated the light emitting properties of the isomeric states and the polymorphs of Alq$_3$ and determined that molecular packing plays a significant role [85]. X-ray diffraction studies showed that the two crystalline polymorphs of Alq$_3$, α and β forms, are mainly composed of the meridional isomer [85]. Recently a new crystalline phase of Alq$_3$, namely δ-Alq$_3$, was discovered [86]. It shows blue luminescence which is markedly different from the meridional isomer which shows green luminescence. The quantum yield is also higher in the δ-phase. These results suggest that there is a clear correspondence between the crystal structure of Alq$_3$ and the photoluminescence property. Extensive studies on the δ-phase of Alq$_3$ have been carried out and it was suggested that δ-Alq$_3$ is composed purely of facial Alq$_3$ [87, 88]. Again in the case of charge carrier transport in Alq$_3$, intermolecular interactions play the most crucial role [89]. Also, it has been a

practice to use different dopants in Alq_3 emitting layers to obtain desired colours [83]. Such Alq_3 systems which accommodate small solvent molecules within its crystal matrix are in general known as solvated Alq_3. It was also reported that the unit crystal structure and the crystal packing change in Alq_3 when it hosts small solvent molecules, which resulted in a small red shift in the fluorescence spectra [85].

Considering the above stated facts, it becomes important to have insight about the structure of Alq_3 in both the solvated and the unsolvated form and about the intramolecular and intermolecular interactions. Though X-ray diffraction is a powerful tool to yield insight into the structure of crystalline material, solid-state NMR can be as good in providing similar information. In addition, solid-state NMR is particularly suitable for studying disordered or amorphous materials [90–95]. Since Alq_3 has an Al^{3+} ion in the centre, one can make use of it as a probe to monitor the electronic distribution in the molecule. ^{27}Al is well suited for solid-state NMR because of its high natural abundance (100%) and relatively large gyromagnetic ratio. Since ^{27}Al has spin $I = 5/2$, it possesses a quadrupolar moment [96]. It is possible to record and analyse solid-state ^{27}Al MAS NMR spectra, observing the central m=+1/2←→-1/2 magnetic transition under magic-angle spinning (MAS), which, for well-resolved spectra, exhibits a characteristic second-order order broadening. High-resolution quadrupolar spectra can be obtained with two-dimensional (2D) methods such as multiple-quantum MAS (MQMAS) [14]. This can help in identifying the various quadrupolar sites in a system and in obtaining the quadrupolar parameters [97,100]. The study of quadrupolar parameters with solid-state NMR can provide a wealth of information about the local environment around quadrupolar nuclei, as the quadrupolar parameters show strong dependence on the neighbouring electronic environment [96,101].

Octahedral chelate complexes, which are structurally similar to Alq_3, were studied by Schurko and co-workers using one-dimensional (1D) ^{27}Al MAS NMR spectroscopy [102]. They showed that the change of structural environment about the aluminium centres

can be easily investigated by studying the quadrupolar parameters of ^{27}Al nuclei of the organic chelate complexes. They also reported how the distortion in the chelate rings leads to larger value of quadrupolar coupling constant in one of the complexes.

Recently Utz *et al.* [92, 93] have successfully used 1D MAS ^{27}Al spectroscopy to differentiate between the α phase and the δ phase of Alq$_3$ and to characterise the structural disorder of amorphous Alq$_3$ deposited from vapour phase at different rates. They also estimated the EFG tensor on the basis of point charge model and predicted the asymmetry parameters of the α and the δ phase [92]. Kaji *et al.* have done a similar study by recording 1D ^{27}Al spectra under static and MAS condition to characterise the α phase, the δ phase, and the γ phase of Alq$_3$ and also amorphous Alq$_3$ [103]. However unlike Utz *et al.* they have used DFT based quantum-chemical calculations to theoretically predict the value of the asymmetry parameters of the α phase and the γ phase. Their study suggested that whilst the α phase contains a non axially symmetric isomer both the δ phase and the γ phase of Alq$_3$ contain an axially symmetric form.

This chapter experimental investigation of three types of Alq$_3$ samples: (a) α phase (containing the meridional isomer), (b) δ phase (containing the facial isomer), and (c) solvated phase (containing ethanol in the crystal lattice) using solid-state NMR combined with density functional theory (DFT) [104] based quantum chemical calculation. We show with MQMAS experiments that in all the polymorphs, ^{27}Al is present in a single crystallographic site. We further demonstrate that the local environment around ^{27}Al in solvated phase is different from that in the α phase with the use of both 1D MAS and 2D MQMAS experiments. We also made use of DMFIT [135] program to model the 1D MAS spectra of all the polymorphs to extract the quadrupolar parameters and we have compared the results with the previous works. In addition the anisotropic slices of the peaks in 2D MQMAS spectra were modelled using the DMFIT program to extract the quadrupolar parameters and isotropic chemical shifts. We further report the result obtained from DFT based quantum-chemical calculation done on isolated molecule and

show that the correspondence with the experimental results improve when the calculation is done under the solvation model.

3.2 Materials and Methods

3.2.1 Preparation of Alq$_3$ and X-ray Diffraction Measurements

Alq$_3$ was prepared from 8-hydroxyquinoline and Al(NO$_3$).9H$_2$O using an aqueous route by a standard procedure [106]. Briefly the procedure adopted was as follows: 1 g of aluminium nitrate (Al (NO$_3$)$_3$).9H$_2$O was dissolved in 100 ml of water. The solution was warmed to 60°C. 1.5 g of 8-hydroxyquinoline was dissolved in a solvent mixture of 20 ml of water and 4 ml of glacial acetic acid. 8-hydroxyquinoline solution was slowly added to aluminium nitrate solution. The pH of the resulting solution was then increased to 8 by the addition of ammonia to precipitate Alq$_3$ out. The resulting precipitate was washed by hot (60°C) water. The bright yellow powder was dried in oven for overnight. Yield of Alq$_3$ obtained by this method was 95-100% with a melting point > 300°C. This procedure was adapted from Vogel [107].

Alq$_3$, as prepared, was subjected to train sublimation under vacuum and purified [106]. Alq$_3$ gets deposited in different temperature zones. The portion which was deposited at $\sim$ 175°C was collected. Powder XRD pattern of the sample matched with the reported pattern for the α phase of Alq$_3$ [85], which is well established to be the meridional isomer of Alq$_3$. Fluorescence emission spectra in thin film showed a maximum at 510 nm (Figure 1). Facial isomer of Alq$_3$ was prepared by thermal annealing process [108]. A quartz tube with N$_2$ gas flow arrangement at high pressure was used in the preparation. The temperature of the tube was regulated by a heater coil. Alq$_3$, purified by train sublimation (containing α and other phases of Alq$_3$), was loaded on an alumina boat kept inside the chamber. The chamber was flushed with N$_2$ for 2 hrs. The pressure was kept at 1.5 atm. The temperature of the chamber was increased from

room temperature to 350°C at the rate of 10°C/min. The temperature was then further increased to 400°C at the rate of 1°C/min. The system was kept at this temperature for 30 minutes. Temperature of the sample was then brought down to room temperature rapidly by removing it from the heating zone under continuous flow of N$_2$. A suspension of the annealed sample was made with acetone (7mg/ml). The suspension was kept for 24 hours with occasional shaking. The suspension was centrifuged at 13000 r.p.m. The grayish-white sample obtained at the bottom of the centrifuge tube was dried over vacuum and kept in glass vials for further study. Powder XRD pattern of the δ phase of Alq$_3$ matched with the previously reported pattern [87]. Fluorescence emission spectra in thin film showed a maximum at 468 nm (Figure 1). XRD pattern and fluorescence spectrum confirmed the sample to be the facial isomer of Alq$_3$. The ethanol solvated phase was prepared by recrystallising Alq$_3$ from ethanol. Fluorescence emission spectra in thin film showed a maximum at 510 nm (Figure 1). Powder XRD pattern showed a close resemblance with the reported solvated phase of the form Alq$_3$ (C$_6$H$_5$Cl)$_{1/2}$ where C$_6$H$_5$Cl acts as an inclusion or guest compound within Alq$_3$ crystal [85]. Alq$_3$-ethanol solvated phase was annealed at $\sim$ 200°C under nitrogen atmosphere for 2 hrs to remove ethanol from the crystal lattice. X-ray powder diffraction data were obtained with Philips instrument (panalytica) with a Cu Kα (λ= 1.5418A°) radiation source. Data were recorded at room temperature in 2θ mode (Δ2θ=0.017).

3.2.2 Fluorescence Measurements

Steady-state fluorescence of powdered Alq$_3$ samples was recorded at room temperature using a Spex Fluorolog fluorimeter. The excitation wavelength was 340 nm and scanned at a step of 1 nm.
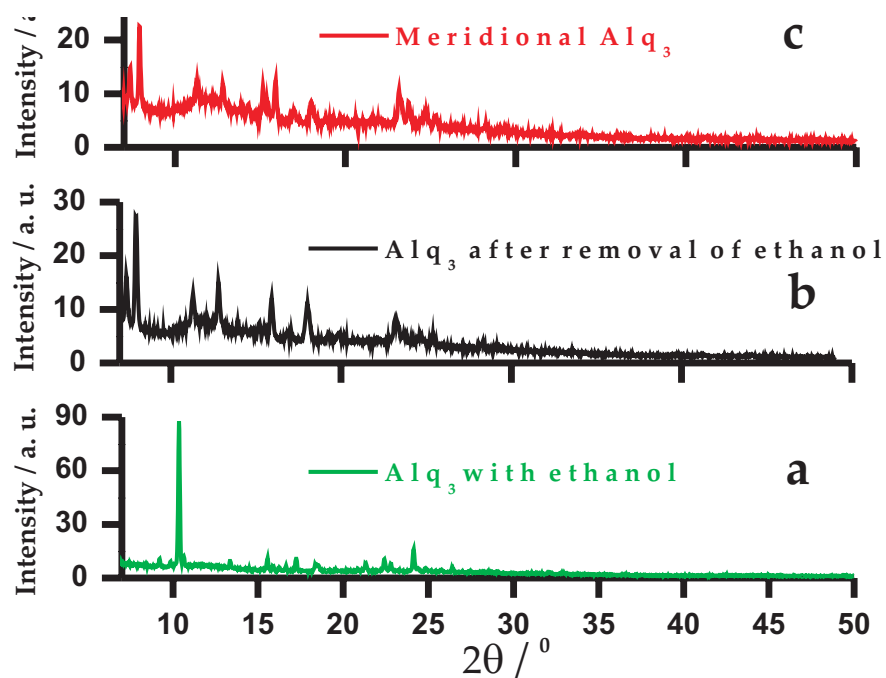
Figure 3.2: XRD data of (a) solvated Alq$_3$, (b) after the removal of ethanol, and (c) the α-phase of Alq$_3$ (meridional).
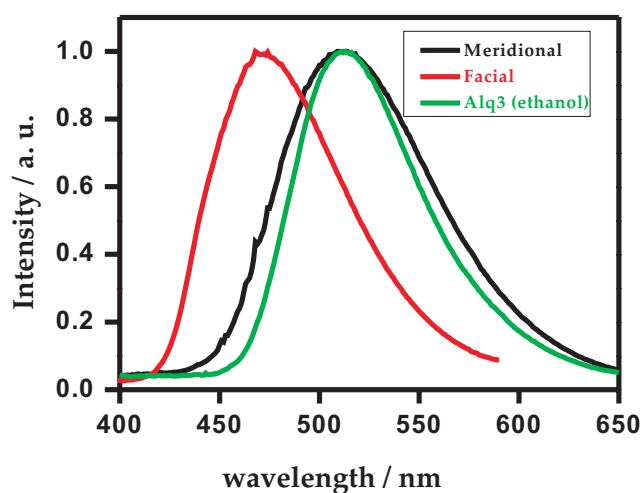
Figure 3.3: The fluorescence emission spectra of a thin film of the α-phase of Alq$_3$ (meridional), the δ-phase of Alq$_3$ (facial), and the solvated Alq$_3$ containing ethanol.

3.2.3 Thermo-Gravimetric Measurements

Thermo-gravimetric analysis (TGA) and differential thermal analysis (DTA) were performed with a NETZSCH instrument. The temperature was varied at 5 K/min under nitrogen atmosphere.
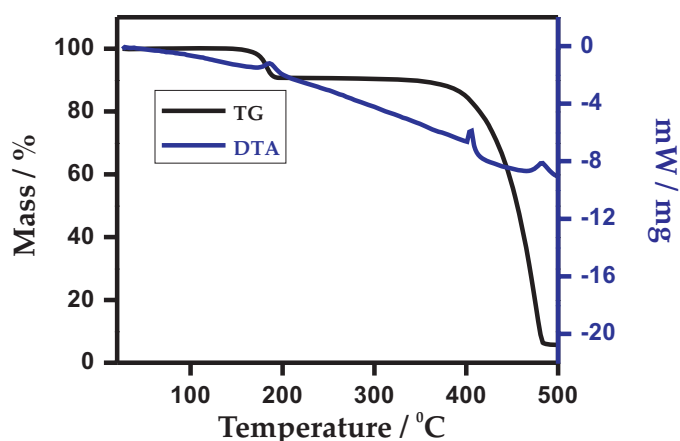
Figure 3.4: Thermo-gravimetric analysis (TGA) and differential thermal analysis (DTA) plots of solvated Alq$_3$ containing ethanol.

3.2.4 NMR Experiments

All NMR experiments were carried out on a Bruker Avance 500 MHz spectrometer operating at a field strength of 11.7 T with a Bruker 4 mm triple-resonance probe. Experiments were performed observing the central transition of ^{27}Al (I=5/2) resonance of the different forms of Alq$_3$ sample at a Larmor frequency of 130.28 MHz. Magic-angle spinning was performed at 10 kHz. The nutation frequency of the excitation pulse for the 1D MAS experiments was 120 kHz. For the 2D experiments the split-t_1 sequence

proposed by Brown and Wimperis was used [21]. A nutation frequency of 80 kHz was applied for excitation and conversion pulses. The echo time was 2.5 ms. The pulse width of the selective 180° pulse was 27.8 μs. Further experimental details are given in the figure captions of Figs. 3.5, 3.6, 3.7, and 3.8. The chemical shifts were referenced to aqueous 1M $AlCl_3$ solution.
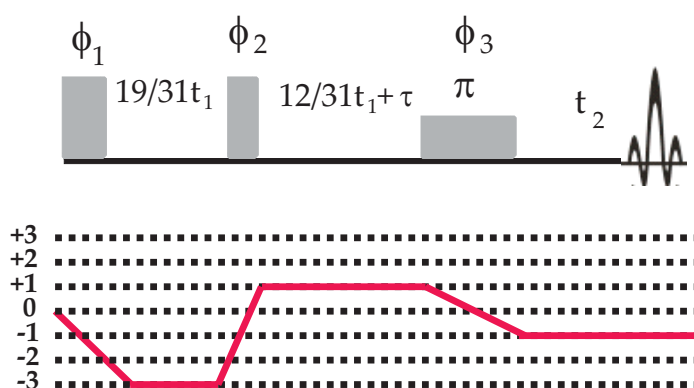
Figure 3.5: Split-t_1 3QMAS pulse scheme with coherence pathways applicable for spin-5/2 systems according to Ref. [21]. ϕ_1, ϕ_2, and ϕ_3 are the phases of the excitation, reconversion and the selective π pulses.

The isotropic quadrupolar shifts from the MQMAS spectra, ν_Q^{iso}, were calculated using the method given in Ref. [97]. In all the experiments swept-frequency two pulse phase modulation (SW_f-TPPM) [131] heteronuclear dipolar scheme was applied to remove the ^{1}H-^{27}Al dipolar couplings [99].

3.2.5 Computation

Density functional theory (DFT) was used in all the quantum-chemical calculations using Gaussian 03 [109]. The DFT method used here is based on hybrid B3LYP functional.

The geometry optimisation of Alq_3 (both the facial and the meridional isomer) was done using 6-31G(d) basis set for all the atoms. The gas phase geometry optimised structure was used to calculate the electric field gradients (EFG). The EFG calculation was done using DFT with B3LYP functional. 6-31G(d) basis functions for C, H atoms and 6-311+G(3df) basis set for Al, N and O atoms were taken during the calculation. The more diffused basis sets were used for Al, N, and O due to our interest in the quadrupolar parameters at the Al center of Alq_3. The calculated values are given in Table 3.3. In organic powder/thin-film samples the organic molecule can be considered as solvated by the molecules of its own type. Hence, it is more realistic to take solid "solvation" into account whilst doing the EFG calculation for the molecules in thin films. For this, the isodensity polarisable continuum model (IPCM) provides an efficient way to consider the solvent effect as it defines the molecular cavity as a contour surface of constant electron probability density of the molecule [110]. This method has as its basis Onsager reaction field model [111]. In Onsager model the solvent is simply a continuous unstructured dielectric with a given dielectric constant surrounding a solute embedded in spherical cavity. This model was improved in polarizable continuum model (PCM) [112] where the solute cavity was constructed by a set of overlapping spheres where the spheres can be placed on individual atoms of the solute molecule and a more realistic cavity shape can be generated. The model was further improved in IPCM where a cavity can be defined based upon an isosurface of the total electron density. The shape of the cavity is then derived uniquely from the electronic environment which is surrounded by a continuum dielectric medium.

The isotropic polarisability (α) and molar volume (M/ ρ) of meridional and facial isomers were estimated from their corresponding geometry optimized structures obtained using the DFT method (B3LYP/6-31G (d)). The values of isotropic polarisability and molar volume were used to theoretically determine the values of dielectric constants, ε, for facial and meridional isomers using Clausius-Massoti equation [113]:

$$\frac{\varepsilon - 1}{\varepsilon + 2} = 4\pi\rho N_A \alpha / 3M$$

Our theoretical calculation of dielectric constants, ε, for facial and meridional isomers came out to be 2.62 and 2.69 respectively. The N_A in the above equation represents the Avogadro number.

The experimentally determined value of ε for thin film, which predominantly contains the meridional isomer, was found to be 3.0±0.3 [114]. As the theoretically predicted values of ε for both the isomers were nearly the same, the experimentally determined value of ε for thin film was used in the IPCM calculation for both the isomers. The levels of basis functions were the same for both the gas phase and the solid solvated phase.

3.3 NMR and XRD of Isomeric Forms of Alq$_3$

Figure 3.4 a shows the comparison between the experimental 1D spectra of the α-phase and 3.4 b shows the δ-phase of Alq$_3$ with the theoretical line generated using the DMFIT program which gave the quadrupolar coupling constant (χ) in MHz, the asymmetry parameter (η_Q), and the average value of isotropic shift which is a combination of both the isotropic chemical shift (δ_{iso}) and the isotropic quadrupolar shift (ν_Q^{iso}). The isotropic chemical shift δ_{cs} in ppm for p-quantum coherence can be evaluated by [97],

$$\delta(p) = -[\delta_{cs}p + \nu_Q^{iso}(p)/\nu_0]$$

where ν_Q^{iso} is isotropic qudrupolar shift, the expression of which is given in Ref. [19] and ν_0 is the Larmor frequency of the nuclei.

The quadrupolar parameters obtained from the 1D spectra (Table 3.1) conclusively prove that Al^{+3} ion is situated in an axially symmetric environment in the δ-phase whilst it is in a non-axially symmetric environment in the α-phase of Alq$_3$. (A low asymmetry
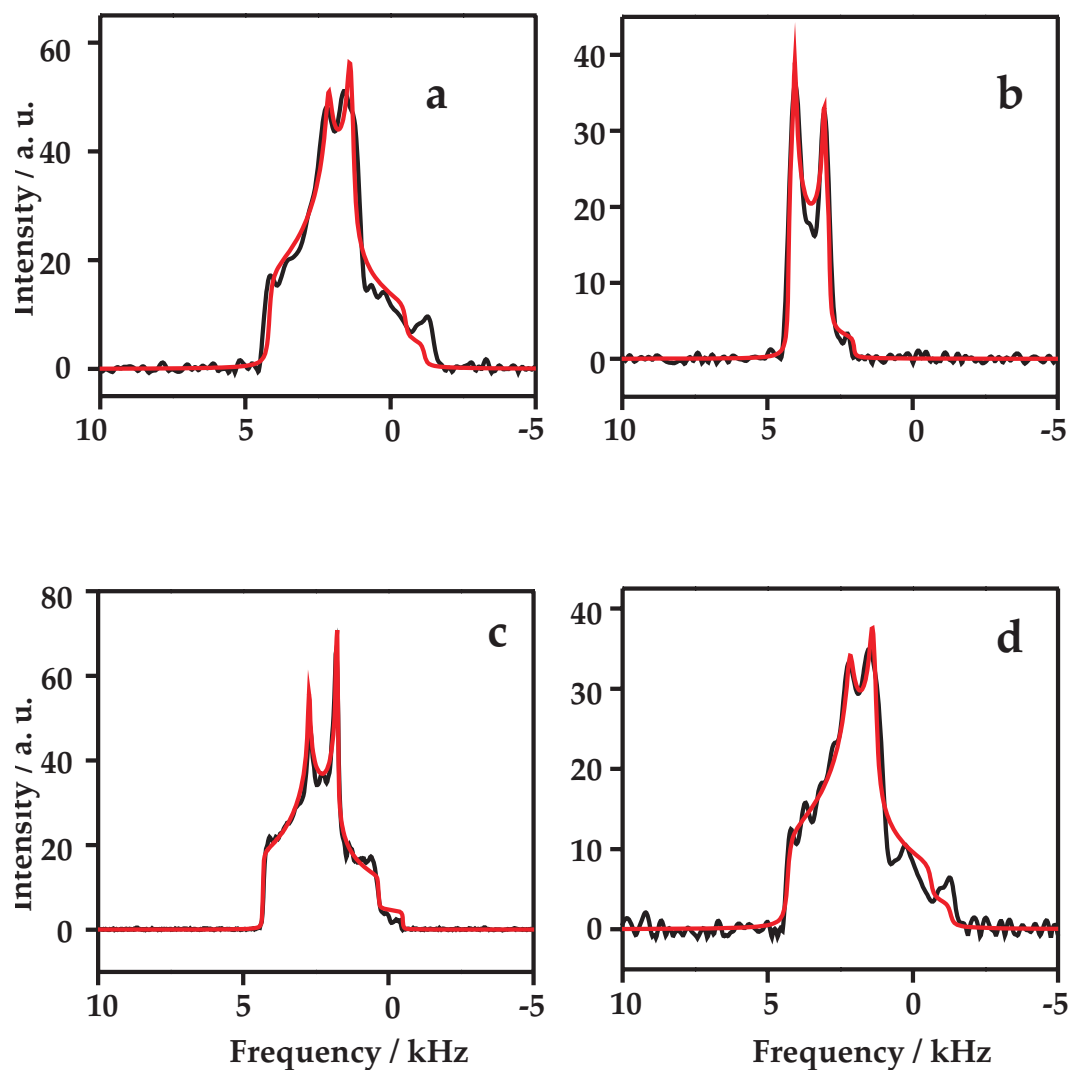
Figure 3.6: 1D ^{27}Al spectra of different modifications of Alq$_3$ under MAS. Experimental data (black) and fitted spectra (red) of (a) α-Alq$_3$, (b) δ-Alq$_3$, (c) solvated Alq$_3$, and (d) solvated Alq$_3$ after the removal of ethyl alcohol.

value generally signifies axial symmetry and a high asymmetry value denotes otherwise.) This agrees well with the previously reported results [92,93,103]. Figs. 3.4 c and d show the 1D spectrum of solvated Alq$_3$ before and after removal of the ethanol respectively along with the fitted lines. The 1D spectra of the α-phase of Alq$_3$, the δ-phase of Alq$_3$, and the solvated Alq$_3$ have distinctly different second-order quadrupolar broadened line shapes. The quadrupolar parameters obtained using the DMFIT program also show significant difference between the α-phase and the solvated Alq$_3$, which clearly suggests that the introduction of an ethanol molecule inside the Alq$_3$ matrix changes the local environment around Al^{+3} in the centre. Further, the line shape of the apohost Alq$_3$ (i.e, after the removal of ethanol from the solvated phase) has similar features to that of the α-phase of Alq$_3$ which is also evident from their nearly similar quadrupolar parameters (Table 3.1). The uncertainties in the values of χ, η_Q, and δ_{iso} were estimated by visual comparison of experimental and modelled spectra by employing small changes in the parameters and observing the matching of modelled spectra with the experimental ones.

Table 3.1: ^{27}Al quadrupolar parameters obtained from 1D MAS experiments using the DMFIT program.

Isomer	δ_{CS} (ppm)	η_Q	C$_q$/MHz
α- Alq$_3$	55.4±1.0	0.80±0.04	7.0±0.1
δ- Alq$_3$	43.6±1.0	0.18±0.03	4.9±0.1
Solvated Alq$_3$	50.5±1.0	0.62±0.04	6.4±0.1
Solvated Alq$_3$ after removal of ethanol	55.1±2.0	0.85±0.05	6.5±0.3

Figs. 3.5, 3.6, 3.7, and 3.8 show the 2D 3QMAS spectrum of the α phase, the δ phase, and the solvated phase before and after the removal of ethanol respectively of Alq$_3$. Sidebands appear along the F$_1$ dimension of the 2D spectra as the t_1 increments were not synchronised with the MAS rotor period. The isotropic spectrum is obtained from a projection on to F$_1$ which in all cases consists of only a single resonance. This

indicates that all the phases studied here have ^{27}Al in an unique crystallographic site. The cross section extracted along the ridge line shape parallel to the F$_2$ axis was fitted using the DMFIT program. From the fit the quadrupolar parameters were extracted and are given in Table 3.2. Figure 3.9 shows a comparison of the 2D MQMAS experimental anisotropic slice with the theoretical line generated using the DMFIT program. Since the DMFIT program gives the model spectrum of a site under ideal excitation, there will be some difference in the line shapes of the model and the experimental spectra, nevertheless the procedure for the model calculation is quite robust and gives fairly accurate results [135].
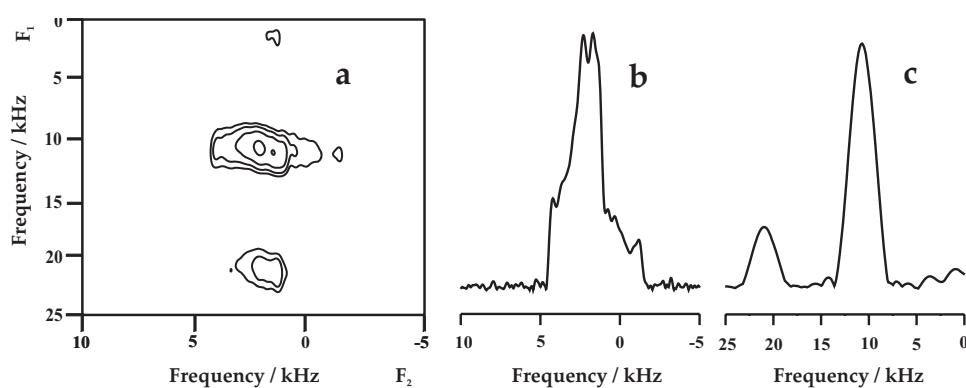
Figure 3.7: (a) 2D 3QMAS spectra of meridional Alq$_3$ (α-phase). The optimised excitation pulse and conversion pulse lengths were 3.8 μs and 1.8 μs. A total of 64 t$_1$ increments was taken with 10 μs of dwell time with 288 transients per increment. The recycling delay was 1 s. Total experiment time was 5 hours. (b) The anisotropic slice along the direction parallel to the F$_2$ dimension. (c) The isotropic projection along the F$_1$ dimension.

The quadrupolar parameters in Table 3.1 and Table 3.2 indicate that the α phase of Alq$_3$ contains only the meridional isomer as reported from the XRD study [85] and the δ phase of Alq$_3$ is composed of purely facial isomer as reported from the XRD study [87].

From Figs. 3.7 and 3.8, it can be observed that the isotropic projection for solvated Alq$_3$ is much narrower compared to the α-phase, the δ phase, and the solvated Alq$_3$
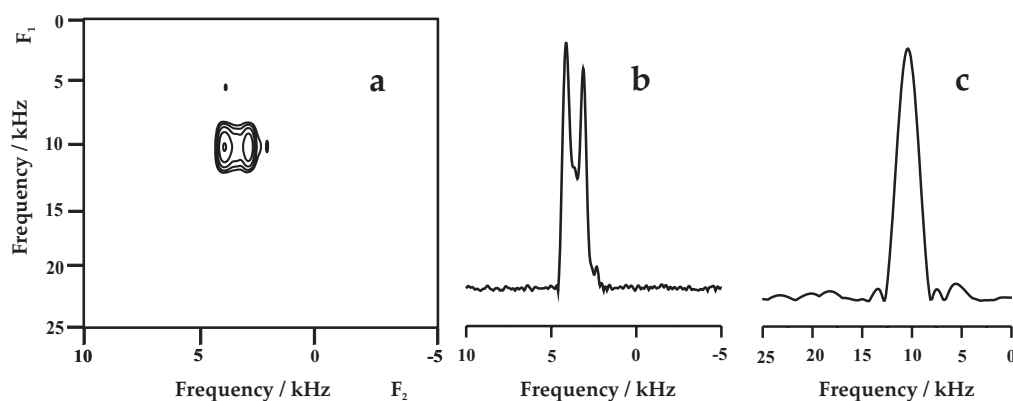
Figure 3.8: (a) 2D 3QMAS spectra of facial Alq$_3$ (δ-phase). The optimised excitation pulse and conversion pulse lengths were 4.4 μs and 1.9 μs. Rest of the experimental parameters are as in Figure 3. (b) The anisotropic slice along the direction parallel to the F$_2$ dimension. (c) The isotropic projection along the F$_1$ dimension.

from which ethanol was removed. It is well known that chemical and/or rotational exchange processes can influence the powder patterns of half-integer spin quadrupolar nuclei [115]. In general, the higher the rate and symmetry of the exchange process the narrower will be the line width. Hence, the reason for the narrowing down of isotropic projection of solvated Alq$_3$ could be due to the high mobility of the quinoline ligands between chemically equivalent orientations around the ^{27}Al site due to the introduction of ethanol into the crystal structure. Also it was observed that the shape of the cross section extracted along the F$_2$ dimension of the solvated Alq$_3$ is completely different from that of the α-phase of Alq$_3$ which was earlier indicated by their 1D MAS spectra as well. This also clearly indicates that the local electronic environment around the ^{27}Al centre undergoes significant change upon the introduction of ethanol into the matrix. Similar results were reported by Brinkmann *et al.* [85] where they showed that the unit crystal structure of the α-phase (triclinic) is different from that of a solvated phase of the form Alq$_3$(C$_6$H$_5$Cl)$_{1/2}$ (monoclinic). On the other hand the fluorescence emission spectra (Fig. 3.1) interestingly show practically no difference between the α-form (meridional)

of Alq$_3$ and the solvated Alq$_3$ containing ethyl alcohol. It shows fluorescence in Alq$_3$ is determined at molecular level and hardly influenced by molecular packing.
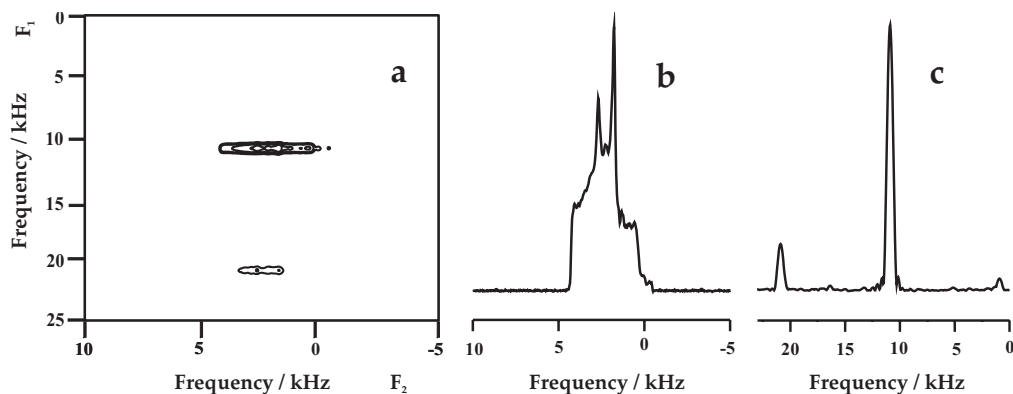
Figure 3.9: (a) 2D 3QMAS spectra of solvated Alq$_3$ (containing ethanol). Optimised excitation and conversion pulse lengths were 4.6 μs and 2.5 μs. A total of 192 t$_1$ increments was taken with 8 μs of dwell time with 96 transients per increment. The recycling dealy was 1 s. Total experiment time was 5 hours 18 mins. (b) The anisotropic slice along the direction parallel to the F$_2$ dimension. (c) The isotropic projection along the F$_1$ dimension.

It was further observed that the shape of the anisotropic slice of the apohost Alq$_3$ has remarkable resemblance to that of the α-phase. However, the isotropic projection is broader in the apohost form compared to the later. In a recent study on the polymorphism of a hexa-substituted benzene derivative, Hexakis (4-cyanophenyloxy) benzene, it was suggested that one can get four different polymorphic forms of the above mentioned compound when crystallising it from melt [116]. It can be argued qualitatively that removal of ethanol from the solvated Alq$_3$ is akin to the process of crystallising from melt, as the number of ethanol molecules existing per unit Alq$_3$ to solvate it is very small. Therefore it is possible that more than one polymorph may appear from the recrystallisation process giving rise to a distribution of NMR parameters resulting in the broadening of the ridges in the 3QMAS experiments.
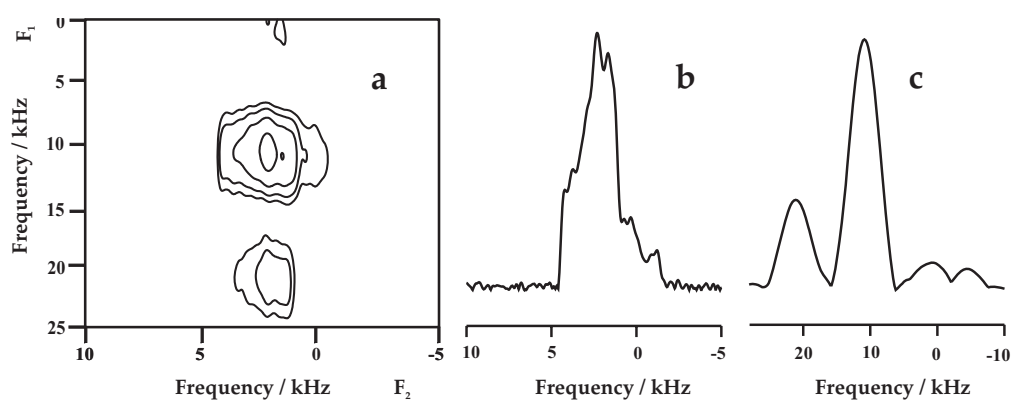
Figure 3.10: (a) 2D 3QMAS spectra of solvated Alq$_3$ after the removal of ethanol. Optimised excitation and conversion pulse lengths were 3.8 μs and 1.8 μs. A total of 60 t$_1$ increments was taken with 5 μs of dwell time with 576 transients per increment. The recycling dealy was 1s. Total experiment time was 9 hours 42 mins. (b) The anisotropic slice along the direction parallel to the F$_2$ dimension. (c) The isotropic projection along the F$_1$ dimension.

Table 3.2: ^{27}Al quadrupolar parameters obtained from 2D MQMAS experiments using the DMFIT program.

Isomer	δ_{CS}(ppm)	η_Q	C$_q$/MHz
α- Alq$_3$	54.7±1.0	0.85±0.04	6.9±0.1
δ- Alq$_3$	43.1±1.0	0.15±0.03	5.1±0.1
Solvated Alq$_3$	50.4±1.0	0.60±0.04	6.4±0.1
Solvated Alq$_3$ after removal of ethanol	55.0±2.0	0.81±0.04	6.9±0.3
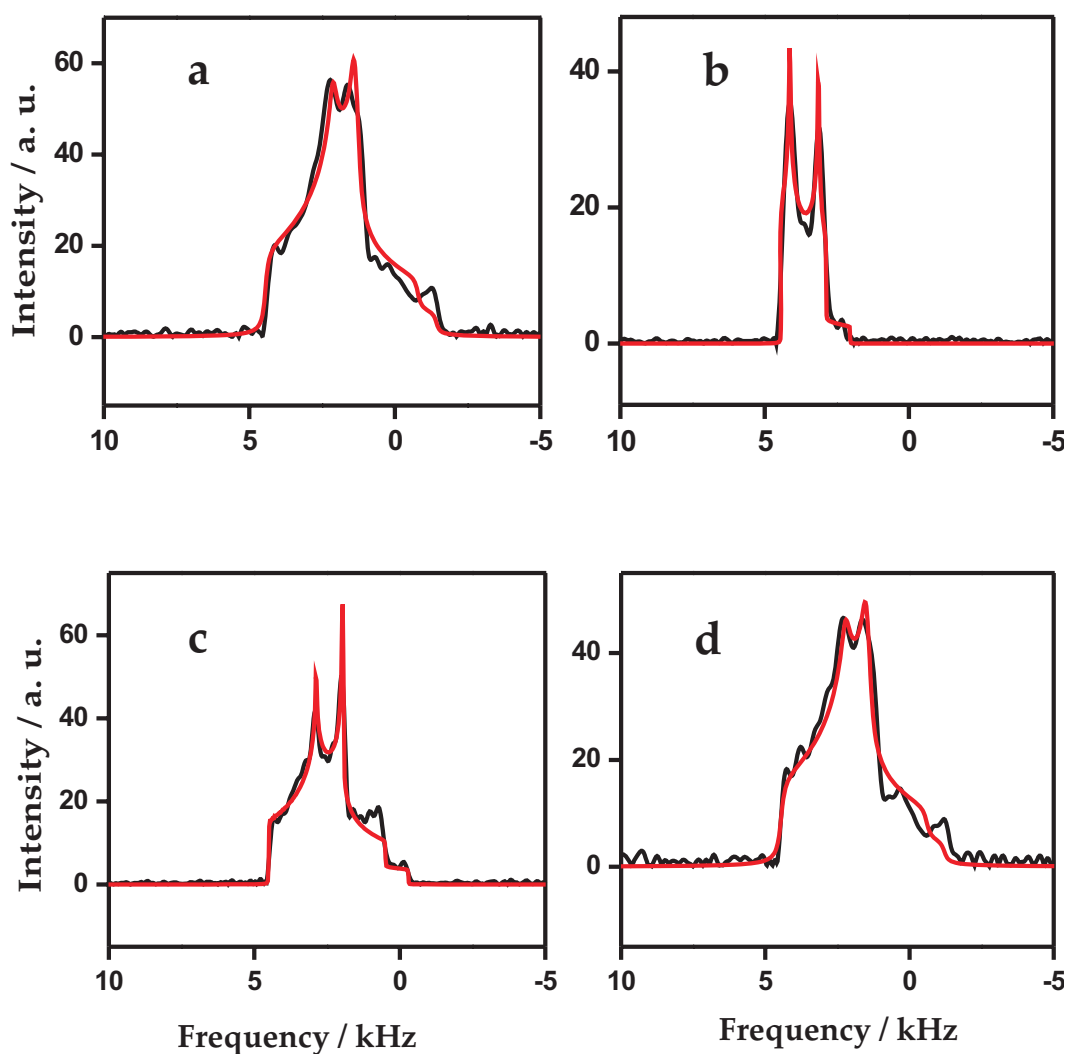
Figure 3.11: Comparison between 2D MQMAS (black) and fitted (red) line shapes for (a) meridional (α-phase), (b) facial (δ-phase), (c) solvated Alq$_3$ containing ethanol, and (d) after the removal of ethanol from the solvated Alq$_3$.

The quadrupolar parameters obtained for the α-phase of Alq$_3$ and the apohost Alq$_3$ are similar to each other indicating a similar environment around ^{27}Al in the two forms. Similar observations were also made from the XRD analysis, Figure 3.2, where the solvated form of Alq$_3$ containing ethanol has distinctly different feature from that of the α-phase. However, when the ethanol was removed from the solvated phase it gave XRD feature similar to that of the α-phase.

Figure 3.3 shows the data from the thermo gravimetric analysis of the solvated phase indicating a mass loss of 9.4 % at 140$^{\rm o}$C which corresponds to loss of one molecule of ethanol from Alq$_3$(C$_2$H$_5$OH)$_1$. It should be noted that Mq$_3$ where M is a trivalent metal can host small molecules in its solvated phase [85]. The removal of ethanol at a temperature higher than its boiling point confirms its participation in the crystal lattice. Though ethanol is not chemically bonded to Alq$_3$ its presence within the lattice affects the electronic distribution around Al and as a result the quadrupolar parameters of the solvated phase are different from either the α or the δ phase.

3.4   Quantum-Chemical Calculation

Quantum-chemical calculations yield principal components of EFG tensor, q$_{ii}$, in atomic unit, with $|{\rm q}_{zz}| \geq |{\rm q}_{yy}| \geq |{\rm q}_{xx}|$. The calculated q$_{ii}$ values were used to obtain the quadrupolar parameters manually [100],

$$\chi = e^2 Q q_{zz}/h$$

$$\eta_Q = | (q_{yy} - q_{xx})/q_{zz} |, 0 \leq \eta_Q \leq 1$$

where Q is the quadrupolar moment of ^{27}Al nuclei. The atomic Q(^{27}Al) value is 14.66×10^{-30}m^2 [117]. The calculated values of quadrupolar parameters are tabulated in Table 3.3.

DFT calculation of EFG principal values were done for isolated Alq$_3$ molecule. The asymmetry parameter η_Q obtained for the α-form was 0.77 while η_Q for the δ-phase of Alq$_3$ came to be 0.03. Previously Kaji *et al.* [103] also did similar kind of DFT calculations

where they predicted that the η_Q values for the α-form and the γ form of Alq$_3$ are 0.72 and 0.0 respectively. They also reported that the DFT calculation for the δ-phase yielded inconsistent results. Utz *et al.* [93] carried out a simple calculation for the estimation of EFG tensor on the basis of the assumption that the EFG tensor is determined by three point charges of -*e* at the oxygen sites. However, the values of η_Q predicted by this model (0.91 for meridional and 0.26 for facial) overshoot the experimental values obtained by us for both the isomers.

Here we make use of a model for DFT calculation where molecules are considered under the influence of a continuum dielectric medium (IPC model) which is a more realistic situation. Under this model it is observed that the theoretically predicted values (η_Q=0.81 for meridional and η_Q=0.10 for facial) show a relatively good agreement with the experimental values. In the case of solvated Alq$_3$, it was not possible to take a suitable model for the DFT calculation.

Table 3.3: ^{27}Al quadrupolar parameters obtained from DFT quantum chemical calculation under isolated molecule and isodensity polarisable continuum model (IPCM).

Model	Isomer	δ_{CS}(ppm)	η_Q	C$_q$/MHz
Isolated Molecule	α- Alq$_3$	-	0.77	7.7
	δ-Alq$_3$	-	0.03	7.0
IPCM	α-Alq$_3$	-	0.81	7.2
	δ-Alq$_3$	-	0.10	5.8

3.5   Temperature Dependent Study of Solvated Alq$_3$

Temperature dependent study was carried out on solvated Alq$_3$ in order to ascertain whether the different quadrupolar parameters exhibited by it is solely due to the presence of ethanol in the crystal matrix. The temperature was varied from room tempera-

ture to 140°C. The sample was packed in 4 mm rotor with a ceramic cap so that the cap does not melt at higher temperature and a steady spinning rate can be maintained. After that the temperature of the sample was increased from 25°C to 140°C at an increment of 10°C by using the bearing gas. The temperature of the bearing gas was controlled using a heater. At each temperature the ^{27}Al 1D MAS and 2D 3QMAS spectra was recorded. Here the results obtained at three three different temperature namely at 25°C, 80°C and at 140°C (Fig 3.10) are shown. It was observed that at 80°C which is the boiling point of ethanol the anisotropic lineshape of the 2D 3QMAS spectrum remains similar to that at room temperature. Clear change of lineshape occurs at a temperature of 140°C at which it is known that ethanol comes out of the crystal matrix. At this temperature the anisotropic line shape closely matches with that of the α form of Alq$_3$.

Here it is observed that as soon as ethanol is removed from the crystal matrix the anisotropic line shape of the solvated Alq$_3$ changes and the quadrupolar parameters become similar to that of the α form of Alq$_3$. Hence it can be concluded that the differential value in the quadrupolar parameters of the solvated Alq$_3$ is due to the presence of ethanol in the crystal matrix.

3.6 Conclusions

We have done 1D MAS and 2D MQMAS experiments to obtain high resolution spectra of meridional (α-phase) and facial (δ-phase) isomers of Alq$_3$. We have predicted the quadrupolar parameters from 1D MAS spectra using the DMFIT program. The 2D MQMAS experiments have shown that all the different modifications of Alq$_3$ have ^{27}Al in single unique crystallographic site which is evident from the single resonance lines along F$_1$ dimension. The quadrupolar parameters were also predicted using DFT calculation under isolated molecule assumption and also under the IPC model. It is shown that the theoretically calculated values of quadrupolar parameters improve and come close to the experimentally obtained values when calculations are done under the IPC
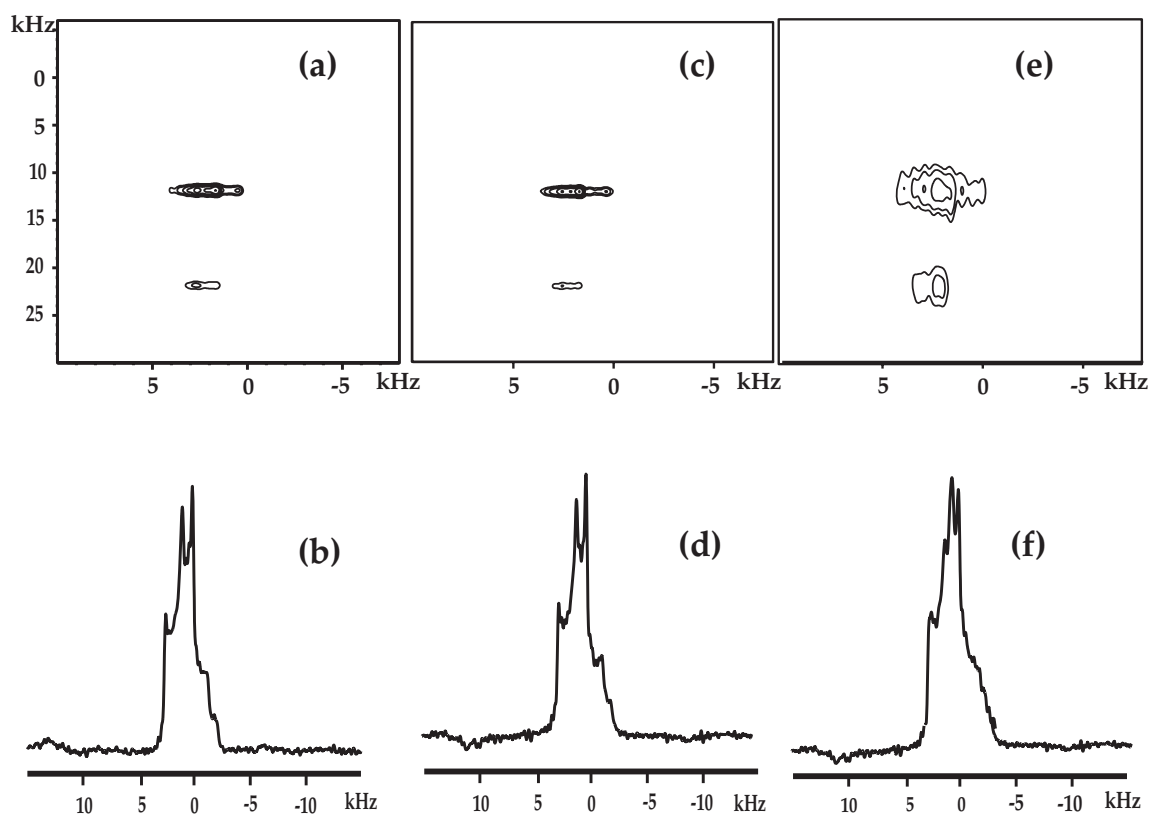
Figure 3.12: 2D 3QMAS spectra of solvated Alq$_3$ at different temperatures. (a) 2D 3QMAS spectrum at 25°C, (b) corresponding anisotropic projection, (c) 2D 3QMAS spectrum at 80°C, (d) corresponding anisotropic projection, (e) 2D 3QMAS spectrum at 140°C, (f) corresponding anisotropic projection.

model where an Alq$_3$ molecule is assumed to be solvated in a surrounding of similar Alq$_3$ molecules, which is the closest to the actual situation. We have also shown using solid-state NMR that the solvated phase of Alq$_3$ containing ethanol has structural difference from the α-phase of Alq$_3$ (containing meridional isomer). This was also confirmed by the XRD features, though the fluorescence spectra did not show any significant difference between them which again reaffirms the fact that fluorescence is determined at molecular level in Alq$_3$ and does not depend on crystal structure. Further it was shown that the isotropic projection of the solvated Alq$_3$ is much narrower than all the other polymorphs, which could be due to dynamic exchange processes. It was also shown using Thermo Gravimetric Analysis that there exists one ethanol molecule per Alq$_3$ in the solvated form. We have also shown that after the removal of ethanol the solvated Alq$_3$ becomes structurally similar to the α-phase of Alq$_3$. However, due to the possible introduction of more than one polymorph during re-crystallisation, broader ridges appear in the 2D 3QMAS spectrum of the apohost Alq$_3$. It can be seen that solid-state NMR can be used as an effective complementary tool to XRD for characterisation and structural elucidation. We have further demonstrated that more realistic approach to the calculation of EFG tensor would be to consider the solvation model (IPC model) where it is assumed that the molecule is placed inside a cavity surrounded by a continuum dielectric with dielectric constant of that of the molecule.

Chapter 4

Technique for Simultaneous Extraction of Dipolar and Quadrupolar Parameters

4.1 Introduction

Interest in ^{17}O (I=5/2) NMR has increased markedly in the last few years, particularly for characterizing amorphous inorganic oxide gels [119] and in the measurement of hydroxyl groups and water molecules in peptides and biological samples [120]. ^{17}O (I=5/2) NMR has also been applied to the study of zeolites [121], glasses [122], and membrane bound proteins [123]. The study of ^{1}H-^{17}O pairs is of particular interest for the investigation of hydrogen bonded systems since the ^{17}O quadrupolar interaction is sensitive to any perturbation in the local environment [124]. Knowledge of the local environment is extremely valuable and correlation of the quadrupole and dipole information of OH groups provides useful insight into structure. It was Linder *et al.* [125] who first explored the possibility of correlating the quadrupolar and dipolar tensor. Later the groups of Van Eck [126] and Levitt [127] have successfully demonstrated the correlation of dipolar and quadrupolar tensor.

Although the magnitude of ^{1}H-^{17}O dipolar coupling of directly bonded hydroxyl groups is quite large (of the order of 15 kHz) it is difficult to observe them directly be-

cause of the presence of large second order quadrupolar broadening of the order of several kHz associated with the central ^{17}O transition. The problem is further accentuated by the presence of ^{1}H- ^{1}H homo nuclear dipolar coupling. Earlier E. R. H. Van Eck and M. E. Smith [126] successfully resolved the ^{1}H-^{17}O dipolar coupling in static condition using Hartman-Hahn cross polarization [128] from ^{1}H to ^{17}O and Lee-Goldberg [129] decoupling in order to reduce the effect of ^{1}H- ^{1}H homo nuclear dipolar coupling. They also performed two dimensional ^{17}O quadrupole separated local field experiments in order to obtain the relative orientation of the ^{17}O quadrupole and OH dipole tensors.

Later Jacco D. van Beek *et al.* [127] showed that the ^{1}H-^{17}O dipolar coupling can be resolved in MAS condition by using spin echo sequence on ^{17}O and symmetry sequence [70] of the type RN_n^ν on proton to selectively reintroduce ^{1}H-^{17}O heteronuclear dipolar coupling while decoupling ^{1}H- ^{1}H homo nuclear dipolar coupling. They further predicted the relative orientation of dipolar and quadrupolar tensor using computer simulation.

However in all these studies one could only predict experimentally the dipolar information between ^{1}H-^{17}O pair. Simultaneous extraction of quadrupolar and dipolar information could not be possible with the schemes described above. One way to obtain both dipolar and quadrupolar information is to combine high-resolution sequences for the quadrupolar nuclei with the dipolar recoupling sequence in a 3D fashion such that one of the 2D planes of the 3D experiment will give high resolution spectrum for quadrupolar nuclei while the other 2D plane will provide corresponding quadrupolar-dipolar (QD) correlation spectrum.

In this chapter we show the results obtained when the symmetry sequence was combined with high-resolution sequences for the quadrupolar nuclei such as Satellite Transition Magic Angle Spin (STMAS) [19] and Multiple Quantum MAS (MQMAS) [130] sequences. Here we have also explored the possibility of performing three dimensional experiment by combining the STMAS and symmetry sequence to simultaneously obtain the dipolar and quadrupolar informations. From the 3D experiment we extracted the

quadrupolar informations and used them in the simulation of dipolar evolution. From the simulation of dipolar evolution the dipolar coupling constant and the bond length was estimated . Further we performed two dimensional numerical simulations with the previously estimated dipolar coupling constant to predict the relative orientation of dipolar tensor with respect to the quadrupolar tensor.

4.2   Experimental

^{17}O NMR experiments were performed on Bruker Avance 500 NMR spectrometer equipped with standard Bruker double-tuned MAS probes with 2.5 mm zirconia rotors. All experiments were carried out at 16 kHz MAS at room temperature. Symmetry sequence [70] of the type R18$_2^5$ was applied on ^{1}H with nutation frequency on proton, $\omega_{nut}^H = 72$ kHz. In all the experiments swept-frequency two pulse phase modulation (SW$_f$-TPPM) [131] heteronuclear dipolar scheme was applied to remove the ^{1}H-^{17}O dipolar couplings using an rf strength of 103 kHz.

The two dimensional (2D) quadrupolar-dipolar (QD) correlation experiments were done on Brucite, Mg(^{17}OH)$_2$ using spin echo, STMAS and MQMAS sequences on ^{17}O and R18$_2^5$ symmetry sequence on ^{1}H. The R18$_2^5$ sequence is made up of a repetition of two pulse element $180_{50}180_{-50}$ where the subscript expresses the pulse phases expressed in degrees where as the value "180" represent the pulse flip angle again expressed in degrees. The rf field strength needs to correspond to a nutation frequency of 4.5 times the MAS frequency. The 2D QD experiment using spin echo on ^{17}O was performed by taking 600 transients for each of the 30 t_1 increments. The interpulse delay was kept constant at a value corresponding to 15 rotor period (937.5 μs). The 2D QD experiments when performed using two pulse STMAS sequence on ^{17}O the interpulse delay was again kept constant at a value of 15 rotor period where as 256 number of transients was collected for 30 t_1 increments. For using two pulse 3QMAS scheme on ^{17}O a total of 4200 number of transients was taken for 16 t_1 increments. The interpulse delay was kept

constant at a value of 250 μs corresponding to 4 rotor period. All other experimental details are provided in the figure captions.

The 3D experiment was carried out to obtain both high resolution spectrum for quadrupolar nuclei as well as the quadrupolar-dipolar correlation spectrum. For this Double Quantum Filtered (DQF) -STMAS [132] scheme was applied on ^{17}O where as R18$_2^5$ symmetry sequence on ^1H. Here a total of 1024 number of transients was collected for each of 16 t_1 and 16 t_2 increments. The delay between excitation and the first soft π pulse was kept constant at 250 μs. All other relevant experimental details are given in the figure caption.

4.3   Simulation

Both one dimensional and two dimensional numerical simulations were carried out using SIMPSON [133] simulation program. All the experimental parameters such as the number of pulses, timings, and field strength were included in the simulation. For 2D simulation of the QD experiment the powder averaged spectra were calculated using 2000 crystal orientations following the REPULSION [134] scheme and 25 γ angles. For 1D dipolar evolution simulation 656 crystal orientations were considered with 10 γ angles for each orientations. The maximum time step over which the Hamiltonian was considered time independent was 0.5 μs. The SIMPSON simulation for calculating the dipolar evolution typically took 30 minutes where as a full 2D QD simulation took about 42 hours to complete in a HP XW 4400 workstation.

4.4   NMR of ^{17}O (I=5/2) in Mg(OH)$_2$

Fig 4.1(a) gives the general pulse schemes used for both 2D QD correlation experiments where an echo sequence is used on ^{17}O and R18$_2^5$ symmetry sequence on ^1H. The R18$_2^5$ symmetry sequence can be shown to recouple heronuclear dipolar coupling on symmetry

ground [70]. Though it should be noted that this sequence also reintroduces ^{1}H CSA but we have seen through simulations that at our magnetic filed neither the magnitude nor the orientation of CSA tensor has any significant effect on the QD correlation spectrum. The scheme depicted in Fig 4.1(a) was also used to plot the dipolar evolution curves as a function of varying length of the R block(Fig 4.6). Three different types of two pulse echo sequences were used for the QD experiments such as spin echo, STMAS and 3QMAS. The inter pulse delay in all the three schemes were kept constant at a value equal to an integral multiple of rotor period in order to refocus the isotropic chemical shift and chemical shift anisotropy of ^{17}O.

Fig 4.1(b) shows the 3D pulse schemes that was used to simultaneously obtain dipolar and quadrupolar informations. Here we have made use of DQF-STMAS scheme on ^{17}O in order to get high resolution spectrum of ^{17}O. The DQF-STMAS is superior to other STMAS schemes as it completely filters out all the unwanted diagonal and outer satellite peaks. Here as well the delay between the excitation pulse and the first soft π pulse was kept constant at an integral multiple of rotor period (4 rotor period) and in between R18$_2^5$ sequence was inserted. As the figure suggests the t$_1$ and t$_2$ delays are dependent on each other. In the 3D experiment, as the t$_1$ delay was incremented by certain amount t$_2$ was decremented by the same amount. The Fourier transform of F$_1$-F$_3$ plane produced the 2D Quadrupolar-Dipolar correlation spectrum where as the Fourier transform of F$_2$-F$_3$ plane generated the high resolution spectrum of ^{17}O from which all the quadrupolar parameters were extracted.

Quadrupolar dipolar correlation spectra under different pulse schemes are shown in Figs 4.2, 4.3, and 4.4. The unique shape of the correlation spectra reflects the fact that the dipole dipole coupling varies across the quadrupolar pattern. It is actually the secular dipole dipole coupling that has orientation dependence along with the dependence on the internuclear distance varies across the quadrupolar powder pattern. Hence the variation of the orientation of individual crystallites across the powder pattern gives rise
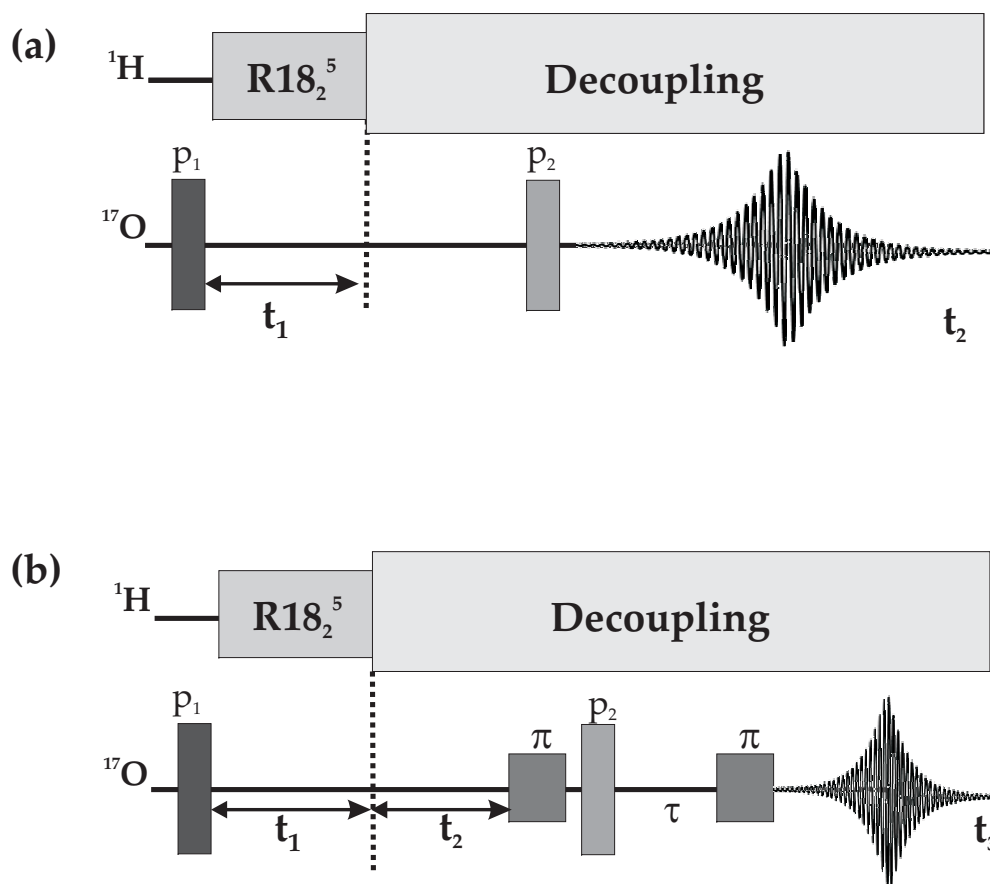
Figure 4.1: (a)Pulse sequence diagram for 2D QD correlation spectroscopy using $R18_2^5$ dipolar recoupling sequence on ^{1}Hand a two pulse echo sequence on ^{17}O. (b) The 3D scheme using high resolution DQF-STMAS on ^{17}O and $R18_2^5$ symmetry sequence on ^{1}H. In the both scheme p_1 and p_2 denotes the excitation and reconversion pulse length.

to the variation in the secular dipole dipole coupling resulting in the unique shape of the 2D QD correlation spectra. Fig 4.2(c) and (d), 4.3(c) and (d) show the projections along the dipolar (indirect) dimensions of right hand side singularity and left hand side singularity respectively of the quadrupolar powder pattern. The 3QMAS scheme could not effectively excite the whole powder pattern that is the reason why we believe that we get quadrupolar dipolar correlation for only the right hand side singularity. However as expected the splitting of the dipolar projection obtained using 3QMAS of the right hand side singularity is ~ 3 times the splitting obtained using spin echo and STMAS scheme. Similar observation was also made when the experimental evolution of both the singularities was plotted (Fig 4.6) under different pulse schemes.

The result obtained using the 3D pulse scheme depicted in Fig 4.1(b) is shown in Fig 4.5. From the Fourier transform of the F_1-F_3 plane the usual 2D QD correlation spectrum (Fig 4.5a) was obtained with the dipolar projection of the right hand side singularity (Fig 4.5c) and the left hand side singularity (Fig 4.5d). The high resolution spectrum of the ^{17}O nuclei was obtained by Fourier transforming the F_2-F_3 plane. From the anisotropic projection (Fig 4.5e) of the high resolution spectrum we estimated the value of the quadrupolar coupling constant, C_Q of the ^{17}O nuclei in Mg(^{17}OH)$_2$ using DMFIT [135] program to be 6.21 ± 0.03 MHz and asymmetry parameter $\eta = 0.0$. Further from the isotropic projection (Fig 4.5f) we obtained the isotropic chemical shift δ_{CS} = 18 ppm. It can be observed that the signal intensity of the QD correlation spectrum obtained using the 3D pulse scheme is lower than the QD correlation spectrum obtained using the two pulse STMAS scheme. The reason behind this we believe is the fact that in case of two pulse STMAS scheme contribution from all the satellite transitions and more importantly the central to central transition comes into play. However in DQF-STMAS the only contribution which is chosen is the contribution from the inner satellites that is also precisely why the DQF-STMAS scheme gives a better high resolution spectra of quadrupolar nuclei with out the presence of addition peaks coming from other transi-
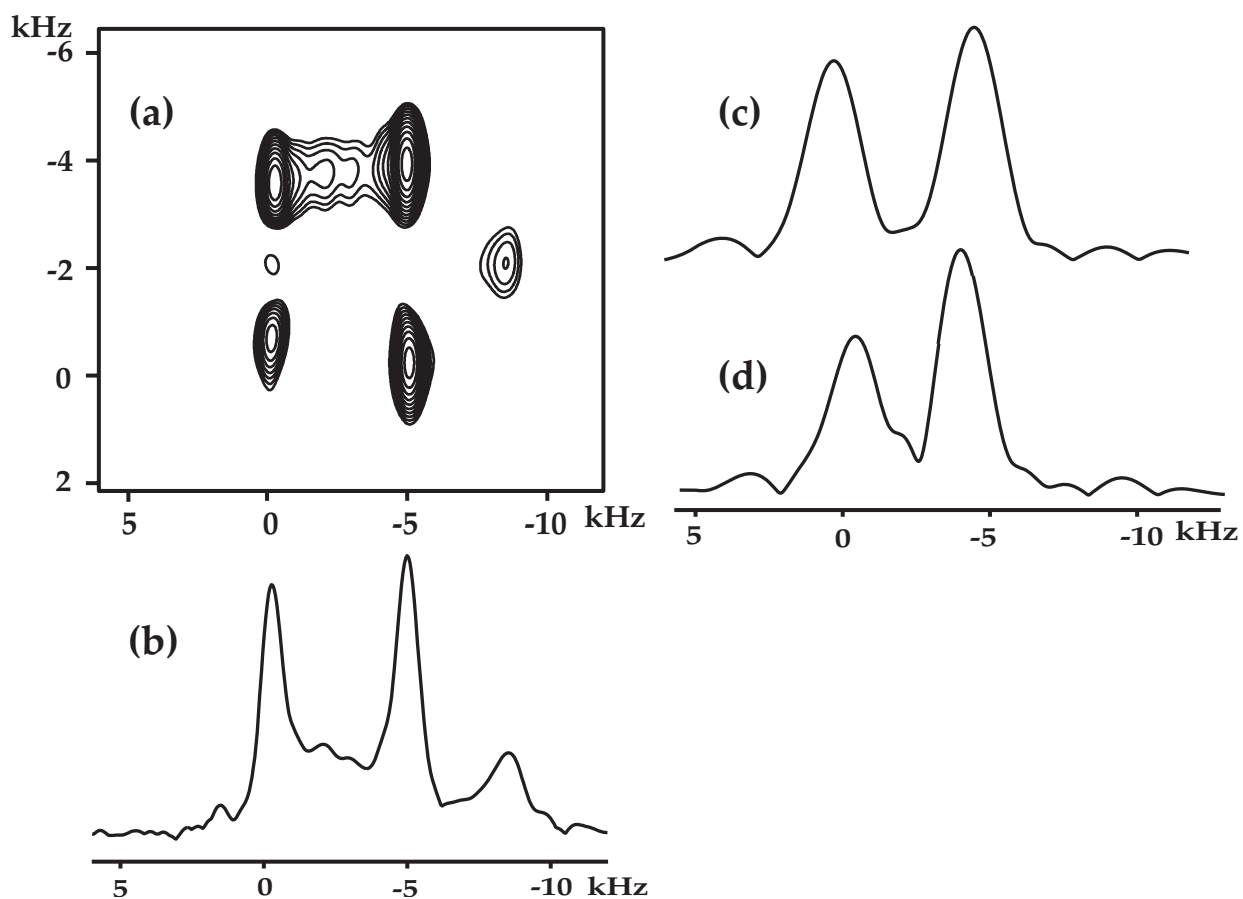
Figure 4.2: (a) 2D QD spectrum using spin echo on ^{17}O, (b) Projection along the direct (quadrupolar) dimension, (c) Projection along the indirect (dipolar) dimension of the right hand side singularity, (d) Projection along the indirect (dipolar) dimension of the left hand side singularity. The length of the 90° pulse was 5 μs. The relaxation delay was 2 s. The length of each t_1 increment was 27.77 μs corresponding to two pairs of R blocks.
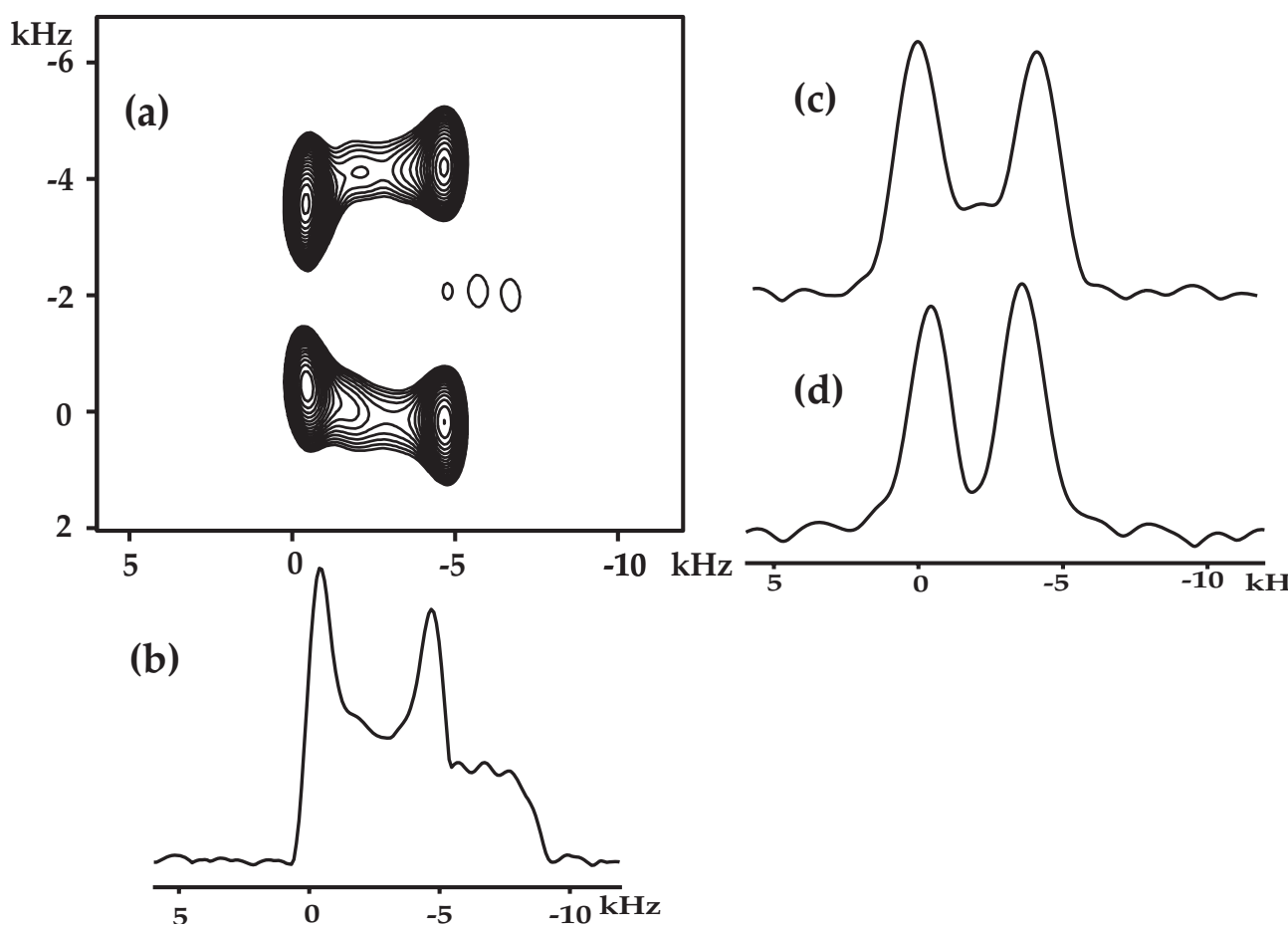
Figure 4.3: (a) 2D QD spectrum using two pulse STMAS on ^{17}O, (b) Projection along the direct (quadrupolar) dimension, (c) Projection along the indirect (dipolar) dimension of the right hand side singularity, (d) Projection along the indirect (dipolar) dimension of the left hand side singularity. The length of the excitation pulse was 2.1 μs and that of the reconversion pulse was 1.4 μs. The relaxation delay was 2 s. The length of each t_1 increment was 27.77 μs corresponding to two pairs of R blocks.
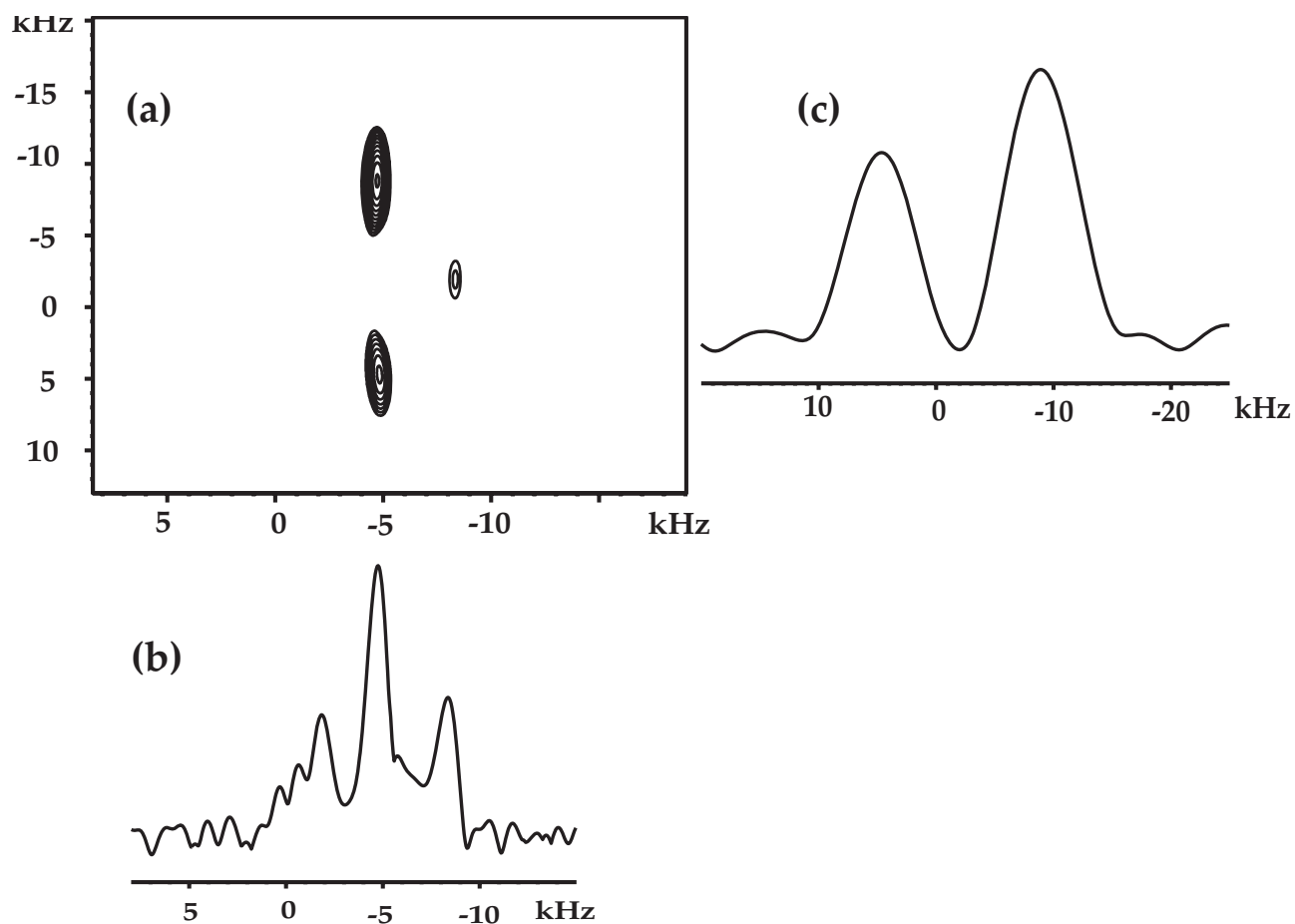
Figure 4.4: (a) 2D QD spectrum using two pulse 3QMAS on ^{17}O, (b) Projection along the direct (quadrupolar) dimension, (c) Projection along the indirect (dipolar) dimension of the right hand side singularity, (d) Projection along the indirect (dipolar) dimension of the left hand side singularity. The length of the excitation pulse was 5 μs and that of the reconversion pulse was 2.8 μs. The relaxation delay was 2 s. The length of each t_1 increment was 13.88 μs corresponding to a single pair of R block.

tions. Hence by applying a 3D pulse scheme such as Fig 4.1(b) one can simultaneously obtain both Quadrupolar Dipolar correlation spectra as well as the high resolution spectra of the quadrupolar nuclei concerned. This method will be more useful for substances with more than non equivalent quadrupolar sites. This is because this scheme can resolve all the quadrupolar sites in a system and in addition will give quadrupolar dipolar correlation of each of the sites.

Fig 4.6 shows the experimental dipolar evolution of both right hand side singularity and left hand side singularity of the quadrupolar powder pattern under different pulse schemes on ^{17}O. As expected the dipolar evolution of both the singularities under spin echo and STMAS are similar since essentially both the sequences are single quantum experiment. The dipolar evolution of right hand side singularity under 3QMAS scheme on the other hand shows 2.93 times faster dipolar evolution frequency which is expected as the spin system evolves under the recoupled dipolar coupling when the system is in triple quantum. The triple quantum excitation was not efficient enough to properly excite the whole powder pattern as a result only the evolution of the right hand side singularity can be observed.

4.5 Numerical Simulation

Fig. 4.7 shows the simulated dipolar evolution for both right hand side singularity and left hand side singularity compared with the experimental evolutions. It is quite evident that the simulated evolutions show good correspondence with the experimental evolutions for both the singularities. From the simulation we obtained the dipolar information in the form of secular part of direct dipole-dipole coupling represented as d. Now it is known that d depends on θ_{jk} [136], the instantaneous angle between the internuclear vector and the magnetic field. The secular dipole dipole coupling is given by,

$$d = b_{jk}\frac{1}{2}(3cos^2\theta_{jk} - 1)$$
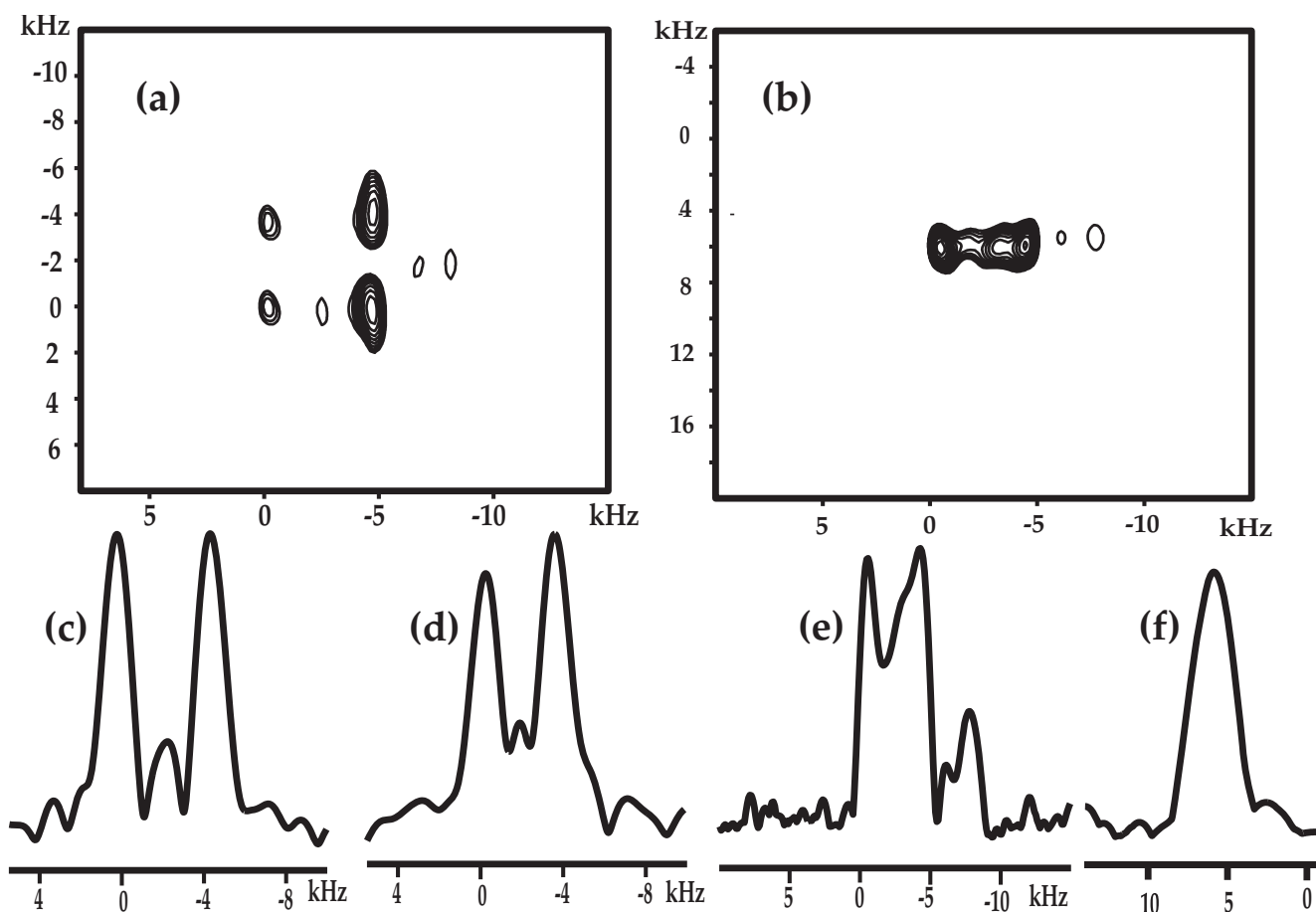
Figure 4.5: (a) 2D QD spectrum obtained by Fourier transforming F_1-F_3 plane, (b) Projection along the indirect (dipolar) dimension of the right hand side singularity from the 2D QD spectrum, (c) Projection along the indirect (dipolar) dimension of the left hand side singularity from the 2D QD spectrum, (d) High resolution 2D ^{17}O spectrum obtained by Fourier transforming F_2-F_3 plane,(e)The anisotropic slice taken parallel to the direct dimension of the 2D ^{17}O spectrum, (f) The high resolution projection along the isotropic dimension. The length of the excitation pulse was 2.1 μs and that of the reconversion pulse was 1.4 μs. The length of the soft π pulse was 15.7 μs. The relaxation delay was 2 s. The length of each t_1 increment was 27.77 μs corresponding to two pairs of R blocks. The length of each t_1 decrement was also equal to two pairs of R blocks.
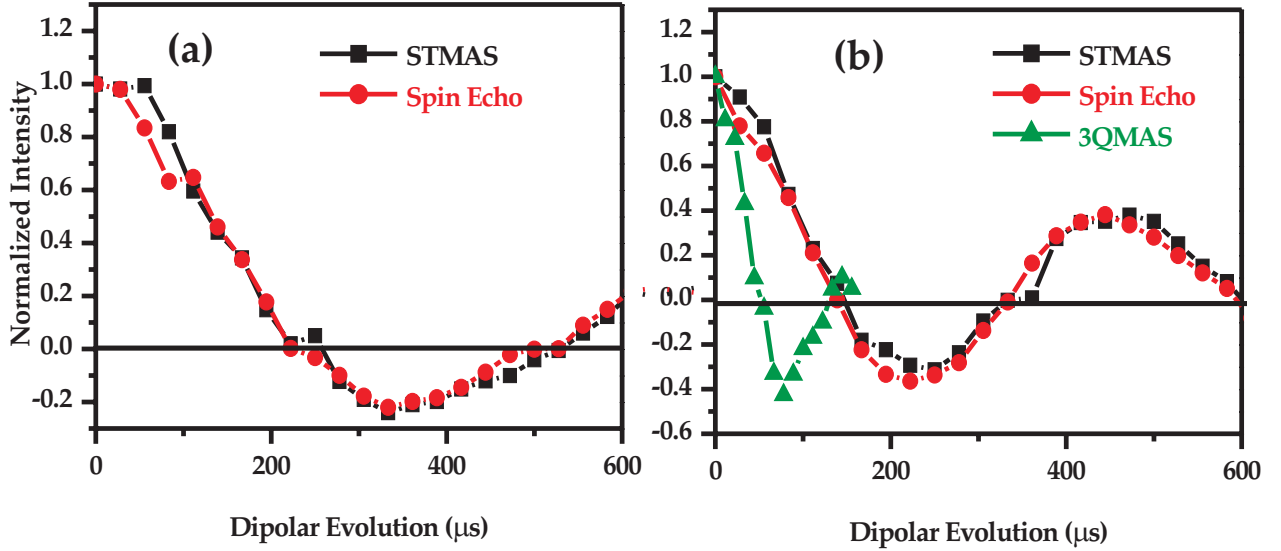
Figure 4.6: The experimental dipolar oscillations of (a) left hand side singularity, (b) right hand side singularity using different pulse schemes.

where the dipole dipole coupling constant is given by,

$$b_{jk} = -\frac{\mu_0}{4\pi} \frac{\gamma_j \gamma_k \hbar}{r_{jk}^3}$$

where r_{jk} is the internuclear distance. So it is evident from above the maximum possible value that secular dipole dipole coupling d can have is equal to the dipole coupling constant b_{jk} when θ_{jk} is equal to zero i.e, when the internuclear vector and magnetic field is collinear. It is observed from the 2D QD correlation spectra that the dipolar projections corresponding to the right hand side singularity shows maximum splitting where as it is minimum at left hand side singularity. This observation led us to believe that the secular dipole dipole coupling between ^{1}H-^{17}O pair in brucite has its maximum value along the right hand side singularity. The best fit between the simulated dipolar evolution and experimental simulation for the right hand side singularity was achieved for dipole dipole coupling of 15.6 ± 0.2 kHz. Since it is evident from the 2D quadrupolar-dipolar

experiments that the maximum value possible for the secular dipole dipole coupling was achieved for powder orientations correponding to the right hand side singularity of the quadrupolar powder pattern hence it can be concluded that the value of the dipole dipole coupling constant is 15.6 ± 0.2 kHz. Now the value of dipole coupling constant estimated by by Jacco D. van Beek *et al.* [127] was about 2 kHz less than the value estimated by us. The reasons for this discrepancy in the value could be the following. When we estimated the dipole coupling constant through simulation we used the values of quadrupolar parameters such as coupling constant and asymmetry parameter measured by us from the 3D experiment. However the quadrupolar coupling constant value measure by us (6.21 ± 0.03 MHz) was different than the value used by Jacco D. van Beek *et al.* (6.83 MHz). When we incorporated the value of quadrupolar coupling constant used by them in our simulation we estimated the value of dipole coupling constant to be 14.4 ± 0.2 kHz. But still this is about 1 kHz larger than the value predicted by them. However it should be noted that they estimated the value of dipole coupling constant through simulated 2D QD correlation experiment where as we have estimated the dipole coupling constant from the fitting of the experimental dipolar oscillation which is more sensitive to any small change in the value of dipolar coupling constant value than the simulation of 2D QD correlation plot. Hence we believe the value obtained by directly fitting the experimental dipolar oscillation one can more accurately predict the dipole dipole coupling constant. More over the dipole dipole coupling constant value of 15.6 ± 0.2 kHz corresponds to ^{1}H-^{17}O bond length of 101 ± 1 pico meter which is in very good agreement with the distance of 99.5 ± 0.8 pico meter predicted by neutron diffraction study [137] and a distance of 98 ± 2 pico meter that was found by combining proton NMR and x-ray data [138].

We further did a series of 2D numerical simulations by varying the relative orientation of dipolar coupling tensor with respect to the quadrupolar coupling tensor again using the quadrupolar parameters obtained from the 3D experiment to match the experimental
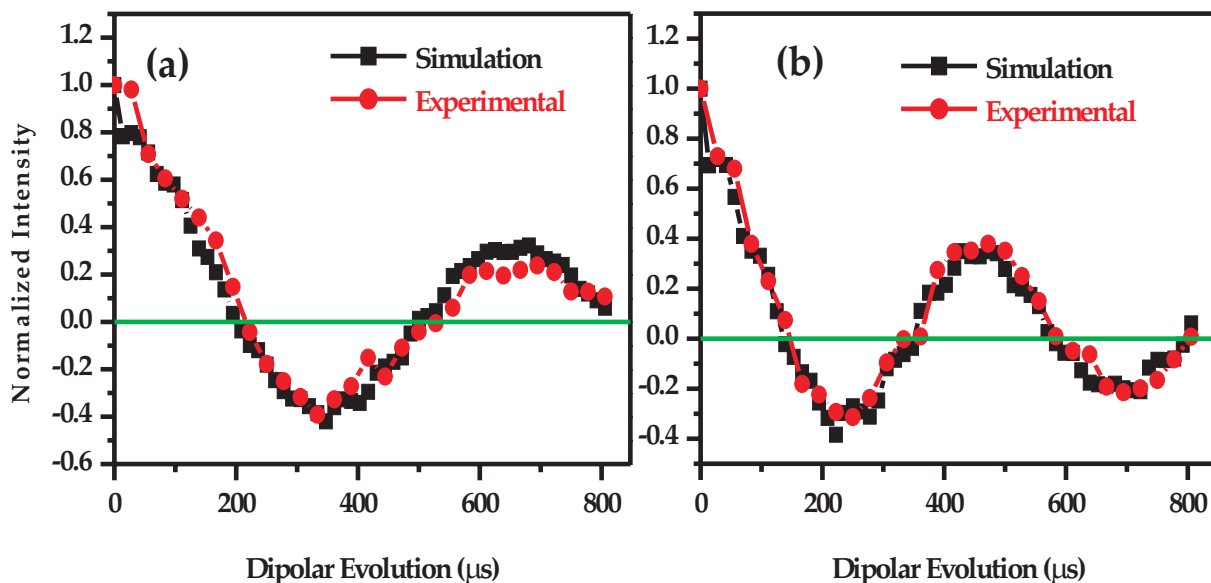
Figure 4.7: The experimental and simulated dipolar oscillations of (a) left hand side singularity, (b) right hand side singularity.

QD correlation spectrum. From the simulation it was concluded that the dipolar tensor and quadrupolar tensor in our system is coaxial which again matches with the previous predictions [127].

4.6 Conclusions

In this chapter we have discussed the possibility of doing two dimensional quadrupolar dipolar correlation experiments using different echo sequences such as spin echo, STMAS and MQMAS. We have further shown that high resolution NMR schemes for quadrupolar nuclei can be combined with the symmetry sequences in 3D fashion to simultaneously obtain dipolar and quadrupolar informations. This method will be of particular importance for materials with more than one quadrupolar sites since by this method one can get the dipolar informations of all the individual sites separately. From the experimental dipolar oscillations we predicted the value of dipolar coupling constant
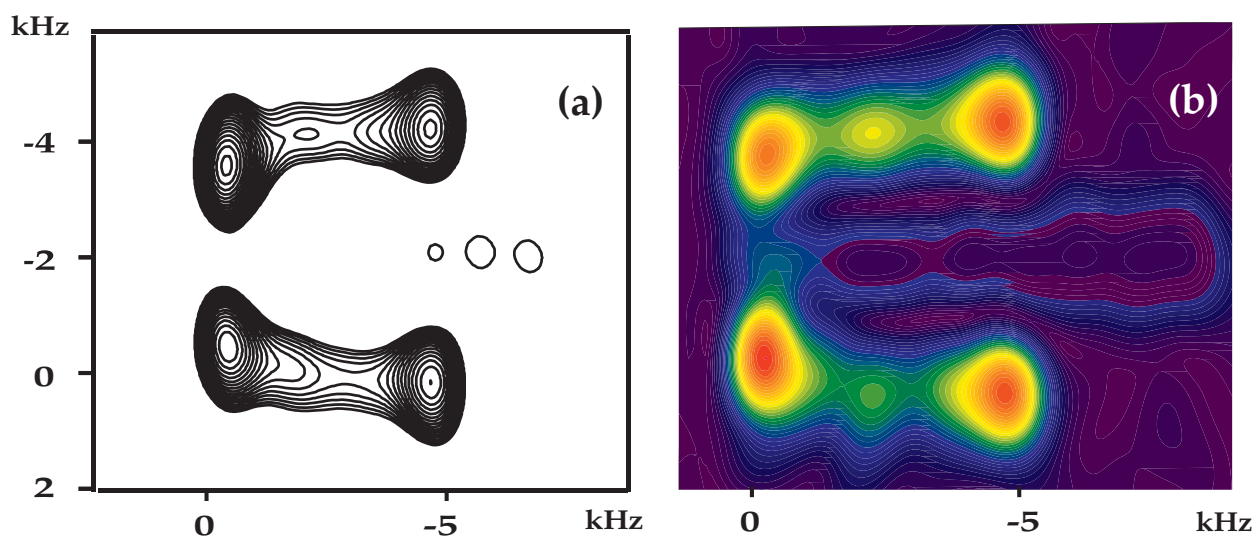
Figure 4.8: The experimental and simulated 2D QD correlation spectrum. (a) Experimental QD spectrum, (b) Simulated QD spectrum.

and the ^{1}H-^{17}O bond distance which shows close correspondence with the previously reported value using neutron diffraction. We have also done the simulation of two dimensional quadrupolar dipolar correlation experiment from which it is concluded that the dipolar tensor and quadrupolar tensor is coaxial in Brucite.

Chapter 5

Sensitivity Enhanced ^{29}Si Double-Quantum Dipolar Recoupling NMR Spectroscopy

5.1 Introduction

In the study of ordered silicate materials, such as the open framework zeolites [139,140] and mesoporous silica [141,142], elucidation of the framework structure is the key to the understanding of the unique catalytic properties exhibited by these materials [143–145]. However, structure determination of these materials by diffraction techniques is difficult since single crystals of adequate dimensions are usually not available. Powder X-ray diffraction (XRD) experiments can provide unit cell parameters and identify possible space groups. However, solving zeolite structures from powder XRD data alone is not straightforward. Solid-state NMR can provide structural information that is complementary to diffraction. Description of the framework structure has been made possible with two-dimensional (2D) ^{29}Si homo- and hetero-nuclear correlation experiments carried out under magic-angle spinning (MAS) [146–148].

2D method for obtaining ^{29}Si-^{29}Si correlation spectra that exploit double-quantum (2Q) through-bond (scalar) interactions have been reported. Pulse sequences such as INADEQUATE [149] was successfully utilized to map out the ^{29}Si-^{29}Si connectivity in zeolites [148]. Recently symmetry-based recoupling sequences [70], such as SR26$_4^{11}$ [150] which exploit the dipolar interaction between ^{29}Si spins at natural abundance, were shown to provide information about framework connectivity in zeolites [151]. The double-quantum (2Q) dipole-dipole recoupling achieved under MAS resolution serves to correlate the single-quantum (1Q) and 2Q frequencies of isolated Si-Si spin pairs and thus map the connectivity between various Si sites.

The study of ^{29}Si using solid-state NMR is hindered by the poor intrinsic sensitivity of ^{29}Si due to the low natural abundance and the low gyromagnetic ratio. Hence structural elucidation through 2Q-correlation spectra at ^{29}Si natural abundance is typically only possible in well-crystallised high-silica zeolites when the resonances in MAS spectra are narrow. However, this favourable situation is not met when MAS spectra are broadened by a distribution of isotropic chemical shifts, as would often occur in materials which lack long-range order or which contain surface defects (silanol groups). Such line broadening is even more severe in the case of functionalised mesoporous materials. Therefore, ^{29}Si observation is often beset with very poor detection sensitivity due to the disordered nature of the samples and this is further accentuated when the concentration of silicon species is small. The latter would occur, for example, in organo-functionalised silica where the degree of functionalisation is usually low (ca. 20%). Thus, in many cases of practical relevance, it is a prerequisite for the analysis to establish 2Q-recoupling experiments with enhanced ^{29}Si observation sensitivity.

Implementation of Carr-Purcell-Meiboom-Gill [51, 52] (CPMG) sequence proved to be highly successful as a means to enhance the sensitivity of second-order broadened quadrupolar nuclei in static [53–55], MAS [56–58], and MQ-MAS [59–61] experiments. Similarly, in our present case also the sensitivity problem can be alleviated to a great ex-

tent by implementing a CPMG train of π pulses within the acquisition period of the dipolar recoupling experiment. The multiple-pulse CPMG sequence refocuses the inhomogeneously broadened MAS spectral lines and entails the repeated generation spin echoes, which can be co-added to enhance the signal intensity. As done in ^{1}H-^{29}Si heteronuclear and the J coupling based ^{29}Si-^{29}Si homonuclear correlation experiments [148], the CPMG implementation in dipolar recoupling sequences would provide the desired sensitivity enhancement to aid the structural characterisation effort in disordered solids.
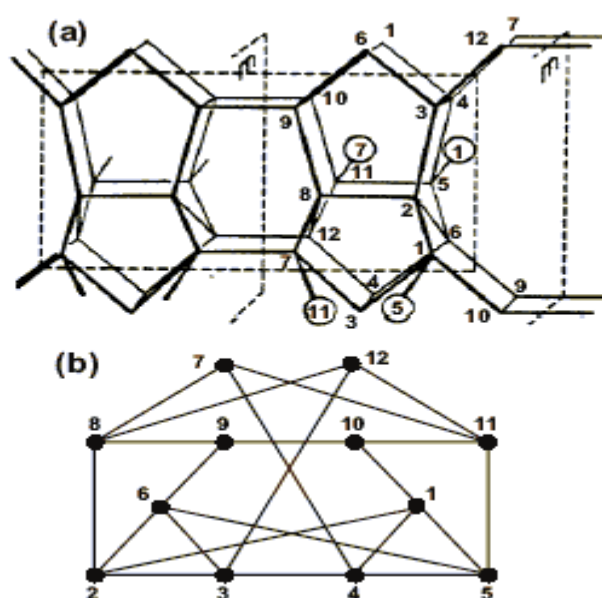
Figure 5.1: (a)Three dimensional structure of zeolite ZSM-5 showing the inter connectivity between different ^{29}Si T-sites (Tetrahedral sites) in orthorhombic as-synthesized form, after Ref. [162], (b) A connectivity map of different ^{29}Si sites.

In this chapter we discuss about ^{29}Si double-quantum dipolar recoupled 1Q-2Q correlation experiment to establish ^{29}Si-^{29}Si homonuclear correlations within the zeolite ZSM-5 framework using the POST-C7 [152] recoupling sequence. It will be further shown that considerable enhancement in the signal intensity can be achieved by implementing CPMG train of π pulses at the ^{29}Si Larmor frequency into a POST-C7 dipolar recoupling sequence. The sensitivity gain obtained and the framework connectivity established in

the catalytically important molecular sieve ZSM-5 are demonstrated. Further the comparison between the 2D 1Q-2Q correlation spectra obtained using INADEQUATE [149] and POST-C7 sequences will be shown.

5.2   Pulse Sequence

We have made use of symmetry based double quantum dipolar recoupling sequences of the types POST-C7 and supercycled $R26_4^{11}$. We then compared our result with the j-coupling based INADEQUATE sequence.

5.2.1   POST-C7

This method has been applied to recover through-space nuclear dipole-dipole couplings [153]. The double-quantum (2Q) C7 method is a particularly efficient method for dipolar recovery in powders. Its efficiency derives partly from the fact that the magnitude of the recoupled Hamiltonian to a first-order approximation is only sensitive to one of the three orientational angles (γ) relating a molecule-fixed axis system to a rotor fixed frame. 2Q-filtering efficiencies exceeding 50 % have been reported for this scheme [69]. The original C7 ($C7_2^1$) sequence exploited a basic element of two pulses of flip angle 2π, with opposite phase, i.e. $(2\pi)_\phi (2\pi)_{\phi+\pi}$. The basic element is repeated 7 times each time advancing the rf phase ϕ within the element by $2\pi/7$. The sequence is timed so that the full cycle of seven steps is completed in exactly two sample rotation periods. The robustness of C7 with respect to chemical shift offsets and rf inhomogeneity can be significantly improved by permutation of pulses within the basic sequence element, leading to the new element = $(\pi/2)_\phi (2\pi)_{\phi+\pi} (3\pi/2)_\phi$ known as Permutationally Offset Stabilized C7, POST-C7. This simple modification gives a much more broadbanded dipolar recoupling effect, and in some cases an increased 2Q filtering efficiency by virtue of the enhanced rf inhomogeneity compensation. The behaviour of the homo and heteronu-

clear dipolar coupling terms under $C7_2^1$ sequence can be much easily described by space spin selection diagram. The branching lines in these diagrams show the possible values of mn - μv for the particular class of spin interaction, split up into the "space" part mn and the "spin" part μv. The number of branches depends on the type of spin interaction, while the spacing between the branches depends on the symmetry numbers n and v. The right hand side of each diagram shows a barrier containing holes spaced by the symmetry number N. Those pathways that are blocked by the barrier represent values of mn - μv represent components that are symmetry-forbidden. Those pathways that pass through the holes in the barrier represent values of mn - μv which are symmetry-allowed.
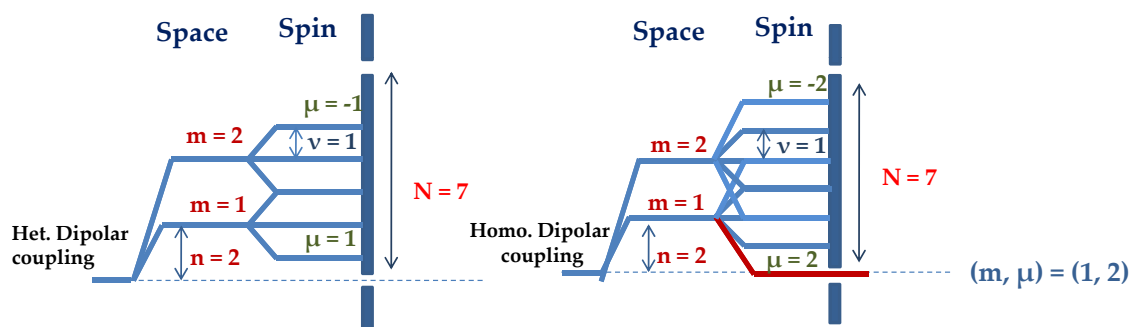
Figure 5.2: Space spin selection diagram for POST-C7 homonuclear recoupling sequence.

5.2.2 SR26$_4^{11}$

In the context of homonuclear dipolar recoupling, sequences such as C7 and POST-C7 provide high double-quantum signal filtering efficiency, and make it possible to determine bond distances with picometer accuracy [153]. These sequences have the property

of γ-encoding, which implies that to first-order, the recoupled double-quantum Hamiltonian is purely phase modulated by the third Euler angle describing the orientation of the molecules with respect to the rotating sample holder. γ-Encoding leads to high double-quantum filtering efficiencies and large dipolar oscillations for powder samples [154]. However, γ-encoded double-quantum recoupling sequences have not proven so suitable for the determination of longer distances between nuclei with relatively large chemical shift anisotropies. The supercycled $R26_4^{11}$ method combines the favourable features of the symmetry based sequences with the robustness of the non γ-encoded sequences. The pulse sequence can be described as,

$$SR26 = [R26_4^{11}R26_4^{-11}]_0[R26_4^{-11}R26_4^{11}]_\pi$$

where the symbol RN_n^v describes a symmetry based pulse sequence described by,

$$RN_n^v = [(R^0)_{+\pi v/N}(R^0)'_{-\pi v/N}]^{N/2}$$

where R^0 is a composite π pulse that rotates the resonant spin by $\pm\pi$ about the x-axis and $R^{0'}$ is derived from R^0 by changing the sign of all phases. The subscript determines the overall rf phase shifts of the R-elements, and the superscript determines the number of repetitions of the bracketed elements. It was shown that by applying a super cycle of the form $[R26_4^{11}R26_4^{-11}]$, the influence of the higher-order terms generated by large CSA can be removed from both first- and second-order average Hamiltonians [158]. Again the behaviour of homo and heteronuclear dipolar coupling under $R26_4^{11}$ sequence can be described with the help of space spin selection diagram.

5.2.3   INADEQUATE

The pulse sequence INADEQUATE was designed by Ad Bax *et al.* in 1980. The acronym stands for "Incredible Natural Abundance Double Quantum Technique". This pulse se-
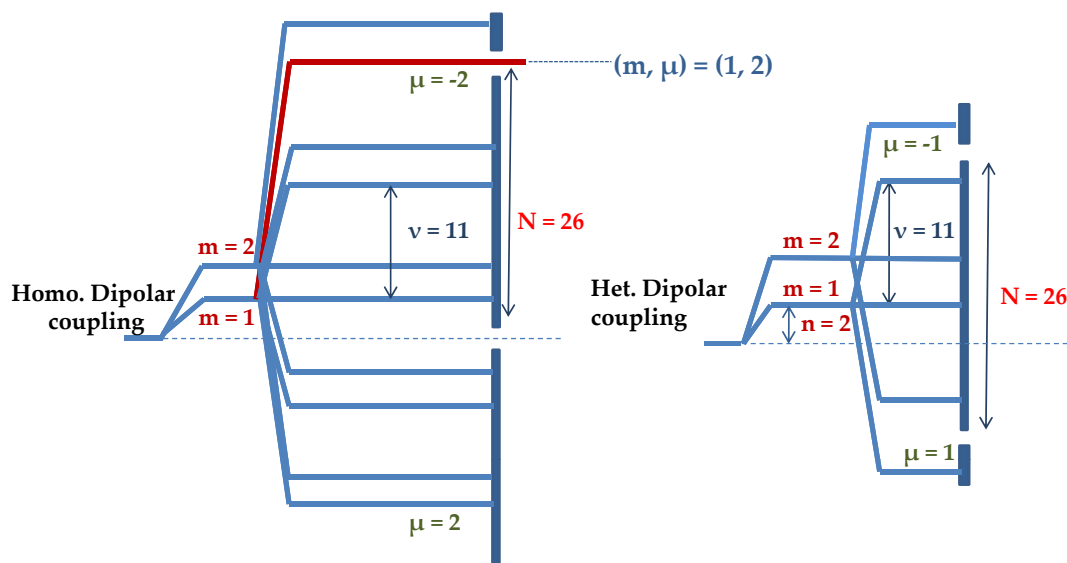
Figure 5.3: Space spin selection diagram for R26$_4^{11}$ homonuclear recoupling sequence.

quence can effectively suppress the signals from isolated ^{13}C spins while selectively detecting the NMR signals from natural pairs of ^{13}C atoms. The pulse sequence can schematically described as,

This is the basic 2D INADEQUATE pulse sequence. The initial $\frac{\pi}{2}$ pulse is used to bring the equilibrium z- magnetization to xy plane. After this a spin echo is inserted to reduce the effect of CSA while the second $\frac{\pi}{2}$ pulse excites the double quantum coherence. The final $\frac{\pi}{2}$ pulse converts the double quantum coherence to observable single quantum coherence. By proper phase cycling one can selectively filter out the signals coming from the double quantum coherence thereby ensuring that NMR signals from only the paired ^{13}C spins are detected. This is a powerful technique in a sense that this scheme can be used to trace out the whole skeleton of the molecule.
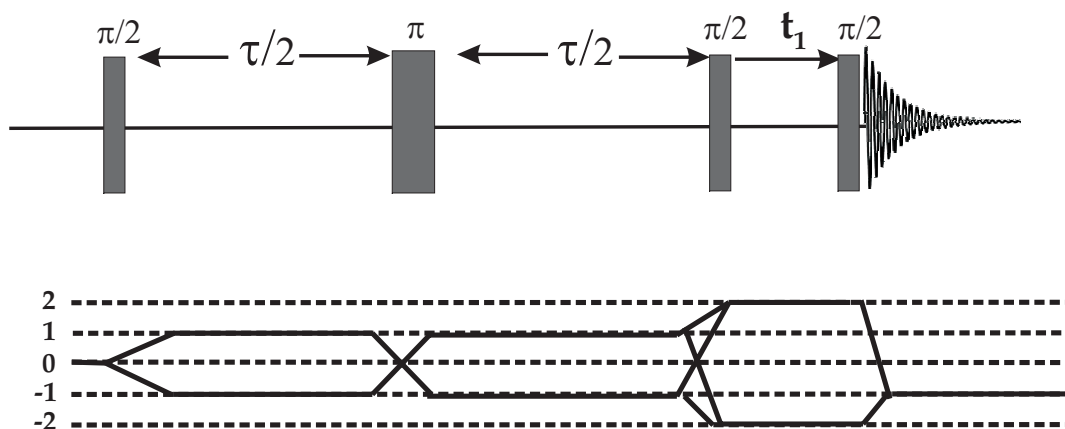
Figure 5.4: Pulse sequence diagram for 2D INADEQUATE experiment.

5.3   Experimental

^{29}Si MAS experiments were performed on Bruker Avance 500 NMR spectrometer equipped with standard Bruker triple-tuned MAS probes with 4 mm zirconia rotors. Ramped-^{1}H - ^{29}Si cross-polarisation (CP) [155] was employed with 15 ms of contact time. The ^{29}Si RF field strength during CP was kept at 33 kHz and that for ^{1}H was 38 kHz. The RF amplitude on the ^{1}H channel was smoothly varied from 30 kHz to 38 kHz during ramped-CP. For the INADEQUATE experiment the initial $\pi/2$ pulse was replaced by the CP and through out the experiment the ^{29}Si RF field strength was kept at 33 kHz while the spinning speed was maitained at 5 kHz. The 2Q excitation and conversion block for POST-C7 was 6.7 ms and for the supercycled R26$_4^{11}$ it was 21 ms. The spinning speed was 4720 and 5083 Hz and the ^{29}Si RF field strength during the dipolar recoupling sequence was 33 kHz for both POST-C7 and SR26$_4^{11}$, respectively. The spinning-speed stability was maintained within $\pm$ 1 Hz using a pneumatic MAS controller. CPMG implementation during acquisition is shown in the pulse sequence diagram, Fig. 5.4. ^{1}H decoupling

was not applied during the dipolar recoupling sequence or during the acquisition period. The π pulses in the CPMG were of duration 15 μs. All the relevant pulse and acquisition parameters are given in figure captions. Pure-absorption-mode spectra were obtained using TPPI [156] method by incrementing the phase of all the pulses prior to t_1 by 45^0. The ^{29}Si chemical shifts were referenced with respect to TMS. ZSM-5 (CN form) sample was synthesised by hydrothermal method using tetrapropyl ammonium as the pore-directing template.

5.4 Results and Discussion

Fig 5.4 shows the pulse sequence diagram for 2D single quantum-double quantum correlation experiment using POST-C7 for double quantum excitation and reconversion while CPMG is used for signal enhancement.

A ^{29}Si cross-polarisation magic-angle-spinning (CPMAS) spectrum of ZSM-5 is shown in Fig. 5.5a. The material disorder leads to a broadening of the various signals in the spectrum, however, most of the 12 expected crystallographic non-equivalent tetrahedral Si sites in the asymmetric unit of this orthorhombic ZSM-5 are resolved in the spectrum. The gain in signal-to-noise ratio achieved by CPMG acquisition is illustrated in Fig. 5.5c, which represents a reconstituted spectrum obtained by a co-addition of all of the 14 acquired echoes in a CPMAS experiment extended with CPMG sampling followed by Fourier transformation. Figure 5.5b shows the spikelet spectrum obtained by directly Fourier transforming the echo trains. An enhancement of 3.7 times in the signal intensity is observed which is well in accordance with the theoretical prediction that the S/N is proportional to the square root of the number of echoes. Although further sensitivity enhancement can be accomplished by employing ^{1}H decoupling to lengthen the echo train decay, limitations of our probe head hardware precluded acquisition with ^{1}H decoupling over the long acquisition period of 470 ms that we have used.

Dipolar recoupling in systems characterised by small dipole-dipole couplings may
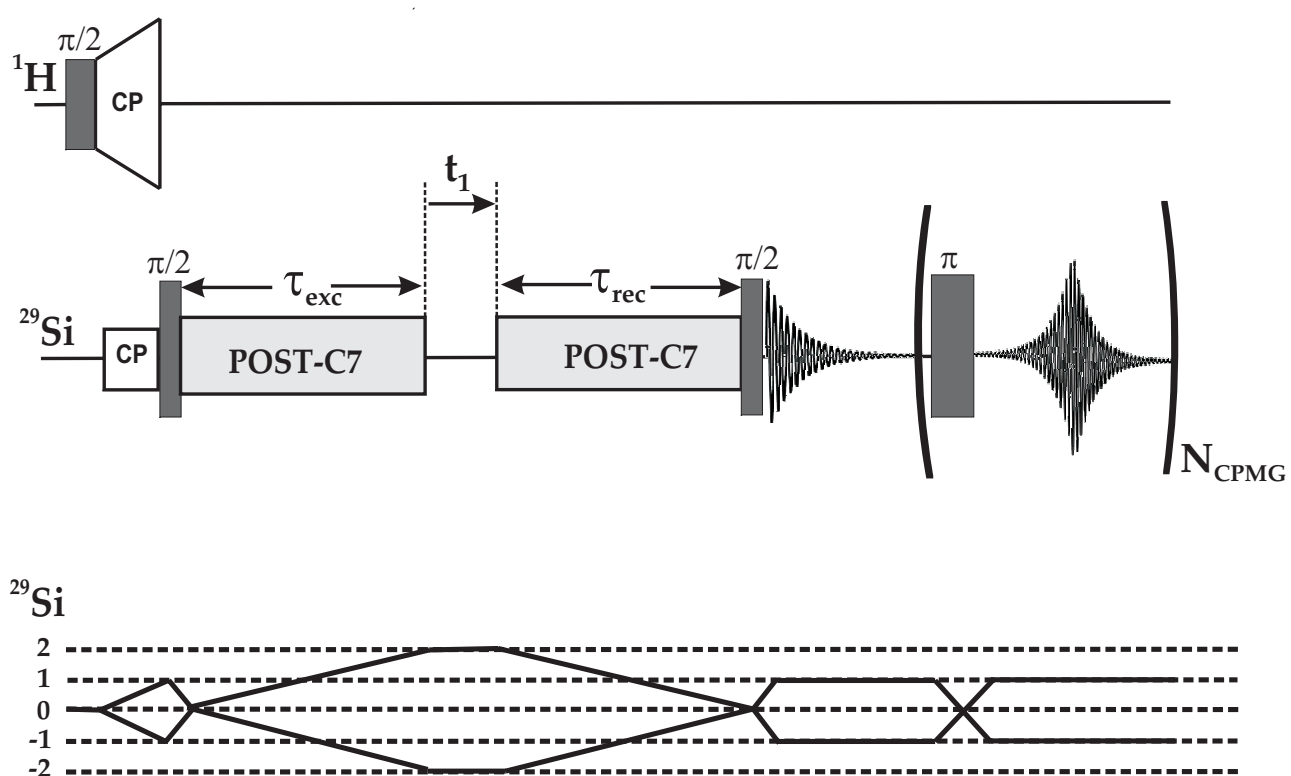
Figure 5.5: Pulse sequence diagram for 2D ^{29}Si 1Q-2Q correlation spectroscopy using POST-C7 dipolar recoupling sequence with CPMG spin echo refocusing during sampling.
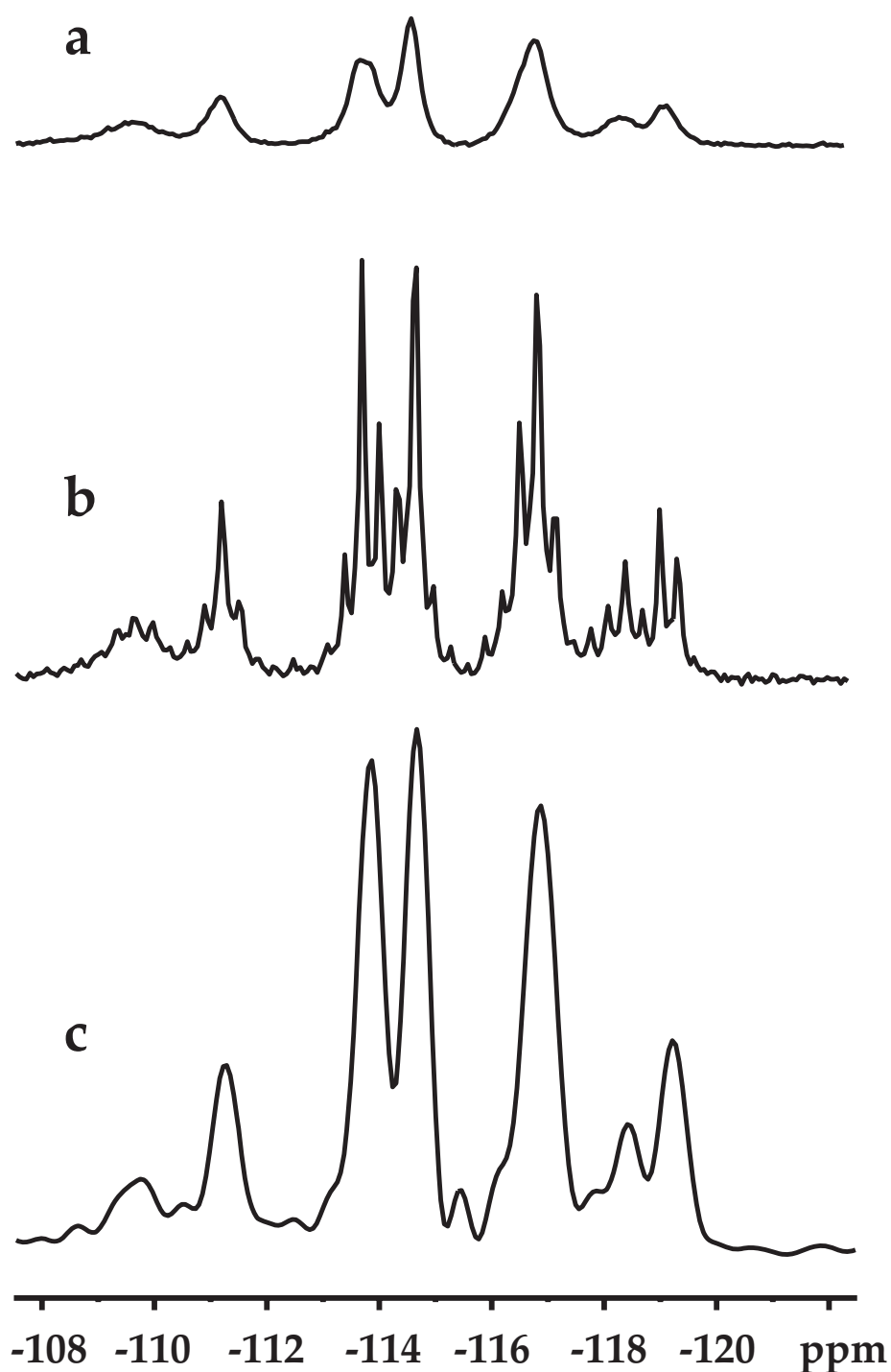
Figure 5.6: ^{29}Si CPMAS spectra of ZSM-5 (CN form). (a) Normal CPMAS spectrum. (b) Spikelet spectrum obtained by directly Fourier transforming the echo trains (total number of echoes, $N_{CPMG}= 14$) generated by CPMG π pulses with the corresponding delay between CPMG π pulses, $\tau_{CPMG}= 16$ ms. (c) Spectrum obtained by co-addition of spin echoes generated by a CPMG π pulse train ($\tau_{CPMG}= 16$ ms, $N_{CPMG}= 14$) followed by Fourier transform.

be challenging. It is well-known that in recoupling experiments such as POST-C7, the efficiency of excitation of 2Q coherence may degrade in systems with large chemical shift anisotropy (CSA) [157]. However, it has been shown by Levitt *et al.* that by applying supercycled $R26_4^{11}$ one can get rid of the destructive effect of large CSA [150]. It has also been shown by Brinkmann *et al.* that by applying a super cycle of the form $[R26_4^{11}R26_4^{-11}]$, the influence of the higher-order terms generated by large CSA can be removed from both first- and second-order average Hamiltonians [158]. In addition to this, $SR26_4^{11}$ can effectively decouple weak heteronuclear dipolar couplings [151]. As a result $SR26_4^{11}$ appears to be an obvious choice for 2Q experiments in systems with weak homonuclear dipolar couplings. However, in our case we are dealing with a system with very low CSA, as a result the damaging effect of CSA will be negligible. More over, in the present system the ^{1}H - ^{29}Si heteronuclear dipolar coupling is very weak, making it an ideal system to use POST-C7 homonuclear dipolar recoupling pulse sequence to excite 2Q coherences. The build up of the 2Q-filtered signal was monitored with both POST-C7 and $SR26_4^{11}$ in order to choose an optimum value for τ_{exc} and τ_{rec} [Fig. 5.4] that can be used for the 2D experiment. The results are shown in Fig. 5.6a for the ^{29}Si resonance at 114.6 ppm which represents a single site Si12 which is tetrahedrally connected to Si8, Si12, Si11, and Si3. The experimental data show that for ^{29}Si-^{29}Si dipolar interaction the 2Q build-up is substantially faster for POST-C7 as compared to $SR26_4^{11}$. The reason for the faster build up of the 2Q-filtered signal in case of POST-C7 is attributed to a higher dipolar scaling factor and the fact that POST-C7 is a γ-encoded sequence [159] whilst the γ-encoding is lost in $SR26_4^{11}$.

The sensitivity gain as a function of the number of echoes acquired when CPMG was implemented within POST-C7 pulse sequence (Fig. 5.4) is shown in Fig. 5.6b for one of the silicon sites. The S/N steadily builds up as the number of acquired echoes is increased and reaches a limiting value of 3.5 for the enhancement. A near 3.5 fold sensitivity gain can be achieved by choosing the number of echoes to be 12 in our experiments.
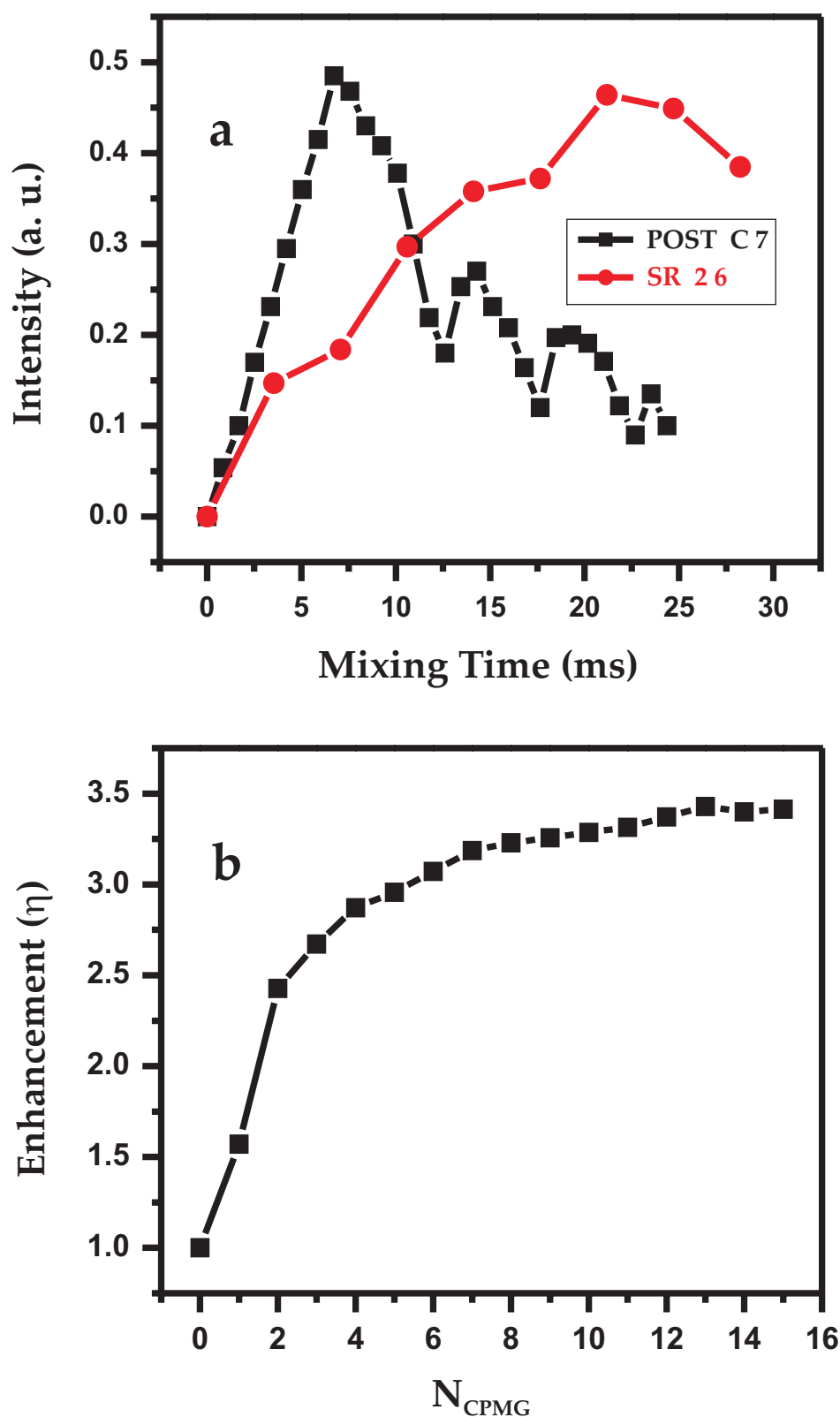
Figure 5.7: (a) 2Q-filtered signal build-up curves obtained with POST-C7 and SR26$_4^{11}$ dipolar recoupling sequences. (b) Plot of the sensitivity gain achieved as a function of the number of echoes acquired using CPMG refocusing within the acquisition period of POST-C7 with $\tau_{CPMG} = 16$ ms. The number of transients acquired was 384. The data is shown for the signal at 114.6 ppm corresponding to the T_{12} site.

The 2Q-filtered 1D POST-C7 spectra obtained without and with CPMG implementation are shown in Figs. 5.7a and 5.7b, whilst that for SR26$_4^{11}$ are shown in Figs. 5.7c and 5.7d. A maximum enhancement by a factor of 3.40 was obtained when successive thirteen CPMG π pulses were applied with SR26$_4^{11}$ used for dipolar recoupling. Interestingly, all the silicon signals noticed in the CPMAS spectrum appear in the 2Q-filtered 1D spectra of both sequences with comparable intensity. Since each of the 12 Si sites are connected to 4 next neighbour Si sites through Si-O-Si linkages in the ZSM-5 structure, all the Si sites pass through the 2Q filter due to ^{29}Si-^{29}Si dipolar coupling. Further, it may be noticed from the spectra that for the Si sites there are no differential signal enhancement from the CPMG acquisition since τ_{CPMG}, the time interval between π pulses, is sufficiently long (16 ms) to allow all signals to dephase between the pulses. The signal intensity of all the Si sites can therefore be uniformly increased in the 2D experiment by the spin-echo acquisition. The so-called "spikelet" spectrum obtained by direct Fourier transformation of the echo trains of a 2Q-filtered signal appear as singlets with linewidth of $\sim$ 3 Hz (not shown). The splitting due to $^2J_{Si-Si}$ coupling ($\sim$ 10 Hz) between two ^{29}Si sites is not observed in the spikelet spectrum presumably due to the decoupling of the J coupling by a combination of pulse imperfections and chemical-shift evolution between the pulses in a similar fashion as previously described for ^{15}N-^{15}N systems [160].

The sensitivity enhancement in the ^{29}Si 1Q-2Q correlation spectrum obtained by applying a CPMG train of π pulses during the t$_2$ acquisition period of POST-C7 sequence is illustrated in Fig. 5.8b. This is to be compared with the corresponding 2D 1Q-2Q correlation spectrum obtained without the CPMG spin-echo acquisition (Fig. 5.8a). These spectra were obtained using the optimum value for the recoupling time. The slight distortion noticed in the contour line shapes of the spin echo acquired data is probably due to the lack of proper phase cycling of the CPMG π pulses. Presence of one extra peak in the 2D plot can also be due to the same reason. We believe by applying cogwheel phase cycling [161] on the CPMG π pulses these may be reduced. Such minor line
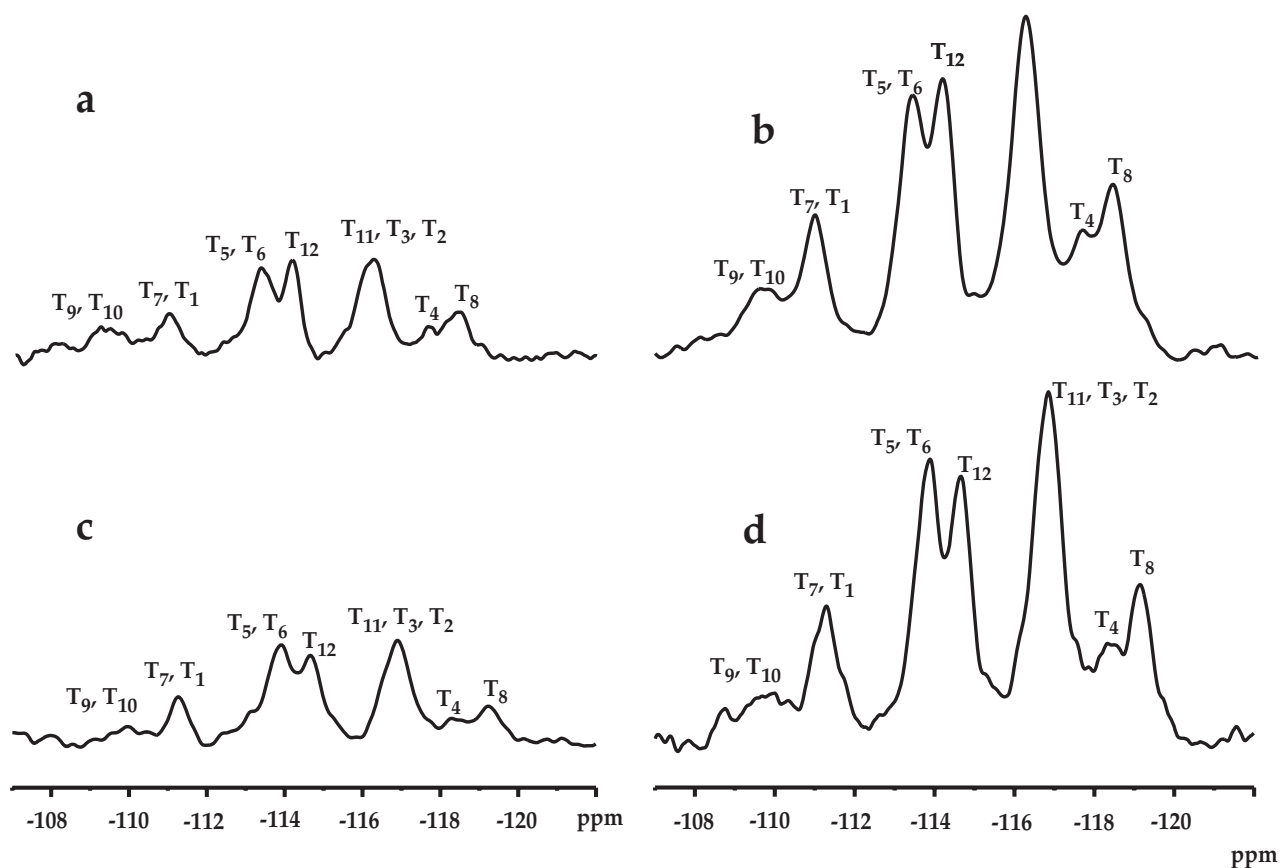
Figure 5.8: (a) 2Q-filtered ^{29}Si CPMAS spectrum obtained with POST-C7 ($\tau_{exc}= \tau_{rec}=$ 6.7 ms, NS = 384). (b) POST-C7-CPMG ($\tau_{exc}= \tau_{rec}=$ 6.7 ms, $\tau_{CPMG}=$ 16 ms, N$_{CPMG}=$ 12). (c) 2Q-filtered ^{29}Si CPMAS spectrum obtained with SR26$_4^{11}$ sequence ($\tau_{exc}= \tau_{rec}=$ 21 ms). (d) SR26$_4^{11}$-CPMG ($\tau_{exc}= \tau_{rec}=$ 21 ms, N$_{CPMG}=$ 13). The number of transients acquired was 384 for all the experiments.

distortions in the reconstructed spectra have been reported previously when CPMG π pulses were applied during acquisition period [58]. Nevertheless, the spectrum in Fig. 5.8b depicts all the expected Si-Si correlations, which occur at the sum of the isotropic chemical shifts along the indirect dimension. Due to the enhanced signal intensities, the spectrum in Fig. 5.8b at once enables us to identify the various Si-Si connectivities. Due to the degeneracy of the chemical shifts for some silicon sites, isolated Si-Si correlations can not be observed for some Si sites. However, the sensitivity enhanced 1Q-2Q correlation spectrum enables us to provide the correct assignments of the various signals to the crystallographic non-equivalent sites determined in the X-ray structure. The assignment of the signals was guided by the fact the X-ray structure of as-synthesised ZSM-5 and that of calcined ZSM-5 above 340 K are both orthorhombic having the same unit cell parameters and the same T-site connectivities [162]. The slight alterations in the T-site geometry of the as-synthesized form from that of calcined ZSM-5 gives rise to slight variations in the observed ^{29}Si chemical shifts from the previously reported values [140]. With this knowledge, the Si resonances in the spectrum could be correctly assigned as shown.

The ^{29}Si dipolar recoupling experiments such as POST-C7 and SR26$_4^{11}$ have a number of important advantages over the J-coupling-based INADEQUATE experiment which has been used previously to investigate the bonding networks of zeolites. A comparison of the correlation spectra obtained with the POST-C7 sequence (Figure 5.9b) and those obtained with the INADEQUATE sequence (Figure 5.9a) reveals that the former contains all of the Si-O-Si connectivity information, whereas the latter is missing the correlations between symmetry-related Si sites that should appear along the DQ diagonal. These "auto-correlations" provide important information about the structure of the zeolite framework; thus, it is advantageous to observe them directly. Another important feature of the dipolar recoupling sequence is that the DQ coherences build up much faster than in the INADEQUATE experiment. This is because the dipolar coupling con-
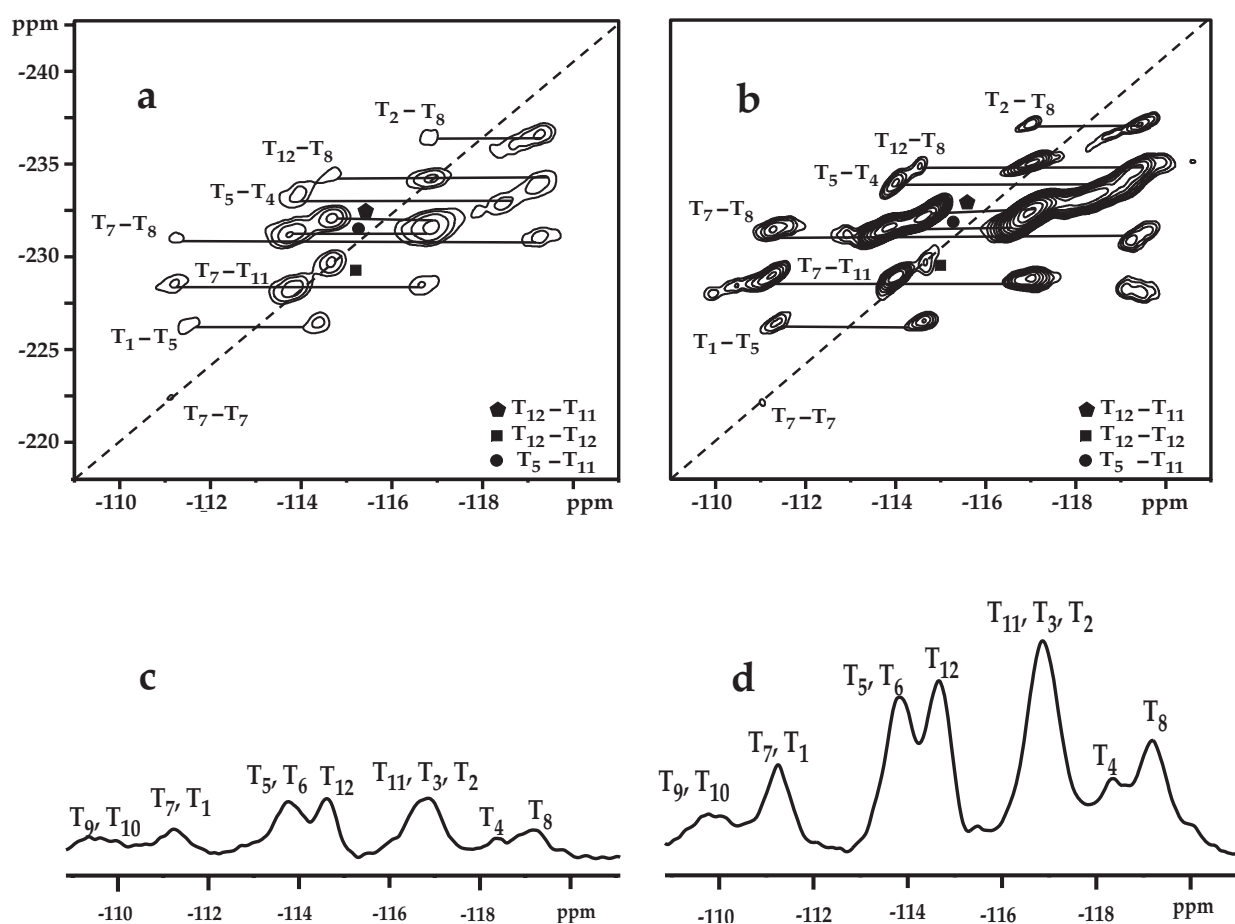
Figure 5.9: ^{29}Si 1Q-2Q correlation spectra of ZSM-5 (CN form) obtained with (a) POST-C7 and (b) POST-C7-CPMG with $\tau_{exc} = \tau_{rec} = 6.7$ ms, $\tau_{CPMG} = 16$ ms, and $N_{CPMG} = 12$. A total of 130 t_1 increments was taken with 125 μs of dwell time. 384 number of transients was taken for each t_1 increment with 1 s relaxation delay. (c) 1Q-dimension (F_2) projection from the 2D 1Q-2Q correlation spectrum obtained with POST-C7 and (d) with POST-C7-CPMG.

stants for ^{29}Si-O-^{29}Si spin pairs are about -160 Hz, an order of magnitude larger than the ^{29}Si-O-^{29}Si J-couplings (approximately 10-15 Hz). Consequently, the excitation and reconversion of the DQ coherences require less time, meaning that the POST-C7 experiment is affected less by relaxation.
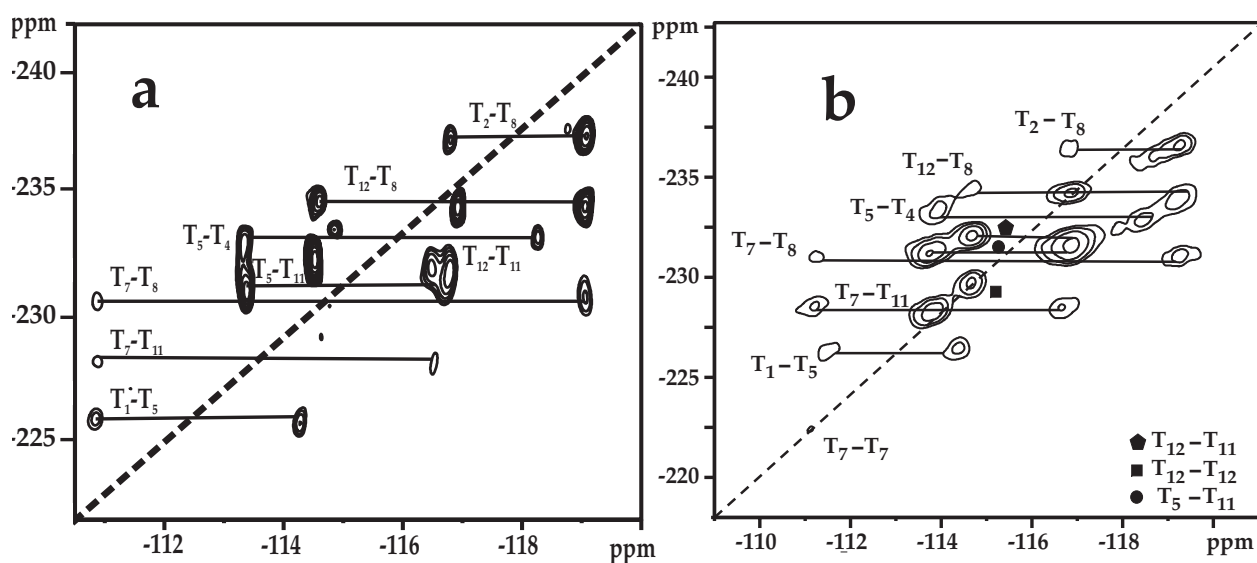
Figure 5.10: ^{29}Si 1Q-2Q correlation spectra of ZSM-5 (CN form) obtained with (a) IN-ADEQUATE and (b) POST-C7 .

5.5   Programs

In this section the pulse program which was used in Bruker Avance I to combine the POST-C7 and CPMG series of π pulses with in the acquisition window and the Bruker AU program to add the successive CPMG echoes are given.

5.5.1   Bruker Pulse Program (POST-C7 + CPMG)

include <Avancesolids.incl>

define delay rde1

define delay rde2

define delay rderx

define delay rdeadc

define delay rdepa

"rde1=de-de1"

"rde2=de-de2"

"rderx=de-derx"

"rdeadc=de-deadc"

"rdepa=de-depa"

define delay del6

"del6=d6/2"

;mc2 : STATES-TPPI

define pulse tau4

"tau4=((1s/cnst31)/7)"

define pulse tau1

"tau1=((0.25s/cnst31)/7)"

define pulse tau3

"tau3=((0.75s/cnst31)/7)"

"d31=1s/cnst31"

ze

1 d31

2 d1 do:f3

10u reset:f1 reset:f2 reset:f3

1m rpp11

1m rpp12

1m rpp13

1m rpp14

10u pl1:f2 pl2:f3 ;preselect pl2 drive power for F3

DE1 DE2 DERX DEADC DEPA DE3

0.3u

p3:f3 ph1 ;proton 90 pulse

(p15 ph2):f2 (p15:spf0 pl15 ph10):f3 ; Cross Polarization

; 1u pl12:f3

; 1u cpd2:f3

p1:f2 ph4

3 tau1:f2 ph11 ipp13 ipp14 ;c7 excitation

tau4:f2 ph12 ipp12

tau3:f2 ph11 ipp11

lo to 3 times l0

d0

4 tau1:f2 ph13 ;c7 reconversion

tau4:f2 ph14 ipp14

tau3:f2 ph13 ipp13

lo to 4 times l0

1u

1u DWELL_GEN

(p1 ph5):f2

d6

(p4 ph28):f2

d6

5 d6

(p4 ph28):f2

d6

lo to 5 times l22

aq

1m ip13*16384

1m ip14*16384

rcyc=2

30m do:f3 mc 0 to 2 F1PH(ip11*8192 ip12*8192, id0)

HaltAcqu, 1m ;for 1D

exit ;for 1D

ph0= 0

ph1= 0 0 0 0 2 2 2 2

ph2= 0 0 0 0 0 0 0 0 ;0*8 1*8 2*8 3*8

1 1 1 1 1 1 1 1

2 2 2 2 2 2 2 2

3 3 3 3 3 3 3 3

ph4= 1 1 1 1 1 1 1 1

2 2 2 2 2 2 2 2

3 3 3 3 3 3 3 3

0 0 0 0 0 0 0 0

ph5= 1 2 3 0 1 2 3 0

2 3 0 1 2 3 0 1

3 0 1 2 3 0 1 2

0 1 2 3 0 1 2 3

ph28= 1 1 1 1 2 2 2 2

2 2 2 2 3 3 3 3

3 3 3 3 0 0 0 0

0 0 0 0 1 1 1 1

ph10=1

ph11=(65536) 0 9362 18725 28087 37449 46811 56174

ph12=(65536) 32768 42130 51493 60855 4681 14043 23406

ph13=(65536) 0 9362 18725 28087 37449 46811 56174

ph14=(65536) 32768 42130 51493 60855 4681 14043 23406

ph30= 0

; ph31=0 1 2 3 2 3 0 1 ;SQ phase cycling

; 1 2 3 0 3 0 1 2

; 2 3 0 1 0 1 2 3

; 3 0 1 2 1 2 3 0

ph31= 1 0 3 2 3 2 1 0 ;DQ phase cycle with cpmg pulses

2 1 0 3 0 3 2 1

3 2 1 0 1 0 3 2

0 3 2 1 2 1 0 3

5.5.2   AU Program to Add The Echoes

```
/****************************************************************/
    /* au_cpmgadd 01.02.2003 */ /****************************************************
    /* Short Description : */
    /* Program to store echos from cpmgall.av experiment */
    /* by adding them up */
    /****************************************************************/
    /* Keywords : */
    /* echo, CPMG */
    /****************************************************************/
    /* Description/Usage: */
    /* After data acquisition using cpmgall.av */
    /* check first data point where sampled intensity grows */
    /* out of noise. Everything else is calculated from */
```

```
/* this pivot point. */

/* Program takes data points with echo information */

/* and stores as result summation of all echos. */

/* After first execution of the program the value of the */

/* pivot point is stored and suggested on subsequent */

/* executions so that the question for the pivot point */

/* can be answered with a simple 'return'. */

/* Program stores result as time domain data into 1r */

/* and 1i files for further processing, */

/* raw data are kept! */

/**************************************************************/

/* Author(s) : */

/* Name : Stefan Steuernagel */

/* Organisation : Bruker Analytik */

/* Email : stefan.steuernagel@bruker.de */

/**************************************************************/

/* Name Date Modification: */

/* ste 030201 created */

/**************************************************************/

int size, sizeout, si2, tdout, tdout2, td2, ireal, sizeofint, parmod, zero=0, td1;

char binfile[255], pulprog[255];

int wdw2,pk2,bc2,ft2,mem2,corrpoints,j1,igegen;

int *in1, *in2;

int order_{aB}IT, first, echopoints, echos, l22, dead, pivot, zeroth;

float del3, del6, pul3, pul4, dwell, aa;

double swh;

char s1[255];
```

```
/* STOPMSG("illegal input"); */
GETCURDATA;
/* reihen rausschreiben*/
WRA(10000);
REXPNO(10000);
SETCURDATA;
FETCHPAR1S("TD",td1);
j1=1;
/* (void)printf("\ n\ %d, %d ",j1,td1); */
TIMES(td1);
RSER(j1,10000+j1,1);
j1++;
END;
FETCHPARS("FL1",pivot);
FETCHPARS("L 22", echos)
/* —————————————————————*/
/* get relevant acquisition parameters */
FETCHPARS("TD",td2);
FETCHPARS("SI",si2);
FETCHPARS("SW_h",swh);
FETCHPARS("D 6",del6);
FETCHPARS("D 3",del3);
FETCHPARS("P 3",pul3);
FETCHPARS("P 4",pul4);
FETCHPARS("L 22",l22);
FETCHPARS("DW",dwell);
FETCHPARS("BYTORDA",order_a_BIT);
```

```
/* ————————————————————*/
/* check for starting point */
/* if (pivot>80) pivot=(int)((10/dwell)); */
if (strlen(cmd) == 0)
GETINT("Enter pivot point : ",pivot);
else
if (1 != sscanf(cmd, "%", pivot))
STOPMSG("illegal input");
if (strlen(cmd) == 0)
GETINT("Enter number of echos to be added up : ",echos);
else
if (1 != sscanf(cmd, "%d", echos))
STOPMSG("illegal input");
if (strlen(cmd) == 0)
GETINT("Enter number of correction points for the echo length : ",corrpoints);
else
if (1 != sscanf(cmd, "%d", corrpoints))
STOPMSG("illegal input");
/* ————————————————————*/
/* calculate required loop parameters */
/* zeroth=(int)((pul3+del3*2000000.0+pul4)/dwell+0.5)+pivot; */
/* zeroth=(zeroth/2)*2; */
/* first=(int)((del6*1000000.0+del3*2000000.0+pul4)/dwell+0.5)+zeroth; */
/* first=(first/2)*2; */
zeroth=pivot;
zeroth=(zeroth/2)*2;
echopoints=(int)(del6*2000000.0/dwell+0.5);
```

```
echopoints=(echopoints/2)*2+corrpoints;

dead=(int)((del3*2000000.0+pul4)/dwell+0.5)+2;

dead=(dead/2)*2;

/* echos=l22; */

/*tdout=echopoints;*/

tdout=td2;

tdout2=td2;

/* tdout2=2^(log(tdout)/log(2)+1);*/

/* tdout2=pow_next(tdout);*/

/* STOREPAR("TD",tdout2*2);*/

/* STOREPARS("TD",tdout2*2);*/

sizeout=tdout2*sizeof(int);

/* (in 10000, for write-out later) */

/*—————————————————————-*/

/* loop over rows, 10001 etc */

j1=1;

TIMES(td1);

REXPNO(10000+j1);

SETCURDATA;

GETCURDATA;

/* ———————————————————*/

/* open file and allocate array */

(void)sprintf(binfile,"%s/data/%s/nmr/%s/%d/fid",disk,user,name,expno);

sizeofint=sizeof(int);

size=td2*sizeofint;

in1=calloc(td2,sizeof(int));

in2=calloc(td2,sizeof(int));
```

```
if ( (ireal=open(binfile, O_RDWR)) == -1)

Perror(DEF_ERR_OPT,binfile);

ABORT;

if ( read(ireal,in1,size) == -1 )

Perror(DEF_ERR_OPT,binfile);

ABORT;

/* ————————————————————*/

/* correct for byteorder */

/* local_swap4(in1,size,order_a_BIT); */

/* ————————————————————*/

/* create final output array */

i1=zeroth;

i2=0;

TIMES2(echopoints);

in2[i2]=0;

i2++;

END;

/* add up */ i2=0;

TIMES2(echopoints);

TIMES3(echos);

in2[i2]+=in1[i1];

i1+=echopoints;

END;

i2++;

i1=zeroth+i2;

END;

/* fold */
```

```
/* i2=1; */
/* TIMES2(echopoints/4); */
/* igegen=echopoints-i2; */
/* in2[i2]+=in2[igegen]; */
/* i2++; */
/* igegen=echopoints+2-i2; */
/* in2[i2]+=in2[igegen]; */
/* i2++; */
/* END; */
/* rest = 0 */
/* i2=echopoints/2+1; */
/* TIMES2(echopoints/2); */
/* in2[i2]=0; */
/* i2++; */
/* END; */
if ( lseek(ireal, 0, SEEK_SET) == -1 )
Perror(DEF_ERR_OPT,binfile);
ABORT;
/* ————————————————————————*/
/* correct for byteorder */
/* local_swap4(in2,sizeout,order_a_BIT); */
if ( write(ireal,in2,sizeout) == -1 )
Perror(DEF_ERR_OPT,binfile);
ABORT;
/* ————————————————————————*/
/* correct relevant acquisition parameters */
/* STOREPAR("TD",td2); */
```

```
/* STOREPARS("TD",td2); */

/* STOREPAR("TDeff",tdout); */

/* STOREPARS("TDeff",tdout); */

STOREPAR("SI",tdout2*2);

STOREPARS("SI",tdout2*2);

/* ————————————————————*/

/* prepare for processing */

FETCHPAR("WDW",wdw2)

FETCHPAR("PH_mod",pk2)

FETCHPAR("BC_mod",bc2)

FETCHPAR("FT_mod",ft2)

FETCHPAR("ME_mod",mem2)

/* ————————————————————*/

/* set required parameters to NO */

STOREPAR("WDW",0)

STOREPAR("PH_mod",0)

STOREPAR("BC_mod",0)

STOREPAR("FT_mod",0)

STOREPAR("ME_mod",0)

/* ————————————————————*/

/* store new FID into 1r and 1i */

TRF;

/* ————————————————————*/

/* restore original FID */

/* if ( lseek(ireal, 0, SEEK_SET) == -1 )  */

/* Perror(DEF_ERR_OPT,binfile); */

/* ABORT; */
```

```
/*  */
/* —————————————————————*/
/* correct for byteorder */
/* local_swap4(in1,size,order_a_BIT); */
/* if ( write(ireal,in1,size) == -1 )  */
/* Perror(DEF_ERR_OPT,binfile); */
/* ABORT; */
/*  */
/* —————————————————————*/
/* restore original parameters */
STOREPAR("WDW",wdw2)
STOREPAR("PH_mod",pk2)
STOREPAR("BC_mod",bc2)
STOREPAR("FT_mod",ft2)
STOREPAR("ME_mod",mem2)
/* STOREPARS("TD",td2); */
/* STOREPAR("TD",td2); */
/* STOREPAR("TDeff",td2); */
/* STOREPARS("FL1",pivot);*/
free(in1);
free(in2);
(void)close(ireal);
(void)sprintf(text,"CPMG echo summation done");
Show_status(text);
/* —————————————————————*/
/* write row into 10000 */
WSERP(j1, name, 10000, 1, disk, user)
```

```
j1++;

END;

/* end loop over rows */

/*————————————————-*/

/* (void)printf("\ n\ %d, %d ",tdout2,echopoints); */

QUIT

include <inc/sysutil>
```

5.6 Conclusions

We have shown that POST-C7 dipolar recoupling sequence can be effectively used for 2Q excitation to study the ^{29}Si-^{29}Si connectivity in the zeolites because of low CSA associated with ^{29}Si in the present system. The fact that the ^{29}Si-^{1}H heteronuclear dipolar coupling is small also has contributed to the success of the POST-C7 method. We have further shown that ^{29}Si dipolar recoupled 1Q-2Q correlation spectra can be obtained under magic-angle spinning with a 3.5 fold sensitivity enhancement achieved by the acquisition of spin echoes generated by a CPMG pulse train. The sensitivity enhancement provided in the as-synthesized ZSM-5 high silica zeolite has enabled the identification of the dipolar correlations at each resolved silicon sites and has led to the resonance assignments in the MAS spectra. It was also shown that POST-C7 is much superior technique than INADEQUATE for structural characterization since it is less affected by relaxation as the double quantum build up is much faster in the former.

Bibliography

[1] E. M. Purcell, H. C. Torrey, and R. V. Pound,Phys. Rev. **69** (1946) 37.

[2] F. Bloch, W. W. Hansen, and M. Packard,Phys. Rev. **69** (1946) 127.

[3] I.I. Rabi, J.R. Zacharias, S. Millman, P. Kusch, Phys. Rev. **53** (1938) 318.

[4] M. R. Hansen, L. Mueller, A. Pardi, Nat. Struct. Biol. **5** (1998) 1065.

[5] M. Mehring, *High Resolution NMR Spectroscopy in Solids* (Springer-Verlag, Germany, 1976).

[6] S. R. Hartman and E. L. Hahn, Phys. Rev. **128** (1962) 2042.

[7] A. Pines, M. G. Gibby, J. Schaefer, and J. S. Waugh, J. Chem. Phys. **59** (1973) 569.

[8] B. C. Garstein, C. R. Debowski, *Transient Techniques in NMR of Solids* (Academic Press, New York, 1985).

[9] A. Abragam, *The Principles of Nuclear Magnetism* (Oxford Press, Oxford, 1961).

[10] M. H. Levitt, *Spin dynamics: Basics of Nuclear Magnetic Resonance,* (Wiley, 2001).

[11] M. H. Cohen, F. Reif, *Solid State Phys 5* (Academic Press, New York, 1957).

[12] A. J. Vega, *Encyclopedia of Nuclear Magnetic Resonance* (Wiley, 1996).

[13] M. E. Rose, *Elementary Theory of Angular Momentum* (Wiley, New York, 1957).

[14] A. Medek, J. S. Harwood, L. Frydman, J. Am. Chem. Soc. **117** (1995) 12779.

[15] A. Samoson, E. Lippmaa, A. Pines, Mol Phys **65** (1988) 1013.

[16] A. Llor, J. Virlet, Chem Phys Lett **152** (1988) 248.

[17] B. F. Chmelka, K. T. MǍuller, A. Pines, J. Stebbins, Y. Wu, J. W. Zwanziger, Nature **339** (1989) 42.

[18] D. D. Laws, H. L. Bitter, A. Jerschow, Angew. Chem. Int. Ed. **41** (2002) 3096.

[19] Z.H. Gan, J. Am. Chem. Soc. 122 (2000) 3242.

[20] A. Samoson, B. Q. Sun, A. Pines, *Pulsed Magnetic Resonance: NMR, ESR, and Optics* (Ed.: D. M. S. Bagguley, Clarendon, Oxford, 1992).

[21] S. P. Brown, S. Wimperis, J. Magn. Reson. **124** (1997) 279.

[22] M. J. Duer, *Solid-state NMR spectroscopy: Principles and application* (Oxford: Blackwell Science, 2002)

[23] K. J. D. MacKenzie, M. E. Smith, *Multinuclear solid state NMR of inorganic materials* (Pergamon Press, Oxford, 2002).

[24] G. A. Morris, R. Freeman, J. Am. Chem. Soc. **101** (1979) 760.

[25] K. G. R. Pachler , P. L. Wessels, J Magn Reson **12** (1973) 337.

[26] C. A. Fyfe, K. C. Wongmoon, Y. Huang, H. Grondey, J. Am. Chem. Soc. **117** (1995) 10397.

[27] R. V. Pound, Phys. Rev. **79** (1950) 685.

[28] S. Vega, Y. Naor, J. Chem. Phys. **75** (1981) 7586.

[29] P. K. Madhu, A. Goldbourt, L. Frydman, S. Vega, Chem. Phys. Lett. **307** (1999) 41.

[30] Z. Yao, H. T. Kwak, D. Sakellariou, L. Emsley, P. J. Grandinetti, Chem. Phys. Lett **327** (2000) 85.

[31] P. K. Madhu, K. J. Pike, R. Dupree, M. H. Levitt, M. E. Smith, Chem. Phys. Lett. **367** (2003) 150.

[32] P. K. Madhu, O. G. Johannessen, K. J. Pike, R. Dupree, M. E. Smith, M. H. Levitt, J. Magn. Reson. **163** (2003) 310.

[33] A. P. M. Kentgens, R. Verhagen, Chem. Phys. Lett. **300** (1999) 435.

[34] D. Iuga, H. Schäfer, R. Verhagen, A. P. M. Kentgens, J. Magn. Reson. **147** (2000) 192.

[35] H. Schäfer, D. Iuga, R. Verhagen, A. P. M. Kentgens, J. Chem. Phys. **114** (2001) 3073.

[36] D. Iuga, A. P. M. Kentgens, J. Magn. Reson. **158** (2002) 65.

[37] S. Prasad, H. -T. Kwak, T. Clark, P. J. Grandinetti, J. Am. Chem. Soc. **124** (2002) 4964.

[38] R. Siegel, T. T. Nakashima, R. E. Wasylishen, Chem. Phys. Lett. **388** (2004) 441.

[39] R. Siegel, T. T. Nakashima, R. E. Wasylishen, Conc. Magn. Reson. **26A** (2005) 47.

[40] R. Siegel, T. T. Nakashima, R. E. Wasylishen, Chem. Phys. Lett. **421** (2006) 529.

[41] R. Siegel, T. T. Nakashima, R. E. Wasylishen, J. Magn. Reson. **184** (2007) 85.

[42] A. P. M. Kentgens, J Magn Reson. **95** (1991) 619.

[43] J. Haase, M. S. Conradi, Chem. Phys. Lett. **209** (1993) 287.

[44] J. Haase, M. S. Conradi, C. P. Grey, A. J. Vega, J. Magn. Reson. **A109** (1994) 90.

[45] J. Haase, M. S. Conradi, E. Oldfield, J. Magn. Reson. **A109** (1994) 210.

[46] S.L. McCall, E.L. Hahn, Phys. Rev. **183** (1969) 457.

[47] M.S. Silver, R.I. Joseph, D.I. Hoult, J. Magn. Reson. **59** (1984) 347.

[48] R. Siegel, T. T. Nakashima, R. E. Wasylishen, Concepts Magn Reson Part A **26A** (2005) 47Ű61.

[49] I. Solomon, Phys. Rev. **110** (1958) 61.

[50] I. D. Weisman, L. H. Bennett, Phys. Rev. **181** (1969) 1341.

[51] H. Y. Carr, E. M. Purcell, Phys. Rev. **94** (1954) 630.

[52] S. Meiboom, D. Gill, Rev. Sci. Instrm. **29** (1958) 688.

[53] F. H. Larsen, H. J. Jakobsen, P. D. Ellis, N. C. Nielsen, Chem. Phys. Lett. **292** (1998) 467.

[54] F. H. Larsen, H. J. Jakobsen, P. D. Ellis, N. C. Nielsen, J. Phys. Chem. A **101** (1997) 8597.

[55] F. H. Larsen, A. Lipton, H. J. Jakobsen, N. C. Nielsen, P. D. Ellis, J. Am. Chem. Soc. **121** (1999) 3783.

[56] F. H. Larsen, H. J. Jakobsen, P. D. Ellis, N. C. Nielsen, J. Magn. Reson. **131** (1998) 144.

[57] F. H. Larsen, H. J. Jakobsen, P. D. Ellis, and N. C. Nielsen, Mol. Phys. **95** (1998) 1185.

[58] R. Siegel, T. T. Nakashima, R. E. Wasylishen, Concepts in Magnetic Resonance Part A. **26** (2005) 62.

[59] T. Vosegaard, F. H. Larsen, H. J. Jakobsen, P. D. Ellis, N. C. Nielsen, J. Am. Chem. Soc. **119** (1997) 9055.

[60] F. H. Larsen, N. C. Nielsen, J. Phys. Chem. A **103** (1999) 10825.

[61] R. Lefort, J. W. Wiench, M. Pruski, J.-P. Amoureux, J. Chem. Phys. **116** (2002) 2493.

[62] Y. Yarim-Agaev, P. N. Tutunjian, and J. S. Waugh, J. Magn. Reson. **47** (1982) 51.

[63] T. G. Oas, R. G. Griffin, M. H. Levitt, J. Chem. Phys.**89** (1988) 692.

[64] T. Gullion, J. Schaefer, J. Magn. Reson. **81** (1989) 196.

[65] T. Gullion, J. Schaefer, Adv. Magn. Reson. **13** (1989) 57.

[66] R. Tycko, G. Dabbagh, Chem. Phys. Lett. **173** (1990) 461.

[67] A. E. Bennett, J. H. Ok, R. G. Griffin, S. Vega, J. Chem. Phys. **96** (1992) 8624.

[68] N. C. Nielsen, H. Bilds$\oslash e, H.J.Jakobsen, M.H.Levitt, J.Chem.Phys.$**101**$(1994)1805.$

[69] Y. K. Lee, N. D. Kurur, M. Helmle, O. Johannessen, N. C. Nielsen, M. H. Levitt, Chem. Phys. Lett. **242** (1995) 304.

[70] M. H. Levitt, *Encyc. of NMR* (D.M. Grant, R.K. Harris, Eds., John Wiley & Sons, Chichester, 2002).

[71] A. Brinkmann, M. H. Levitt, J. Chem. Phys. **115** (2001) 357.

[72] G. Wu, Solid-state ^{17}O NMR Prog. Nucl. Magn. Reson. Spectrosc. 52 (2008) 118.

[73] A. Goldbourt, P. K. Madhu, Monatsh. Chem. **133** (2002) 1497.

[74] A. Goldbourt, P. K. Madhu, Annu. Rep. in NMR Specy. **54** (2005) 81.

[75] T. Bräuniger, K. Ramaswamy, P. K. Madhu, Chem. Phys. Lett. **383** (2004) 403.

[76] T. Bräuniger, P. K. Madhu, A. Pampel, D. Reichert, Solid State Nucl. Magn. Reson. **26** (2004) 114.

[77] T. Bräuniger, G. Hempel, P. K. Madhu, J. Magn. Reson. **181** (2006) 68.

[78] H. -T. Kwak, S. Prasad, T. Clark, P. J. Grandinetti, Solid State Nucl. Magn. Reson. **24** (2003) 71.

[79] A. P. M. Kentgens, E. R. H. van Eck, T. G. Ajithkumar, T. Anüpold, J. Past, A. Reinhold, A. Samoson, J. Magn. Reson. **178** (2006) 212.

[80] A. Goldbourt, P. K. Madhu, S. Kababya, S. Vega, Solid State Nucl. Magn. Reson. **18** (2000) 1.

[81] D. E. Woessner, American Mineralogist. **74** (1989) 203.

[82] T. Bräuniger, K. J. Pike, R. K. Harris, P. K. Madhu, J. Magn. Reson. **163** (2003) 64.

[83] C. Adachi, T. Tsutsui *Organic Light Emitting Devices*, (Ed.: J.Shinar), Springer-Verlag, NewYork, 2004.

[84] C. W. Tang, S. A. Van Slyke, Appl. Phys. Lett. **51** (1987) 913.

[85] M. Brinkmann, G. Gadret, M. Muccini, C. Taliani, N. Masciocchi, A. Sironi, J. Am. Chem. Soc. **122** (2000) 5147.

[86] M. Braun, J. Gmeiner, M. Tzolov, M. Coelle, F. D. Meyer, W. Milius, H. Hillebrecht, O. Wendland, J. U. V. Schutz, W. Brutting, J. Chem. Phys. **114** (2001) 9625.

[87] M. Cölle, R.E. Dinnebier, W. Brütting, Chem. Commun. **23** (2002) 2908.

[88] M. Cölle, J. Gmeiner, W. Milius, H. Hillebrecht, W. Brütting, Adv. Funct. Mater. **13** (2003) 108.

[89] B. C. Lin, C. P. Cheng, Z. Q. You, C. P. Hsu, J. Am. Chem. Soc. **127** (2005) 66.

[90] A. Lesage, M. Bardet, L. Emsley, J. Am. Chem. Soc. **121** (1999) 10987.

[91] H. Kaji, K. Schmidt-Rohr, Macromolecules, 33 (2000) 5169.

[92] M. Utz, M. Nandagopal, M. Mathai, F. Papadimitrakopoulos, Appl. Phys. Lett. **83** (2003) 4023.

[93] M. Utz, M. Nandagopal, M. Mathai, F. Papadimitrakopoulos, J. Chem. Phys. **124** (2006) 0347051.

[94] T. Bräuniger, R. Poupko, Z. Luz, P. Gutsche, C. Meinel, H. Zimmermann, U. Haeberlen, J. Chem. Phys. **112** (2000) 10858.

[95] T. Bräuniger, R. Poupko, Z. Luz , H. Zimmermann , U. Haeberlen, J. Chem. Phys. **115** (2001) 8049.

[96] A. Jerschow, Prog. Nucl. Magn. Reson. Spectrosc. **46** (2005) 63.

[97] A. Goldbourt, P. K. Madhu, Monatshefte für Chemie, **133** (2002) 1497.

[98] R. S. Thakur, N. D. Kurur, P. K. Madhu, Chem. Phys. Lett. 426 (2006) 459.

[99] S. Ganapathy, L. Delevoye, J. -P. Amoureux, P. K. Madhu, Magn. Reson. Chem. **46** (2008) 948.

[100] A. Goldbourt, P. K. Madhu, Annu. Rep. NMR Spectrosc. **54** (2004) 81.

[101] D. D. Laws, Hans-Marcus L. Bitter, A. Jerschow, Angew. Chem. Int. Ed. **41** (2002) 3096.

[102] R. W. Schurko, R. E. Wasylishen, H. Foerster, J. Phys. Chem. A **102** (1998) 9750.

[103] H. Kaji, Y. Kusaka, G. Onoyama, F. Horii, Jpn. J. Appl. Phys. **44** (2005) 3706.

[104] C. J. Cramer, *Essentials of Computational Chemistry-Theories and Models*, (John Wiley and Sons, Chichester, 2003).

[105] D. Massiot, F. Fayon, M. Capron, I. King, S. L. Calve, B. Alonso, Jean-Olivier Durand, B. Bujoli, Z. Gan, G. Hoatson, Magn. Reson. Chem. **40** (2002) 70.

[106] V. V. N. Ravi Kishore, Ph.D. Thesis, Tata Institute of Fundamental Research, Mumbai, 2004.

[107] A. I. Vogel, *A Text Book of Quantitative Inorganic Analysis Including Elementary Instrumental Analysis*, (3^{rd}Ed., ELBS New Delhi, 1970).

[108] M. Mucccini, M. A. Loi, K. Kenevey, R. Zamboni, N. Masciocchi, A. Sironi, Adv. Mater. **16** (2004) 861.

[109] M. J. Frisch, G. W. Trucks, H. B. Schlegel, G. E. Scuseria, M. A. Robb, J. R. Cheeseman, V. G. Zakrzewski, J. A. Montgomery Jr., T. Vreven, K. N. Kudin, J. C. Burant, J. M. Millam,

S. S. Iyengar, J. Tomasi , V. Barone, B. Mennucci, M. Cossi, G. Scalmani, N. Rega, G. A. Petersson, H. Nakatsuji, M. Hada, M. Ehara, K. Toyota, R. Fukuda, J. Hasegawa, M. Ishida, T. Nakajima, Y. Honda, O. Kitao, H. Nakai, M. Klene, X. Li, J. E. Knox, H. P. Hratchian, J. B. Cross, V. Bakken, C. Adamo, J. Jaramillo, R. Gomperts, R. E. Stratmann, O. Yazyev, J. A. Austin, R. Cammi, C. Pomelli, J. W. Ochterski, P. Y. Ayala, K. Morokuma, G. A. Voth, P. Salvador, J. J. Dannenberg, V. G. Zakrzewski, S. Dapprich, A. D. Daniels, M. C. Strain, O. Farkas, D. K. Malick, A. D. Rabuck, K. Raghavachari, J. B. Foresman, J. V. Ortiz, Q. Cui, A. G. Baboul, S. Clifford, J. Cioslowski, B. B. Stefanov, G. Liu, A. Liashenko, P. Piskorz, I. Komaromi, R. L. Martin, D. J. Fox, T. Keith, M. A. Al-Laham, C. Y. Peng, A. Nanayakkara, M. Challacombe, P. M. W. Gill, B. Johnson, W. Chen, M. W. Wong, C. Gonzalez, J. A. Pople Gaussian Inc., Wallingford CT, 2004.

[110] J. B. Foresman, T. A. Keith, K.B. Wiberg, J. Snooria, M. J. Frisch, J. Phys. Chem. **100** (1996) 16098.

[111] L. Onsager, J. Am. Chem. Soc. **58** (1936) 1486.

[112] S.Miertus, E.Scrocco, Tomasi, J. Chem. Phys. **55** (1981) 117.

[113] T. Takahagi, A. Saiki, H. Sakaue, S. Shingubara, Jpn. J. Appl. Phys. **42** (2003) 157.

[114] R. L. Martin, J. D. Kress, I. H. Campbell, D. L. Smith, Phys. Rev. B **61** (2002) 15804.

[115] R. W. Schurko, S. Wi, L. Frydman, J. Phys. Chem. A **106** (2002) 512.

[116] D. Das, L. J. Barbour, J. Am. Chem. Soc. **130** (2008) 14032.

[117] V. Kello, A. J. Sadlej, P. Pyykko, D. Sundholm, M. Tokman, Chem. Phys. Lett. **304** (1999) 414.

[118] Y. Nishiyama, T. Fukushima, K. Takami, Y. Kusaka, T. Yamazaki, H. Kaji, Chem. Phys. Lett. **471** (2009) 80.

[119] T. J. Bastow, M. E. Smith, H. J. Whitfield, J. Mater. Chem. **6** (1996) 1951.

[120] S. Kuroki, A. Takahashi, I. Ando, A. Shoji, T. Ozaki, J. Mol. Struct. **323** (1994) 197 .

[121] L.M. Bull, A.K. Cheetham, A. Samoson, T. Anupõld, A. Reinhold, J. Sauer, B. Bussemer, V. Moravetski, Y. Lee, S. Gann, J. Shore, A. Pines, R. Dupree, J. Am. Chem. Soc. **120** (1998) 3510.

[122] I. Farnan, P.J. Grandinetti, J.H. Baltisberger, J.F. Stebbins, U. Werner, M.A. Eastman, A. Pines, Nature **358** (1992) 31.

[123] V. Lemaitre, R.R. Planque, A.P. Howes, M.E. Smith, R. Dupree, A. Watts, J. Am. Chem. Soc. **126** (2004) 15320.

[124] D. Freude, J. Haase, NMR, *Basic Principles and Progress*, (vol. 29, Springer Verlag, Berlin, 1993).

[125] M. Linder, A. Höhener, R. R. Ernst, J. Chem. Phys. **73** (1980) 4959.

[126] E.R.H. van Eck, M.E. Smith, J. Chem. Phys. **108** (1998) 5904.

[127] Jacco D. van Beek , Ray Dupree , Malcolm H. Levitt, J. Magn. Reson. **179** (2006) 38.

[128] S. R. Hartmann, E. L. Hahn, Phys. Rev. **128** (1962) 1042.

[129] M. Lee, W. I. Goldberg, Phys. Rev. A **140** (1965) 1261.

[130] L. Frydman, J.S. Harwood, J. Am. Chem. Soc. **117** (1995) 5367.

[131] R. S. Thakur, N. D. Kurur, P. K. Madhu, Chem. Phys. Lett. **426** (2006) 459.

[132] Hyung-Tae Kwak, Zhehong Gan, J. Magn. Reson. **164** (2003) 369.

[133] M. Bak, J. T. Rasmussen, N. C. Nielsen, J Magn Reson **147** (2000) 296.

[134] M. Bak, N. C. Nielsen, J Magn Reson **125** (1997) 132.

[135] D. Massiot, F. Fayon, M. Capron, I. King, S. L. Calve, B. Alonso, Jean-Olivier Durand, B. Bujoli, Z. Gan, G. Hoatson, Magn. Reson. Chem. **40** (2002) 70.

[136] F. Fayon, D. Massiot, M. H. Levitt, J. J. Titman, D. H. Gregory, L. Emsley, S. P. Brown, J. Chem. Phys. **122** (2005) 194313.

[137] F. Zigan, R. Rothbauer, Neues Jb. Miner. Mh. (1967) 137.

[138] D. D. Elleman, D. Williams, J. Chem. Phys. **25** (1956) 742.

[139] C. A. Fyfe, H. Gies, Y. Feng, G. T. Kokotailo, Nature **341** (1989) 223.

[140] C. A. Fyfe, H. Grodney, Y. Feng, G. T. Kokotailo, J. Am. Chem. Soc. **112** (1990) 8812.

[141] N. Maity, S. Basu, M. Mapa, P. R. Rajamohanan, S. Ganapathy, C. S. Gopinath, S. Bhaduri, G. K. Lahiri, J. Catal. **242** (2006) 332.

[142] J. W. Wiench, Y. S. Avadhut, N. Maity, S. Bhaduri, G. K. Lahiri, M. Pruski, S. Ganapathy, J. Phys. Chem. B **111** (2007) 3877.

[143] D. W. Breck, *Zeolite Molecular Sieves*, (Wiley, New York, 1974).

[144] J. Datka, S. Marschmeyer, T. Neubauer, J. Meusinger, H. Papp, F.-W. Schütze, I. Szpyt, J. Phys. Chem. **100** (1996) 14451.

[145] M. E. Davis, Nature, **417** (2002) 813.

[146] J. Trebosc, J. W. Wiench, S. Huh, V. S.-Y. Lin, M. Pruski, J. Am. Chem. Soc. **127** (2005) 7587.

[147] G. J. Kennedy, J. W. Wiench, M. Pruski, Solid State Nucl. Magn. Reson. **33** (2008) 76.

[148] J. W. Wiench, V. S.-Y. Lin b, M. Pruski, J. Magn. Reson. **193** (2008) 233.

[149] A. Bax, R. Freeman, S.P. Kempsell, J. Am. Chem. Soc. **102** (1980) 4849-51.

[150] P. E. Kristiansen, M. Carravetta, W. C. Lai, M. H. Levitt, Chem. Phys. Lett. **390** (2004) 1.

[151] D. H. Brouwer, P. E. Kristiansen, C. A. Fyfe, M. H. Levitt, J. Am. Chem. Soc. **127** (2005) 542.

[152] M. Hohwy, H. J. Jakobsen, M. Edén, M. H. Levitt, N. C. Nielsen, J. Chem. Phys. **108** (1998) 2686.

[153] M. Carravetta, M. Edén, O.G. Johannessen, H. Luthman, P.J.E. Verdegem, J. Lugtenburg, A. Sebald, M.H. Levitt, J. Am. Chem. Soc. **123** (2001) 10628.

[154] N.C. Nielsen, H. Bildsøe, H.J. Jakobsen, M.H. Levitt, J. Chem. Phys. **101** (1994) 1805.

[155] G. Metz, X. Wu, S. O. Smith, J. Magn. Reson. A **110** (1994) 219.

[156] D. Marion, K. Wüthrich, Biochem. Biophys. Res. Commun. **113** (1983) 967.

[157] T. Karlsson, J. M. Popham, J. R. Long, N. Oyler, G. P. Drobny, J. Am. Chem. Soc. **125** (2003) 7394.

[158] A. Brinkmann, J. Schmedt auf der Günne, M. H. Levitt, J. Magn. Reson. **156** (2002) 79.

[159] N. C. Nielsen, H. Bildsøe, H. J. Jakobsen, M. H. Levitt, J. Chem. Phys. **101** (1994) 1805.

[160] J. Dittmer, G. Bodenhausen, Chem.Phys.Chem. **7** (2006) 831.

[161] M. H. Levitt, P. K. Madhu, C. E. Hughes, J. Magn. Reson. **155** (2002) 300.

[162] H. V. Koningsveld, J. C. Jansen, H. V. Bekkum, Zeolites. **390** (1990) 235.